WIDE-BANDGAP III-NITRIDE TUNNEL JUNCTIONS AND NOVEL APPROACHES TOWARDS IMPROVING OPTOELECTRONIC DEVICES

A Dissertation
Presented to
The Academic Faculty

by

Evan A. Clinton

In Partial Fulfillment
Of the Requirements for the Degree
Doctor of Philosophy in Electrical and Computer Engineering

Georgia Institute of Technology
May 2020

WIDE-BANDGAP III-NITRIDE TUNNEL JUNCTIONS AND NOVEL APPROACHES TOWARDS IMPROVING OPTOELECTRONIC DEVICES

Approved by:

Dr. W. Alan Doolittle, Advisor
School of Electrical and Computer Engineering
Georgia Institute of Technology

Dr. Bruno Frazier
School of Electrical and Computer Engineering
Georgia Institute of Technology

Dr. P. Douglas Yoder
School of Electrical and Computer Engineering
Georgia Institute of Technology

Dr. Arijit Raychowdhury
School of Electrical and Computer Engineering
Georgia Institute of Technology

Dr. Samuel Graham
School of Mechanical Engineering
Georgia Institute of Technology

Date Approved: 3/17/2020

ACKNOWLEDGEMENTS

First, I want to thank my advisor, Professor W. Alan Doolittle, for his continual support and guidance throughout my research efforts. I am truly appreciative for all the time and energy he afforded me to help understand and solve the many challenges we faced.

I am tremendously grateful for the love and support my family has provided me throughout these years in graduate school. My sisters Lauren and Margo, and my parents Dorothy and Andrew Clinton have always had my back, relieved my anxieties, and provided timely advice.

I am also very fortunate to have worked with some outstanding colleagues in the Advanced Semiconductor Technology Facility. I want to thank Dr. Brendan Gunning and Dr. Chloé Fabien for training and mentoring me during my early time in the group. Additionally, I want to thank Dr. Brooks Tellekamp, Joe Merola, Dr. Joshua Shank, Zachary Engel, Alex Weidenbach, Jobi Zivasatienraj, Christopher Matthews, Habib Ahmad, Aheli Ghosh, Timothy McCrone, and Keisuke Motoki. Additionally, I am especially thankful and pleased for the opportunity to work alongside and become great friends with Dr. Ehsan Vadiee. We all combined to form a collaborative team, and I hope to get the chance to work with some members of the team again.

Much of my work would be impossible if it were not for the hard work and many resources provided by the staff in the Institute for Electronics and Nanotechnology, especially Walter Henderson, Scott Fowler, Eric Woods, Charlie Turgeon, Charlie Suh, Bob Rose, and Paul Turgeon. I appreciate their willingness to always provide their help.

Finally, I want to thank my thesis committee: Dr. Douglas Yoder, Dr. Bruno Frazier, Dr. Samuel Graham, and Dr. Arijit Raychowdhury for their consideration and direction throughout this process.

TABLE OF CONTENTS

LIST OF TABLES

LIST OF FIGURES

LIST OF NOMENCLATURE

Å	Angstrom (10^{-10} meter)
λ	wavelength
ρ	resistivity
σ	conductivity
Ω	Ohm
μ	carrier mobility
μm	micron (10^{-6} meter)
AFM	atomic-force microscopy
Al	aluminum
AlGaN	aluminum gallium nitride
AlN	aluminum nitride
DI	deionized
E_g	bandgap energy
eV	electron volt
FWHM	full width at half maximum
Ga	gallium
GaN	gallium nitride
Ge	germanium
H_2SO_4	sulfuric acid
H_2O_2	hydrogen peroxide
HEMT	high electron mobility transistor
HF	hydrofluoric acid
I-V	current-voltage
In	indium
InGaN	indium gallium nitride
InN	indium nitride
J_{SC}	short-circuit current density
K	Kelvin
LED	light-emitting diode
MBE	molecular-beam epitaxy
Mg	magnesium

MOCVD	metal-organic chemical vapor deposition
N_2	nitrogen
NH_3	ammonia
PL	photoluminescence
RC	rocking curve
RF	radio frequency
RGA	residual-gas analyzer
RHEED	reflection high-energy electron diffraction
RMS	root-mean-square
RSM	reciprocal space map
sccm	standard cubic centimeters per minute
SEM	scanning electron microscope
Si	silicon
SiC	silicon carbide
SIMS	secondary-ion mass spectrometry
TD	tunnel diode
TJ	tunnel junction
T_{sub}	substrate (growth) temperature
UHV	ultra-high vacuum
UV	ultraviolet
V_{OC}	open-circuit voltage
W	Watts
XRD	x-ray diffraction

SUMMARY

In order to supply the world with an ever-improving electronic experience in a manner that minimizes damage to the earth, we must constantly re-imagine and improve upon the overall performance and efficiencies of all electronic systems and their devices. Fortunately, the periodic table of elements can act as a sort of toolbox, where combinations of elements in various environments and configurations allow for a vast number of material systems to explore and engineer into practical solutions to modern problems. The III-nitride semiconductors are an especially promising material system to explore. There are many applications for the III-nitride material system, most notably in the form of commercial power electronics and optoelectronics, such as the white light emitting diode (LED). In this work, a combination of novel techniques, materials, and devices are explored to enhance III-nitride optoelectronics in a wide range of important wavelengths.

Group-III nitride devices have a substantial optoelectronic market primarily in solid state lighting (SSL) via white LEDs. Typically, the devices consist of a III-nitride blue LED with a phosphor coating that converts some blue light (450 nm) to a longer wavelength (*e.g.* yellow at 550 nm) so the combined emission appears as white light. The phosphor is required because outside the blue emission range, the III-nitrides are currently power inefficient. Pursuing longer wavelength III-nitrides is promising for solar cells and red or green LEDs, while the shorter wavelengths into the ultraviolet light are promising for water and air sterilization as an alternative to bulky UV lamps or chemical sterilization. The purpose of this research is to advance both the material and design of III-nitride devices to improve the efficiency and overall performance of next generation electronics and

optoelectronics.

Low bandgap III-nitride materials are investigated to improve longer wavelength optoelectronic devices. In order to synthesize low bandgap III-nitride material below the bandgap of GaN at 3.4 eV, indium must be incorporated into the crystal in the form of InN, InGaN, InAlN, or InGaAlN. High indium incorporation into the crystal is achieved via plasma-assisted molecular beam epitaxy (PAMBE) at low growth substrate temperatures < 400 °C. The low substrate temperatures allow for the InN compounds to form without thermally decomposing, which occurs at the higher temperatures more conventionally used for the synthesis of GaN and other wide-bandgap III-nitrides. Although the plasma-enhanced approach is compatible with the low-temperature incorporation of indium, the plasma is demonstrated to damage the crystal in the form of elevated unintentional background electron concentrations and a textured surface morphology. To further investigate the cause of the damage, the plasma is characterized with a Langmuir probe and via optical emission spectroscopy. InN films are grown as a sensitive thin film under various plasma conditions to characterize and observe the material outcomes. The optimal plasma condition is determined to be a high nitrogen flow and low plasma power. This condition minimizes the damage by reducing the background electron concentration by 74%, providing insight towards future high-indium content III-nitride devices.

GaN homojunction tunnel junctions are investigated to enhance both the commercial blue wavelength as well as shorter wavelength optoelectronics. Extreme n- and p-type doping is established which is essential to form tunnel junctions in such a wide bandgap material. State-of-the-art doping is achieved for both Si-doped n-type and Mg-doped p-type GaN with carrier concentration values of 3.1 and 1.5 x 10^{20} cm^{-3}, respectively.

The extreme doping is then applied to form GaN standalone tunnel diodes at various n- and p-type doping levels and even with delta doping. Negative differential resistance is measured at the lowest reported peak voltage of 1.3 V, and is measurable down to cryogenic temperatures as low as 77 K. Tunnel junctions are then demonstrated as tunnel contacts to p-i-n diodes exhibiting the lowest ever reported voltage penalty of ~0.1 V for homojunction GaN. Additionally, tunnel-contacted InGaN multi-quantum well (MQW) solar cells and LEDs are fabricated, which demonstrate these heavily doped tunnel junctions are compatible in both forward and reverse bias applications.

Finally, ultra-wide-bandgap AlGaN material is synthesized to enable ultraviolet optoelectronics. Techniques are established to limit phase separation in the ternary material, while still maintaining smooth crystal morphology, and allow for the extreme doping necessary for tunnel junctions. Standalone homojunction AlGaN tunnel diodes are formed and exhibit the first ever measured negative differential resistance in an AlGaN device for Al contents up to ~19%. Reverse-bias tunneling is observed up to 60% Al, promising for deep-UV optoelectronics.

CHAPTER 1: INTRODUCTION

The group III-nitrides have been thoroughly investigated due to many of their material properties such as their high breakdown fields, tunable bandgap (from 0.7 for InN to 6.1 eV for AlN), high drift velocity, high mobility, and large absorption coefficients [1]–[4]. These material properties are promising for electronic and optoelectronic devices such as microwave amplifiers, light emitting diodes (LEDs) and lasers, as well as high voltage power switches [1], [5], [6].

1.1 Structural Properties of the III-Nitrides

The III-nitrides consist of Al, Ga, and In metal atoms that form compounds with N. The III-nitride compounds are most thermodynamically stable in the form of a hexagonal wurtzite crystal structure, but can also be in the cubic zinc-blende form. The wurtzite crystal unit cell is displayed in Figure 1.1, where the *a*- and *c*-spacing are highlighted [7].

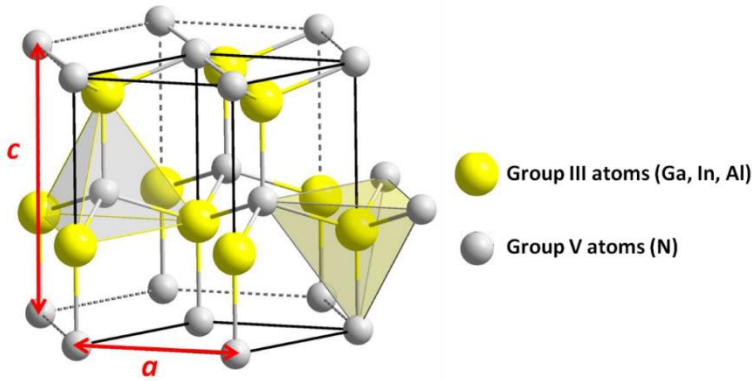

Figure 1.1. Wurtzite GaN unit cell with *a*- and *c*-lattice spacing highlighted [7].

The *a* and *c* lattice parameters of the III-nitrides are different for each of the three binaries of InN, GaN, and AlN. Both lattice parameters increase in length from AlN, to GaN, and to InN. The bandgap energy for the binaries corresponds inversely to the lattice spacing. The III-nitride binary bandgap energies are 6.2, 3.4, and 0.65 eV for AlN, GaN, and InN, respectively. The bandgap energy and wavelength vs the *a* lattice parameter are shown in Figure 1.2.

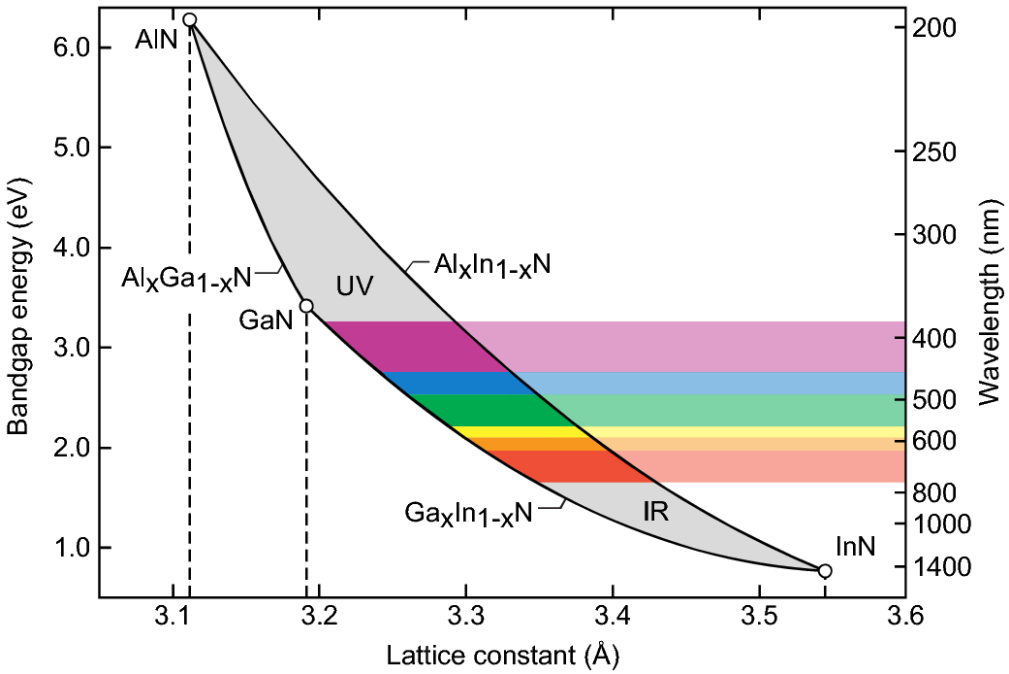

Figure 1.2. Bandgap energy and wavelength vs. *a* lattice constant for the III-nitride material system [8].

Remarkably, the III-nitrides have bandgap energies corresponding to wavelengths from the infrared, through the visible, to the ultraviolet range. The bandgap of the III-nitrides can be tuned to any energy between 0.65 and 6.2 eV by alloying the metals to form

binaries (AlN, GaN, and InN), ternaries (InGaN, AlGaN, and AlInN), and quaternaries (AlInGaN). Due to this wide range of tunable, direct bandgaps, the material system is well suited for optoelectronic applications such as solar cells, LEDs, and lasers.

1.2 Molecular Beam Epitaxy Growth of the III-Nitrides

The III-nitrides materials in this work are synthesized with the plasma-assisted molecular beam epitaxy (PAMBE) technique. MBE is a physical vapor deposition technique where source materials are thermally evaporated in the form of a molecular beam from the effusion cells onto the substrate in an ultra-high vacuum (UHV) environment. The UHV environment allows for a long mean free path for particles, which ensures a low probability that two particles collide on the way from the effusion cell to the substrate surface for growth. Particle collisions are avoided since collisions hinder smooth and high quality crystal growth during physical vapor deposition. MBE systems can reach vacuum levels down to the 5.0×10^{-11} Torr range when idling, corresponding to a mean free path of 1.5×10^{6} m for a nitrogen molecule. During growth, the chamber pressure is typically closer to the 1.0×10^{-5} Torr range, which corresponds to a mean free path of ~7.5 m, much greater than the distance between the effusion cell and substrate surface.

The plasma-assisted variant for the III-nitrides involves a radio frequency (RF) nitrogen plasma source to generate the nitrogen species for the crystal. A schematic diagram of a PAMBE system is shown in Figure 1.3. The nitrogen plasma and effusion cells are all aimed at the substrate holder. In this work, the effusion cells will contain the group-III sources of Al, Ga, and In, as well as the dopant sources of Si, Ge, and Mg. A cold liquid nitrogen (LN_2) cryopanel surrounds the hot substrate heater and effusion cells to

protect the structural integrity of the steel chamber as well as preventing thermal interference between hot components. A residual gas analyzer (RGA) is connected to the system to detect gaseous species in the chamber, including unwanted impurities and thus can help maintain the cleanliness of the system by identifying leaks.

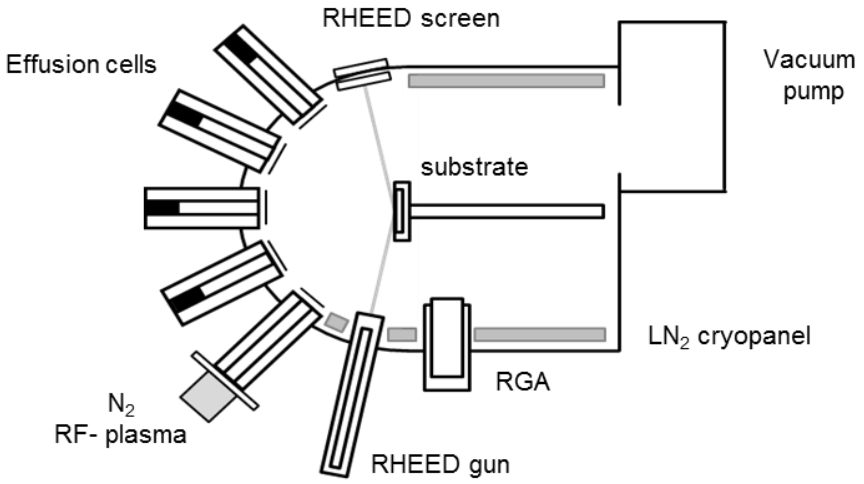

Figure 1.3. Schematic diagram of an MBE system [9].

A reflection high energy electron diffraction (RHEED) gun and phosphorous screen are also attached to the MBE tool. A RHEED gun provides a stream of electrons that diffract off the near-surface of the growing crystal on the substrate. The diffracted electron beam hits and illuminates a pattern on the phosphorous screen. The pattern can provide insights into the lattice spacing, strain, composition, polarity, and others. Additionally, the intensity transient of the RHEED pattern can offer real-time feedback on the layer-by-layer growth of the crystal.

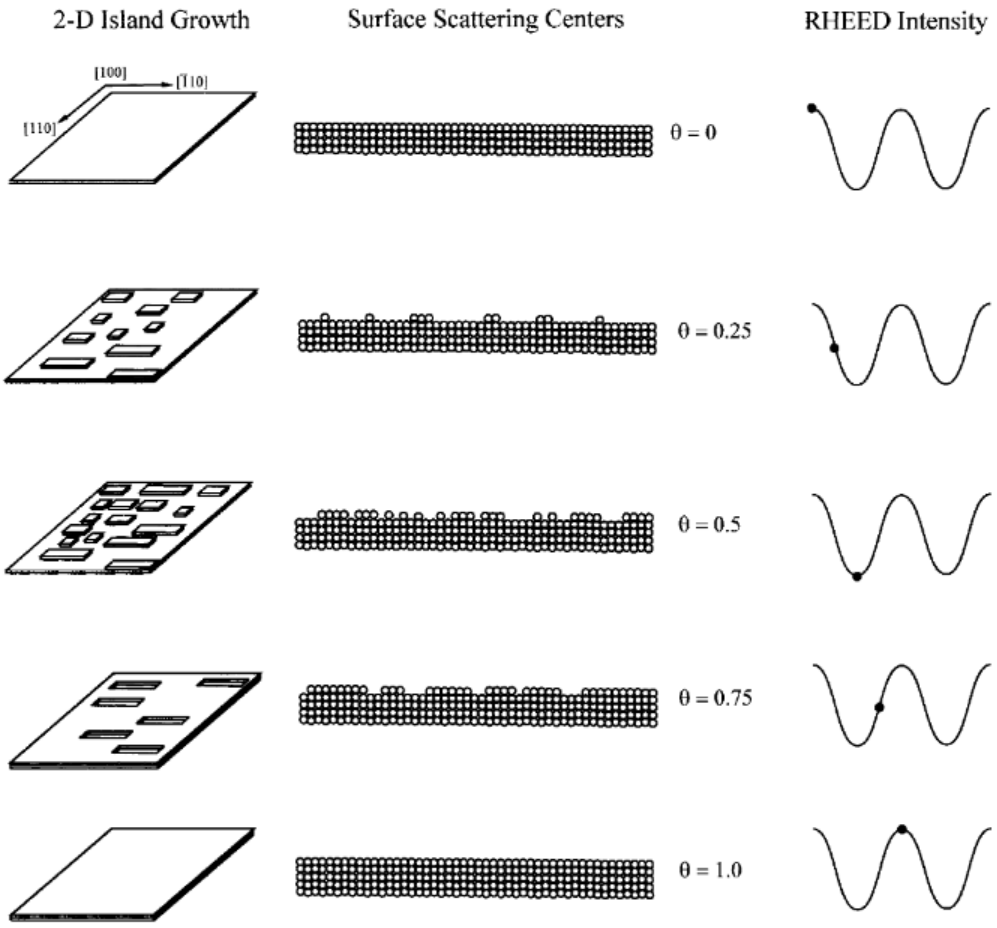

Figure 1.4. RHEED intensity scattering during layer-by-layer growth [10].

An example layer-by-layer growth process and a corresponding RHEED intensity transient is detailed in Figure 1.4. When the surface is pristine, all the diffracted electrons constructively interfere and hit the screen to result in a high intensity signal. When the next layer begins to form and is partially covering the surface, the electrons scatter and the signal intensity decreases, until the next layer is formed fully. Therefore, the RHEED intensity transient can allow for layer-by-layer growth monitoring *in-situ*.

1.3 Difficulties for the III-Nitrides

1.3.1 Heteroepitaxy of III-Nitrides on Non-Native Substrates

Although the group III-nitrides have a significant commercial presence in power electronics and optoelectronics such as the white light LED, they are still limited by many growth and fabrication related challenges [11], [12]. One of the main difficulties in the III-nitrides is that growths are most commonly initiated on non-native substrates [13]. Bulk GaN native substrates are becoming more available, but they are still in the development stage and are substantially more expensive than non-native ones [14]–[16]. The non-native substrates are typically sapphire (Al_2O_3), silicon carbide (SiC), or silicon (Si) wafers, with a lattice mismatch to GaN of 14, 3, and 17%, respectively [13]. The large lattice mismatch between the substrates and GaN results in dislocation generation once the GaN layer exceeds the short critical thickness for relaxation [17]. Figure 1.5 illustrates how the lattice mismatch for the heteroepitaxy of GaN on sapphire generates a large dislocation density typically around 10^9 - 10^{10} cm^{-2} at the heteroepitaxial interface [18]. Remarkably, with the proper cleaning procedures, virtually no threading dislocations are generated during the homoepitaxial growth of GaN on a bulk GaN substrate [19].

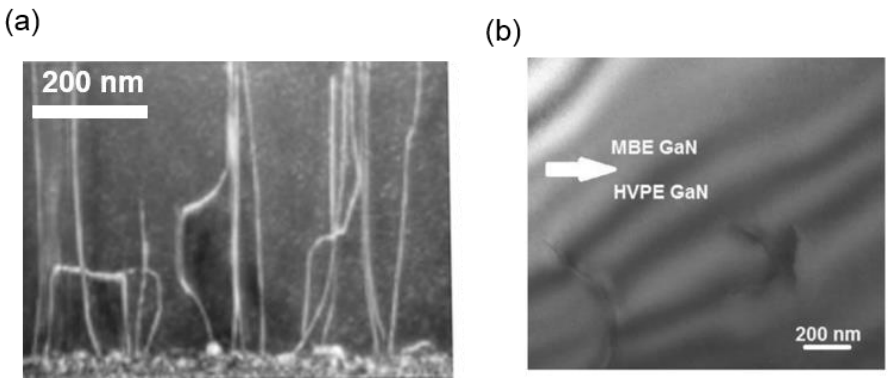

Figure 1.5. Cross-sectional TEM images for GaN grown on (a) sapphire and (b) bulk GaN [18], [19].

Threading dislocations can propagate into the active layers of a device and severely degrade their performance. Dislocations have been shown to deteriorate III-nitride device performance in the form of non-radiative recombination centers for LEDs and solar cells or in the form of providing pathways for leakage current and reducing the breakdown voltage of a p-n junction power device [20]–[23]. In addition to the a large lattice mismatch between non-native substrates that can cause dislocations, the coefficient of thermal expansion mismatch can cause cracking on cool-down, *e.g.* for thick GaN layers grown on Si, and these effects can even cause cracking in sapphire substrates [24], [25]. An example optical microscope image of a cracked GaN epilayer grown on Si (111) is shown in Figure 1.6 [26].

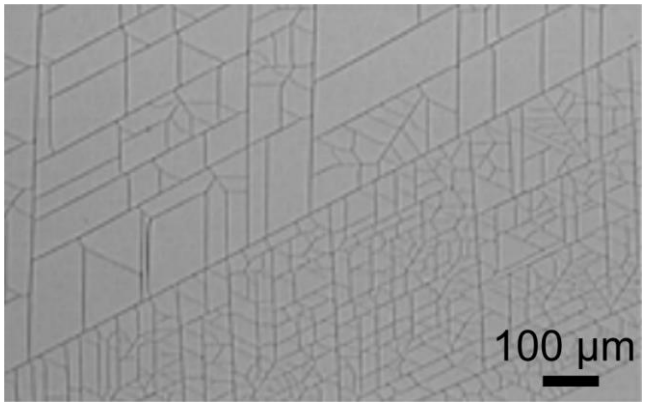

Figure 1.6. Optical microscope image of the crystallographic cracks on the surface of GaN grown on Si (111) [26].

1.3.2 Thick Buffer Layers Grown at High Growth Rates to Mitigate Substrate Effects

One promising avenue to minimize the effect of high dislocation densities in III-nitrides grown on non-native substrates is to grow buffer layers. Buffer layers are inserted between the substrates and the grown III-nitride layers in order to mitigate dislocation generation and propagation via strain engineering, as well as to prevent the Si-Ga eutectic formation when growing on Si substrates [27]. Buffer layers are of varying complexity from simple AlN layers to more complex, strain engineered AlN/GaN superlattices. Superlattice buffer layers have demonstrated the ability to prevent dislocation formation from strain engineering but also the ability to terminate dislocations [28], [29]. Threading dislocation termination is possible by turning or redirecting the dislocations until they annihilate by colliding with another dislocation. Threading dislocation densities can be further reduced by growing thick, many microns of film after the heteroepitaxial interface to facilitate dislocation annihilation [30]. Additionally, for some heteroepitaxy the dislocation density is inversely proportional to the film thickness, so growing thicker is beneficial [31], [32].

Thick buffer layers are more attainable by increasing the film growth rate, which also causes overall growth-related costs to reduce for a device stack. The two most common nitride epitaxial growth techniques are metal organic chemical vapor deposition (MOCVD) and molecular beam epitaxy (MBE). MOCVD and MBE growth rates are typically between 1-3 μm/hr and < 1 μm/hr, respectively, but the MBE growth rate has been recently demonstrated up to ~10 μm/hr [33]. The MOCVD technique is most commonly chosen for commercial production of LEDs for a variety of reasons such as the MOCVD reactor's ability to operate at high temperatures while also avoiding the requirement of ultra-high vacuum (UHV) which is necessary for MBE. The MBE technique typically provides active nitrogen to the surface via either "cracking" of ammonia (NH_3) gas on a suitably hot growth substrate ~700 °C, or via a radio frequency (RF) plasma that breaks apart gaseous nitrogen molecules [34], [35]. The plasma-assisted MBE (PAMBE) variant allows for III-nitride growth at substantially lower temperatures as low as ~300 °C, well below both MOCVD and ammonia based MBE. PAMBE is thus capable of increased growth rates and fast buffer growths of all group III-nitride alloys including high indium content and even high quality InN films that can decompose in the typically hotter environments of MOCVD and ammonia-based MBE [36]–[38].

1.3.3 High Indium Content Buffer Layers

High indium content buffer layers are desirable for a variety of reasons, such as trapping non-radiative recombination centers below the active region of an LED, or by providing a low dislocation density and more relaxed substrate. It is reported that InGaN underlayers allow for higher wave function overlap, increased carrier injection, and most

importantly to trap nitrogen vacancies that hinder device efficiencies [39]–[43]. Thick, high indium bearing layers are also desirable for III-nitride solar cell devices which are sensitive to dislocation densities [44], [45]. Although low dislocation density buffer layers such as $In_xGa_{1-x}N$ with high x are ideal for next generation emitters and solar cells, current state of the art commercial LEDs only have a low mole fraction and volume of indium in the form of a quantum well (QW). In order to produce white light, a low indium content QW blue LED is coated with a phosphor to convert some blue light to another longer wavelength such as yellow and combine emission bands resulting in white light [46]. This LED design is chosen because with the MOCVD technique, indium incorporation and composition above ~20% is difficult, due to the incompatibility of the material with the hot substrate requirements for high quality films [47]. As the growth temperature increases, higher indium content materials decompose. The MBE technique has been able to demonstrate growth of $In_xGa_{1-x}N$ for all x [48]–[53]. Even though indium incorporation is easier in MBE, there are still difficulties mainly in the form of phase separation, indium surface segregation, and plasma sensitivity [54]–[61].

Phase separation is when multiple phases of different indium contents form (*e.g.* x = 0.4 and 0.6) when attempting to grow a single phase (*e.g.* x = 0.5) $In_xGa_{1-x}N$ film. Phase separation occurs due to the large dissimilarity in interatomic spacing between InN and GaN (*a* = 3.56 and 3.19 Å for InN and GaN, respectively). The dissimilarity results in two separate phases being more energetically favorable than one [62]. An example of phase separation observed in X-ray diffraction is shown in Figure 1.7. Instead of a single phase of $In_{0.25}Ga_{0.75}N$, both a high In content $In_{0.28}Ga_{0.72}N$ layer and a low In content $In_{0.22}Ga_{0.78}N$ layer are formed.

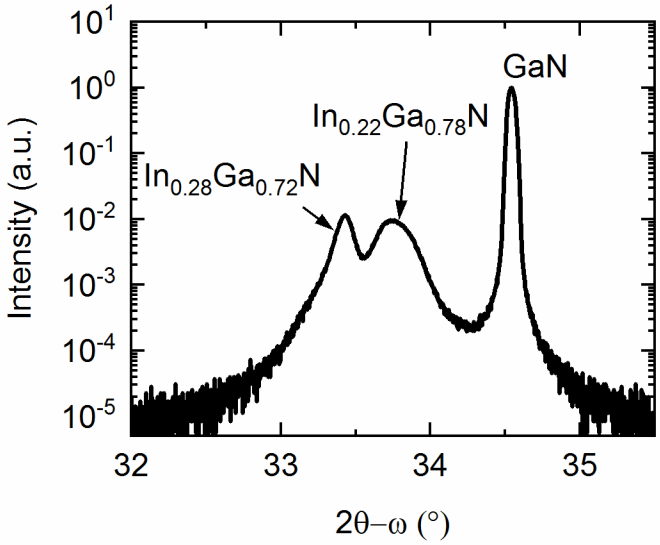

Figure 1.7. X-ray diffraction measurement indicating the presence of phase separation in InGaN grown on GaN. Two phases of low and high In content InGaN are formed when targeting $In_{0.25}Ga_{0.75}N$.

For a multi-quantum well (MQW) LED, a small amount of phase separation actually results in beneficial carrier localization in the higher indium (lower bandgap) regions and can increase radiative recombination and overall device efficiency [63]–[66]. Unfortunately for a thick high indium content bulk layer, phase separation results in additional defects or dislocation generation and harms subsequent epitaxy. Therefore, techniques to avoid phase separation are required for synthesis of structures like solar cells that require thick absorbing layers, or for buffer layers under active regions of an LED or laser.

In addition to phase separation, indium surface segregation is another complication when growing $In_xGa_{1-x}N$ [52], [53]. Most $In_xGa_{1-x}N$ films are grown in the N-rich regime, where there is an excess of nitrogen flux so each Ga and In atom incorporates into the

lattice quickly because of the high availability of nitrogen. This style of growth leads to roughening of the film due to low adatom mobilities [67]. In order to increase the adatom mobility and diffusion length, the film can be grown metal-rich by accumulating In and Ga metal on the surface. If the In metal dose is too high in the metal adlayer, Ga will preferentially incorporate into the lattice and In will segregate to the top of the metal adlayer and can continue to accumulate on the surface. The surface segregation of In results in less indium incorporated into the film and residual indium or InN on the surface after growth, a major problem for subsequent epitaxy from a buffer layer.

Although the plasma-assisted MBE approach is capable of growing $In_xGa_{1-x}N$ for all x, plasma sensitivity of III-nitride films can be problematic, especially for high indium content materials. Generally, as the bandgap and bond strength of the semiconductor decreases, the sensitivity of the material to high energy plasma particles increases. The most common plasma-assisted MBE technology is a radio-frequency (RF) plasma, which replaced the previous electron cyclotron resonance (ECR) plasma. The RF PAMBE has been demonstrated to improve crystal quality of GaN when compared to ECR grown films [35]. Unfortunately, even RF plasmas can cause damage to the group III-nitrides, particularly high indium and low bandgap films.

These multiple phenomena have prevented thick, single phase, and high indium content III-nitride development. For example, an $In_xGa_{1-x}N$ single junction solar cell designed for an optimal conversion of the solar spectrum would requires thick synthesis of a challenging composition of $x = 0.55$ to achieve a bandgap of 1.5 eV [68]. Because of these growth related issues previously discussed and others such as polarization fields limiting carrier extraction, these devices have not been successfully realized and $In_xGa_{1-x}N$

solar technology is limited to a few percent efficiencies [69]–[74].

1.3.4 P-type Doping III-Nitrides

Another major challenge in the III-nitrides is p-type doping with magnesium (Mg). The main difficulties are Mg incorporation into the film, activation of the Mg impurities to produce holes, and self-compensation of the holes by donor-like defects. First, for conventional growth techniques such as MOCVD and MBE the elevated growth substrate temperatures can result in incomplete sticking and incorporation of Mg [75]. Second, the activation energy of incorporated Mg is extremely high, for example it is measured to be ~170 meV for Mg-doped GaN and 510 meV for AlN [76]. Third, donor-like defects of Mg or Mg-H complexes can self-compensate the hole concentrations of the films and thus for the MOCVD technique, an activation anneal is required to out-diffuse hydrogen [77]–[79]. Excess Mg can even cause structural damage in the form of inversion domains and pyramidal precipitates [80], [81]. A pyramidal defect in Mg-doped GaN is shown in Figure 1.8 [81].

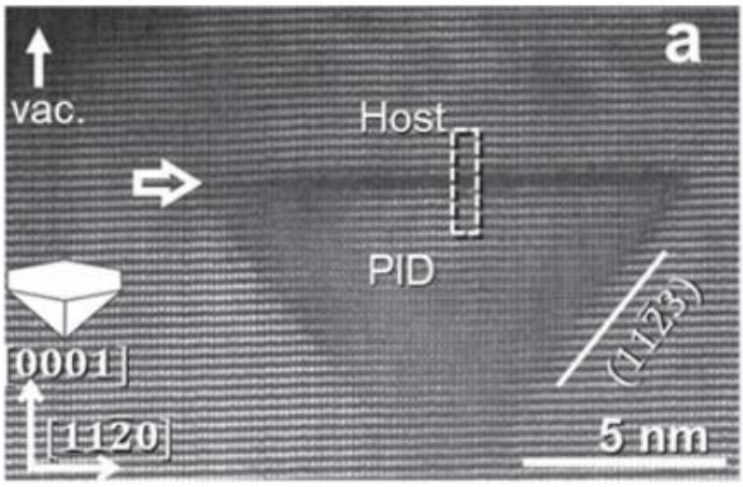

Figure 1.8. TEM image of a pyramidal defect in Mg-doped GaN [81].

These difficulties combine to limit p-type doping for traditional techniques to the low 10^{17} - 10^{18} cm^{-3} range [82]–[85]. The low hole concentrations affect device performance such as an LED by asymmetric carrier injection into the MQW active region resulting in reduced power efficiencies at high current injection referred to as 'droop' and excess electron leakage [86], [87]. In order to combat the asymmetric carrier injection and electron leakage, a multitude of electron blocking layers and other device modifications have been designed to increase radiative recombination [88]–[91]. The asymmetric carrier injection issue gets more severe for shorter wavelength emission such as DUV devices where the hole injection is claimed to be the primary source of low power efficiencies [92]–[94]. The lack of heavy p-type doping has limited device performance, but also hindered the maturity of III-nitride tunnel junctions (TJs).

Tunnel junctions have been investigated in various material systems for decades ever since Esaki discovered the negative differential resistance phenomena for a heavily doped germanium p/n junction in forward bias [95]. After Esaki's initial discovery, tunnel

junctions have been incorporated and are essential to a large variety of devices such as high frequency oscillators and amplifiers, multi-junction solar cells, laser diodes, and LEDs [96]–[100]. An Esaki tunnel junction is a heavily doped p++/n++ junction where the extreme doping results in a very narrow depletion width. The narrow depletion width enables tunneling of electrons between the valence and conduction bands in reverse bias and even in low forward bias. In order to decrease the depletion width and thus increase the tunneling probability, the doping concentrations and/or the built-in voltage must be increased. However, the built-in voltage and often the dopant activation energy both increase with increasing bandgap. Therefore, forming homojunction Esaki-style TJs in wide bandgap semiconductors such as GaN (E_g = 3.4 eV) is a significant challenge.

Due to the inefficient p-type doping and the large bandgaps of many III-nitride compounds, some groups have implemented polarization engineered tunnel junctions to reduce the tunneling distance and increase the tunneling probability for carriers [101]–[103]. This is possible because the wurtzite III-nitrides have large spontaneous and piezoelectric polarization fields. By inserting an interlayer such as AlN or InGaN at the TJ between the n++ and p++ GaN layers, the polarization discontinuity bends the valence and conduction bands to effectively reduce the tunneling distance. An InGaN interlayer tunnel junction diode and its corresponding band diagram is illustrated in Figure 1.9. The band diagram reveals how polarization engineering can reduce the tunneling distance for carriers.

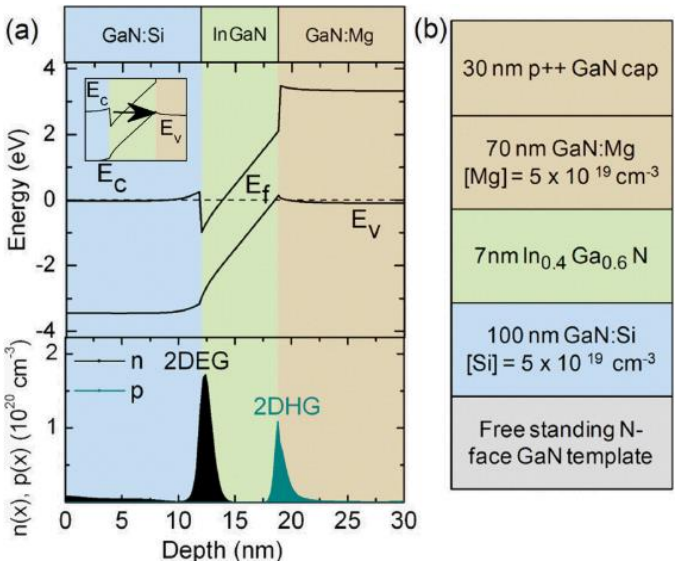

Figure 1.9. Band diagram and device structure for an InGaN interlayer tunnel junction [103].

Although the polarization engineered interlayer approach has been demonstrated to reduce TJ resistance, it can cause growth window complications, generate additional defects from lattice mismatch, and cause optical absorption loss in the lower bandgap interlayers.

Tunnel junctions for the III-nitrides have been implemented mainly as tunnel contacts (TCs) to p-type layers, which is achieved by replacing the p-type metal contact with an n-type nitride layer to form a tunnel junction plus an n-type metallization [104]–[107]. The TJ and n-type metallization allow for increased current spreading by avoiding the large p-type contact resistance and sheet resistance. A TC design simplifies device fabrication by enabling both the top and bottom contact metallization and lithography to be done at the same time (with a modified lithography mask), removing the p-type lithography and metallization step. Both LEDs and laser diodes with TCs for hole-injection have been successfully demonstrated to reduce contact resistance and optical loss. TJs have also been demonstrated to series-connect devices. Interlayer-based TJs have been utilized

to series connect two III-nitride LEDs, solar cells, and even laser diodes [100], [108], [109].

Although first demonstrations of TJs in a variety of device designs has been accomplished, many of the TJ-based devices in literature suffer from large voltage and power penalties required to turn-on or drive the TJ. This loss is mainly due to a lack of extreme p-type doping concentrations due to Mg's high activation energy. Notably, the MOCVD technique used for commercial LED production is unable to form as-grown activated p-type layers that are buried in a TJ-based device. Thus, development of heavy p-type doping and wide-bandgap III-nitride TJ designs are essential to realize next generation devices.

CHAPTER 2: OBSERVATION AND MITIGATION OF RF-PLASMA-INDUCED DAMAGE TO III-NITRIDES BY MOLECULAR BEAM EPITAXY

2.1 Introduction

The III-nitrides demonstrate a band gap as low as ~0.7 eV for InN [110], a high light absorption coefficient [111], and a high radiation resistance [112] which are all desirable for a variety of optoelectronic devices such as light emitting diodes (LEDs) and solar cells.

III-nitride devices are commercially available, such as blue LEDs due to the low indium content used in the $In_xGa_{1-x}N$/GaN quantum well active layers ($x < 0.15$), resulting in a low lattice-mismatch between the $In_xGa_{1-x}N$ quantum well and GaN barrier and high electron-hole wave function overlap. Increasing the indium content in both the quantum wells and barriers can enable longer wavelength emission while minimizing the generation of additional lattice-mismatch induced defects in the active layer. Thus, high indium content $In_xGa_{1-x}N$ with low defect densities, and single-phase crystallinity are essential to realize the next generation of long wavelength III-nitride multi-quantum well (MQW) LEDs.

In addition to LEDs, III-nitride solar cells have been demonstrated with active layers consisting of either $In_xGa_{1-x}N$/GaN MQWs [74], [113], [114] or single semi-bulk $In_xGa_{1-x}N$ [69], [115]. In order to optimally design single junction and tandem $In_xGa_{1-x}N$ solar cells for optimal utilization of the solar spectrum, $In_xGa_{1-x}N$ absorbing layers with x

> 0.5 is required [68]. Presently, $In_xGa_{1-x}N$ solar cells are limited in photovoltaic performance with efficiencies less than 4% [116] primarily due to the limited indium content, and the poor crystal quality of the active layer and, thus, low carrier extraction efficiency. Therefore, improving the crystal quality of high indium content III-nitrides is essential for next generation LEDs, solar cells, and other optoelectronic devices.

III-nitride molecular beam epitaxy typically uses one of two nitrogen sources. In one form, ammonia is supplied to the growth surface and thermally "cracked" to provide active nitrogen to the crystal. Achieving high quality films via ammonia-based MBE becomes significantly more challenging at low growth temperatures due to the inefficient cracking of nitrogen [117]. The high growth temperatures in ammonia-based MBE required to growth high quality nitride-based films is not suitable for the growth of high indium content $In_xGa_{1-x}N$ films. However, plasma-assisted molecular beam epitaxy (PAMBE) which utilizes a radio frequency (RF) plasma source to dissociate gaseous molecular nitrogen can be extended to colder substrate temperatures as low as 275 °C for InN [48] and is thus capable of growing single phase $In_xGa_{1-x}N$ for all x from $0 \leq x \leq 1$ [49], [51], [53].

For III-nitride films, as the indium content increases, the band gap decreases, and, thus, the bond strength decreases. As the bond strength decreases, the film becomes more susceptible to plasma-induced damage. Crystal damage during the growth arises from impinging high kinetic energy particles which, in turn, result in enhanced decomposition, desorption of adatoms, and an increase in surface dangling bonds. The mentioned drawbacks can detrimentally reduce the surface diffusion length and may even prevent step-flow growth. Given the PAMBE nitrogen sources are remote sources with low energy

ions, typically less than 6 eV of kinetic energy filtering out through a series of orifices, any detected ion damage would likely be worsened in direct plasma deposition techniques with high ion energies such as sputtering. Therefore, in order to optimize III-nitride film quality and realize the next generation of optoelectronic devices, damage from the plasma discharge must be characterized and minimized.

In a PAMBE reactor, typically the plasma chamber is a pyrolytic boron nitride chamber in series with the nitrogen gas source and the growth chamber. The plasma chamber is excited by an RF electromagnetic source able to energetically excite (< ~9 eV) and even crack (> 9.7 eV) molecules of nitrogen producing various populations of excited atomic and molecular nitrogen along with both positive and negative ions and free electrons. When nitrogen flows through the plasma chamber, a conductance limitation enabled by an aperture plate at the plasma chamber outlet results in pressures in the order of millitorr. The RF energy excited gas leaks out into the growth chamber which is operated in the 10^{-5}-10^{-6} Torr pressure range. Along with the excited neutral charged gas emission through the aperture plate, both electrons and ions escape and all species are directed in a molecular beam (essentially collisionless) toward the substrate. Since the vacuum acts as a dielectric capacitance and the substrate is typically grounded to the chamber potential, the relative differences in the positive to negative species (positive ions, negative ions, and electrons) emission rates induce a net "floating potential" in steady state between the chamber/substrate and the plasma itself. Direct bombardment of ions from inside the plasma to the substrate is limited by the aperture plate containing narrow holes, and so the primary source of acceleration energy for any ions towards the substrate is from the floating potential. The nature of the plasma discharge is determined primarily from the plasma bulb

geometry, the size of each hole and conductance of the collection of holes in the aperture plate, the input nitrogen gas flow, and the applied plasma power [35]. Specifically, the plasma pressure in the bulb is determined by the flow rate and the conductance of the aperture determines the mean free path for plasma collisions, and in large part, the acceleration potential. The geometry of the plasma bulb as well as the number of holes in the aperture plate modify the bulb volume and conductance [33]. A wide range of applied plasma powers and nitrogen gas flows are used to study the optical and electrical characteristics of the plasma discharge and the crystal quality of the grown films.

The plasma discharge can be electrically characterized *in-situ* via a Langmuir probe [118], [119]. The current-voltage characteristics of the Langmuir probe can reveal the positive and negative ion contents and the ion acceleration potential, which is the voltage induced between the plasma and the substrate. Reducing the ion content, and minimizing the ion acceleration potential has been demonstrated to improve III-nitride film quality [120].

The optical behavior of the plasma can be characterized via optical emission spectroscopy (OES) through the rear plasma window port. OES provides a qualitative understanding of the molecular and atomic nitrogen species in the plasma. It is shown that the ratio of the molecular and atomic nitrogen species in the plasma changes by varying the input nitrogen flow and applied plasma power [121]. The optical characteristics of the plasma measured by OES are weighted by the transmission properties of the rear plasma window and the PBN bulb.

OES measures both excited molecular and atomic nitrogen species, but cannot distinguish between ionic and neutral excited species. In contrast, a Langmuir probe can

measure the charged particles in the form of ions and electrons, but cannot distinguish between molecular and atomic ions. Plasma characterization is best performed when combining these two techniques while recognizing their individual limitations.

In this work, InN, possessing the weakest molecular bond strength (7.72 eV/bond in the bulk) of the III-nitrides (compared to 9.12 and 11.52 eV/bond of GaN and AlN, in the bulk, respectively), is utilized as a sensitive material to characterize and optimize the plasma discharge [122]. It is important to note that the surface bond energies may be significantly less than those of the bulk due to local near-surface crystalline softening and chemical catalytic energy additions. Thus, the plasma-induced damage in InN films needs to be isolated from other potentially damaging effects which can also generate defects in the film. These effects primarily include roughening due to low adatom mobility, InN decomposition, and indium desorption.

The Langmuir probe, OES, and InN crystal quality data are combined to provide insight and guidance towards optimal plasma conditions which minimize plasma damage of high indium content III-nitrides films.

2.2 Experimental Procedure

In this study, a Riber 32 PAMBE reactor is employed to study the nitrogen plasma discharge and grow nitride-based films. GaN templates on sapphire were chosen as substrates. The templates were first backside metallized with 2 μm of tantalum to ensure temperature uniformity during the growth. Next, the templates were cleaned with a two-

stage piranha clean consisting of 3:1 of H_2SO_4:H_2O_2 followed by a DI water rinse. The substrates were then loaded into an introductory chamber and outgassed at 200 °C before loading into the growth reactor. Inside the growth reactor, indium and gallium fluxes are supplied via a standard effusion cell and a Veeco dual-filament SUMO cell, respectively. A Veeco UNI-Bulb RF nitrogen plasma source was used to supply various nitrogen flows and powers ranging from 2.5 to 12.5 sccm and 350 to 550 W, respectively. The plasma source was equipped with an aperture plate containing ~2000 holes drilled with a #80 drill bit (0.0135" diameter). This is roughly half the total conductance used in our previous work that resulted in GaN growth rates of 9.8 um/hour [33]. The plasma optical emission spectrum was monitored *in-situ* via an Ocean Optics HR-2000+ES spectrometer through both a rear window and the pyrolytic boron nitride (PBN) bulb. The flux gauge collector terminal is repurposed as a Langmuir probe and placed in a position that matches the film growth position, in order to accurately characterize the plasma in the growth environment. A Keithley 6517A electrometer is connected to the collector pin feedthrough to sweep the voltage between -100 and 100 V and sense current. Growths were achieved by utilizing the metal modulated epitaxy (MME) growth technique, presented in our previous works [48], [123]. Reflection high energy electron diffraction (RHEED) was used to monitor the MME growths *in-situ*.

2.3 Results and Discussion

2.3.1 Observation of Plasma Damage

The sensitivity of nitride-based surfaces to the plasma discharge is first studied by comparing the surface quality of GaN and InN films which were exposed to the plasma discharge post-growth with a nitrogen plasma input flow of 2.5 sccm and an applied RF power of 350 W. Figure 2.1 compares AFM and RHEED images of GaN and InN surfaces before and after exposure to the plasma discharge for 5 minutes at growth temperatures of 600 and 300 °C for the GaN and InN films, respectively. The GaN surface shows a negligible difference in morphology when exposed to the post-growth plasma discharge, whereas the InN surface exhibits significant texturing. It should be noted that exposure of the plasma to the GaN surface for even a few minutes resulted in a rising specular RHEED spot intensity associated with slight surface roughening, as seen in Figure 2.1. Longer post-growth plasma exposure (*e.g.,* one hour) of GaN resulted in a significant surface roughening.

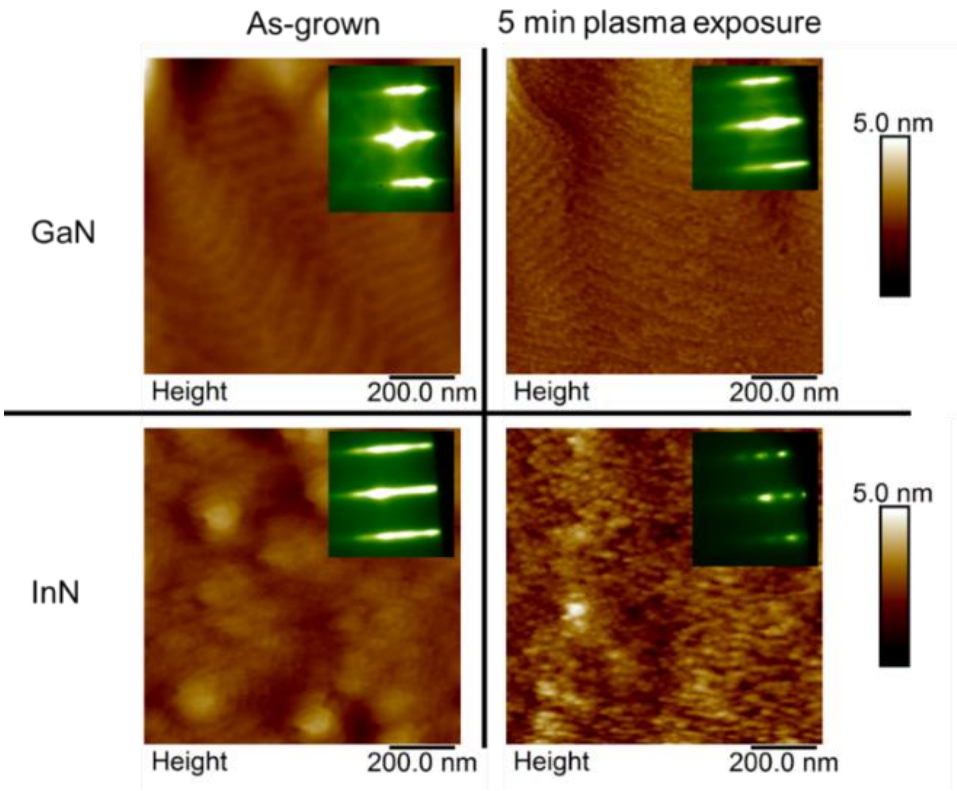

Figure 2.1. AFM images of as-grown and post-growth plasma exposed GaN and InN films. The InN surface is degraded by plasma exposure (inset: associated RHEED images.)

2.3.2 Development of an InN Growth Window to Isolate Plasma Damage

InN film quality can be deteriorated due to a variety of thermal related factors such as high growth temperatures resulting in indium desorption and/or InN decomposition and low growth temperatures resulting in low adatom mobility. In order to isolate the effects of the plasma damage on the InN film quality, a temperature growth window, free of the mentioned thermal related effects, was first established. Figure 2.2 illustrates the onset of each thermal related effect and their associated RHEED patterns. First, at low substrate temperatures (*e.g.*, 225 °C), the indium adatom mobility is low, which results in the surface roughening and spotty RHEED patterns. Next, when the substrate temperature is set to

greater than 250 °C (*e.g.*, 300 °C) the film exhibits a 1 x 1 RHEED streaky pattern and, thus, a smoother InN surface. Finally, at higher growth temperatures (*e.g.*, 450 °C), the RHEED patterns dim due to the accumulation of excess indium metal on the surface, which scatters/blocks the electron beams as a result of InN decomposition.

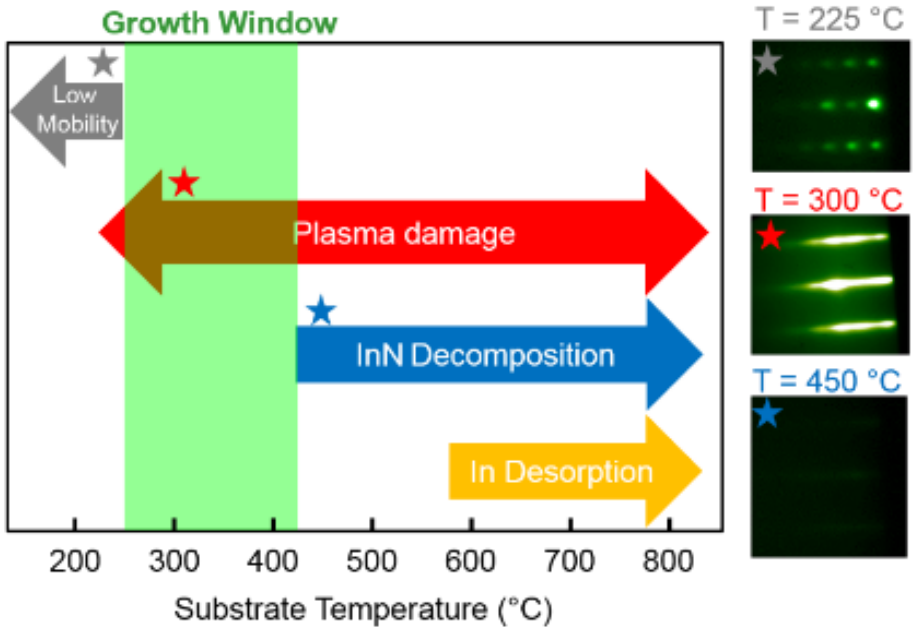

Figure 2.2. Substrate growth temperature window for MME InN for isolation and characterization of the plasma damage effects. The RHEED images indicate a rough surface for substrate temperatures that are low and InN decomposition for substrate temperatures that are high.

The onset of InN decomposition and indium desorption were analyzed to determine a more accurate temperature boundary and extract their corresponding activation energies. First, InN decomposition was studied by growing InN via MME with a growth temperature of 360 to 430 °C. When InN decomposes into indium and nitrogen species, the indium metal remains on the surface and contributes to the total metal dose as long as the growth temperature is lower than the temperatures at which indium desorbs from the surface. For

a constant plasma condition and, thus, nitrogen flux, the excess indium introduced from the decomposition of the underlying InN film can be quantified by measuring the additional time required to consume the total metal dose when compared to lower growth temperatures less than 360 °C without indium decomposition. RHEED transients show that the InN decomposition rate increases by increasing the growth temperature, leading to a longer metal consumption times (see Figure 2.3). As seen in Figure 2.3, by increasing the substrate temperature, the duration of the highlighted region, associated with the decomposed In metal from the underlying InN layers, increases.

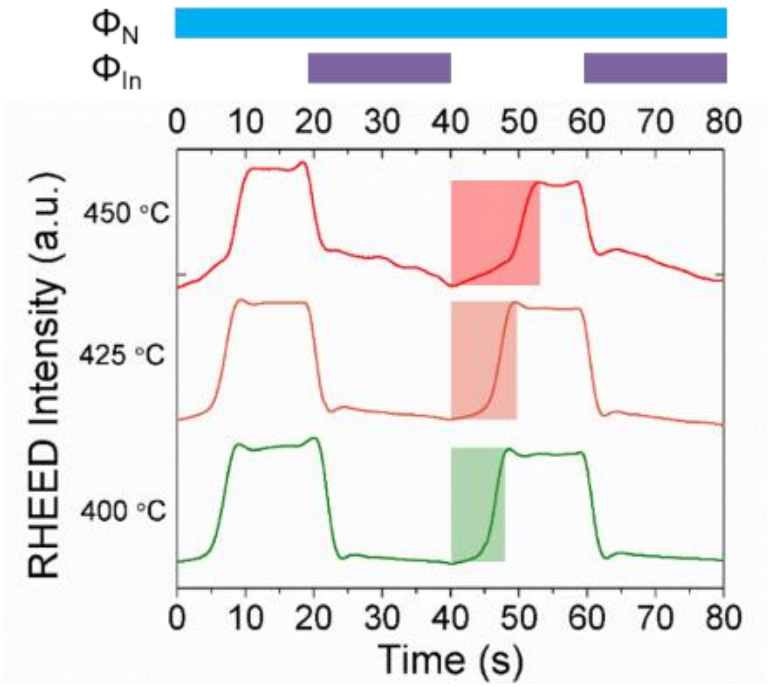

Figure 2.3. MME RHEED intensity transients during the growth of InN at different substrate temperatures where InN decomposition occurs. At higher growth temperatures, InN decomposition contributes additional indium metal to the surface.

The increased amount of time required to consume the indium metal on the surface can be converted into an excess flux of indium in atoms/cm^2. Figure 2.4 illustrates the

exponential nature of the decomposition flux vs substrate temperature. The extracted InN decomposition activation energy is ~1.77 eV which is close to the previously reported value of 1.78 eV [124].

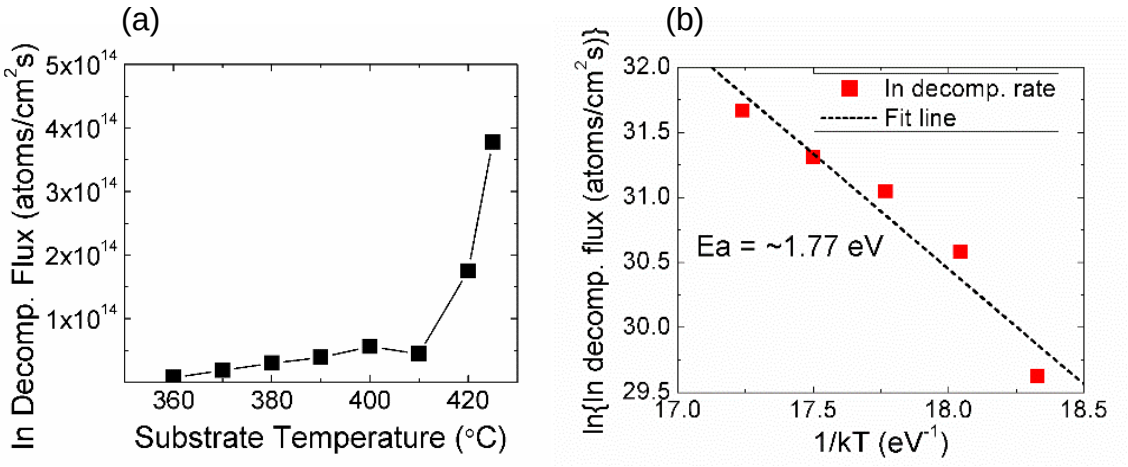

Figure 2.4. InN decomposition flux in the form of excess In flux (atoms/cm^2) present on the surface at various substrate temperatures for both (a) linear and (b) Arrhenius plots.

In addition to the InN decomposition, the substrate temperatures in which indium desorption occurs are identified. Unfortunately, it is difficult to directly measure the indium desorption from an InN surface by RHEED transients due to the InN decomposing at significantly lower substrate temperatures than those required for desorption, as depicted in Figure 2.2. Thus, at first, an indium dose of 5.1 x 10^{16} atoms/cm^2 is supplied to a GaN surface without any supplied nitrogen flux. Subsequently, most of the desorbed indium is indium desorption from the metallic indium surface, and not directly measuring desorption from the GaN surface. Indium desorbing from indium on a GaN surface should provide a rough estimate of the substrate temperature range where significant indium desorption occurs. Figure 2.5 details RHEED intensity transients where the indium dose is evaporated

onto the GaN surface in the first 20 s and then desorbed. As seen, the RHEED intensity falls as the indium accumulates on the surface and rises to its initial value once it is completely desorbed. In addition, Figure 2.5 illustrates that the same amount of indium desorbs faster at higher substrate temperatures.

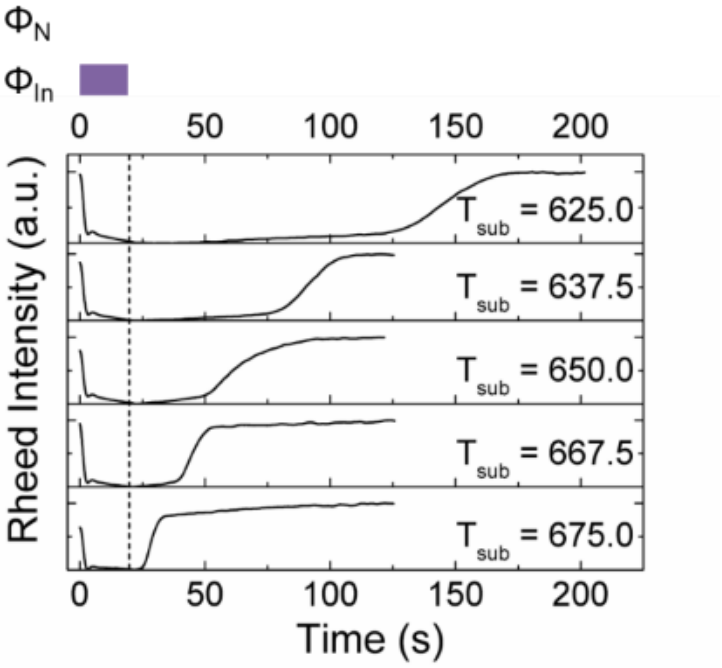

Figure 2.5. RHEED intensity transients after evaporating 5.1 x 10^{16} atoms/cm^2 indium onto a GaN surface for 20 s. RHEED transients illustrate the increasing rates of indium desorption with increasing substrate temperature.

The time to desorb the indium dose on the surface can be then plotted vs substrate temperature (see Figure 2.6). As seen in Fig. 6, the desorption flux exponentially increases with increasing substrate temperature. The Arrhenius plot indicates an indium desorption activation energy of ~2.32 eV, which is most likely indium desorbing from the metallic indium but does closely match with Gallinat *et al.* reported value of 2.49 eV [124].

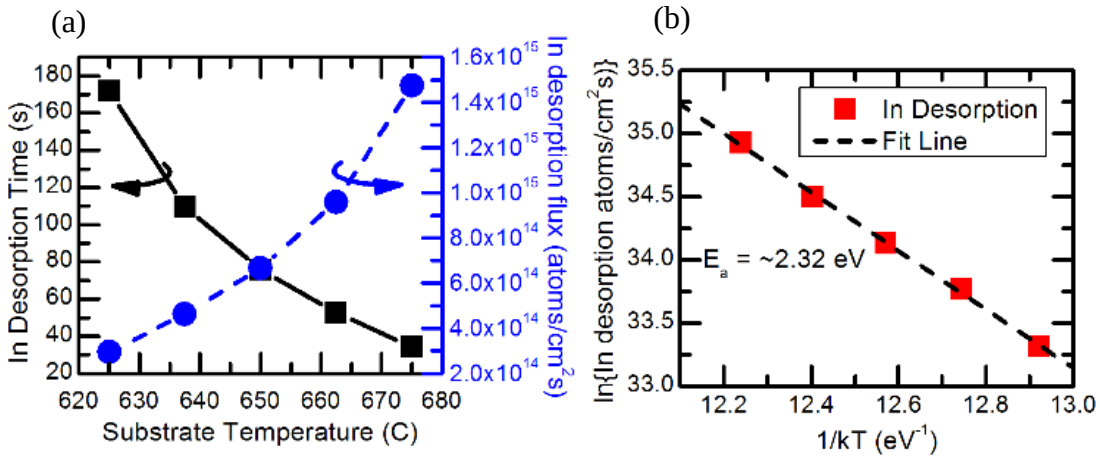

Figure 2.6. (a) In desorption time and associated desorption flux and (b) Arrhenius plot of the desorption flux vs substrate temperature.

By *in-situ* analysis of RHEED patterns and intensity transients, the substrate temperature boundaries for the onset of surface roughening due to low adatom mobility, InN decomposition, and In desorption are established. These temperature boundaries define a growth window for InN containing devices in the range of 250-400 °C. In this work, InN films grown in this window act as a sensitive material to isolate any potential influence of the plasma conditions on the crystal quality.

2.3.3 Characterization of the Nitrogen Plasma with a Langmuir Probe

The plasma is then electrically characterized *in-situ* via the flux ion gauge collector pin repurposed into a Langmuir probe and placed in the growth position. By sweeping voltage and measuring current, any ion/electrons contribute to the total current. At a high reverse (forward) bias, most of the impinging negative electrons (positive ions) are repelled, and mainly the positive ions (electrons) are collected, resulting in a measured positive (negative) current. Since, in this setup, the Langmuir probe is outside the plasma bulb, and the density of the ions and electrons are often uneven, the probe may not collect

an equal contribution of positive ions and negative electrons at zero applied bias. Instead, the plasma bulb will retain a net charge (+Q) that results from excess charge (–Q) ejected from the plasma towards the probe which establishes a steady state acceleration voltage (V_a) according to $Q = CV_a$ (where C is the combined series capacitance of (a) the internal plasma and (b) the vacuum dielectric capacitance). The internal plasma capacitance depends mainly on the plasma chemistry modified by the plasma input conditions and bulb dimensions. The vacuum dielectric capacitance is mainly associated with the aperture to chamber (or sample) location. There corresponds to the series capacitances, a plasma potential (V_p), and a floating potential (V_f). The Langmuir probe bias that cancels the net charge expelled from the plasma and, thus, results in a zero measured current can be identified as V_f. Generally, V_p inside the plasma bulb (internal plasma) is found by the inflection point of the Langmuir probe I-V data in the positive potential region [125]. The difference between V_p and V_f is defined as the ion acceleration potential (V_a). Thus, a Langmuir probe can provide an understanding of the plasma contents, along with the induced ion acceleration potential between the plasma and the sample substrate.

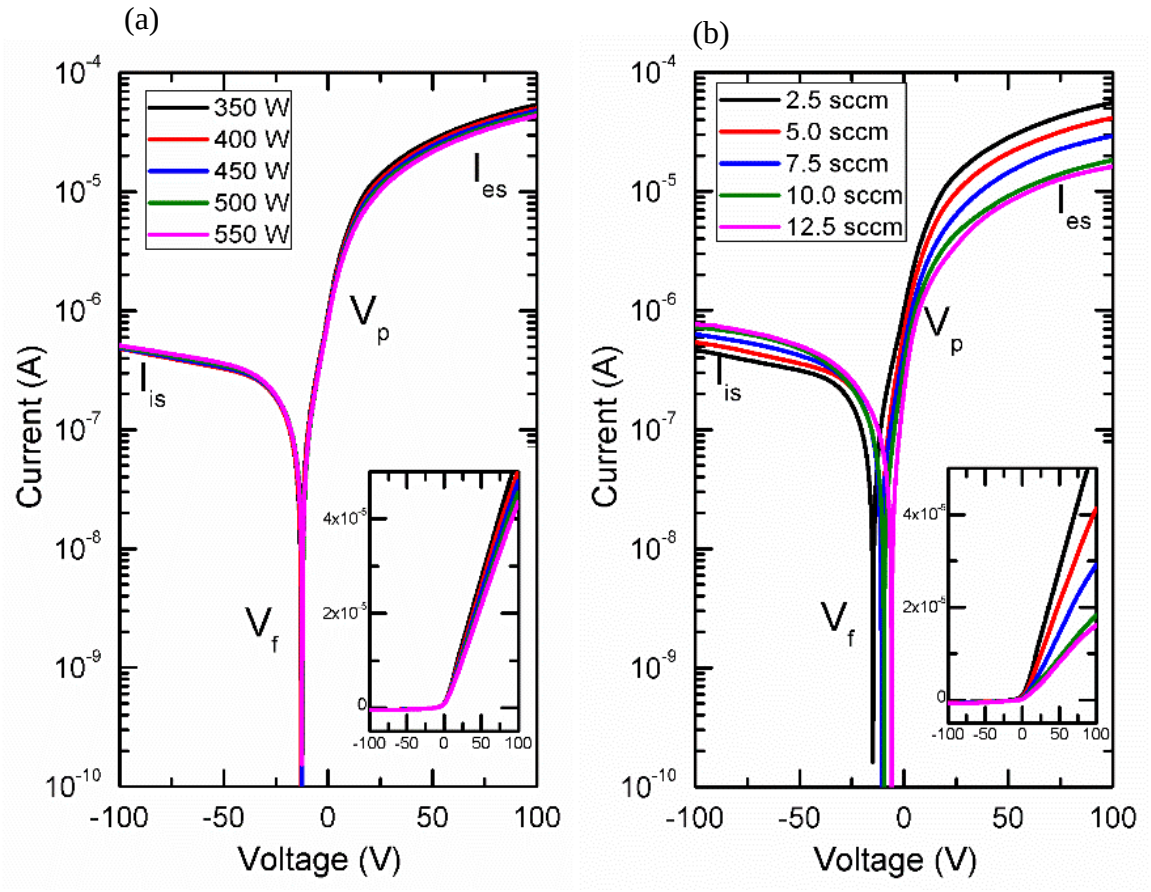

Figure 2.7. Semi-log and linear current-voltage characteristics of the Langmuir probe for different plasma conditions: (a) 350 to 550 W RF applied power with a constant 2.5 sccm N_2 flow and (b) 2.5 to 12.5 sccm N_2 flow with a constant 350 W RF applied power. The ion saturation current (I_{is}), electron saturation current (I_{es}), floating potential (V_f), and plasma potential (V_p), are all labeled.

The Langmuir probe's current-voltage characteristics of the plasma at various power and flow conditions are presented in Figure 2.7. The positive ion saturation current (I_{is}) and negative electron saturation current (I_{es}), the zero-current floating potential (V_f), and the plasma potential (V_p) are all labeled. It is evident that the plasma related parameters (including Ies, Iis, and Va) do not change with increasing plasma power, as the plasma density is proportional to the square root of power. Contrarily, as seen in Figure 2.7(b), an increased nitrogen gas flow results in an increased positive ion content, a reduced negative

ion/electron content, and, thus, a more neutral plasma discharge which lowers the floating potential.

In addition to the floating potential, the plasma potential must be found to determine the overall acceleration potential ($V_a = V_p - V_f$). The plasma potential is best observed when the inflection point is easily identifiable in the current-voltage characteristic. Hershowitz details the best configuration for observing this inflection point when employing a semi-infinite planar probe inside the plasma [126]. Unlike Hershowitz, in this paper, a circular flux gauge collector pin is utilized as a Langmuir probe outside the plasma, and, thus, the current-voltage inflection point and the plasma potential are difficult to extract, as reported by Azooz [127]. However, some of the plasma potential values can be extracted by data smoothing and numerical differentiation of the I-V characteristics, as seen in Figure 2.8.

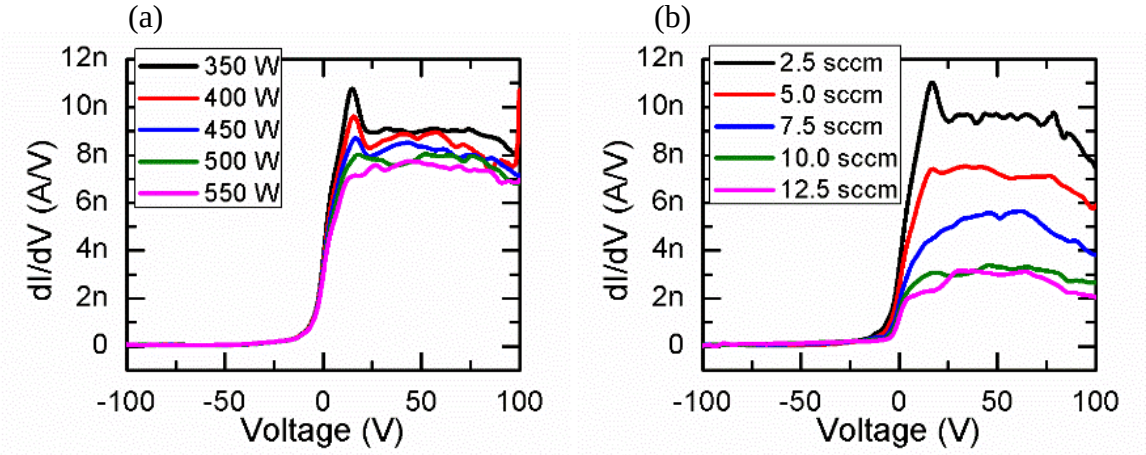

Figure 2.8. A numerical derivative of the Langmuir probe data for various (a) plasma powers and (b) nitrogen flows.

The derivative data shown in Figure 2.8(a), which correspond to the various RF powers and nitrogen flows, have identifiable peaks, associated with the plasma potentials. The floating potential, extractable plasma potentials, and acceleration potential (V_p-V_f) are

plotted in Figure 2.9.

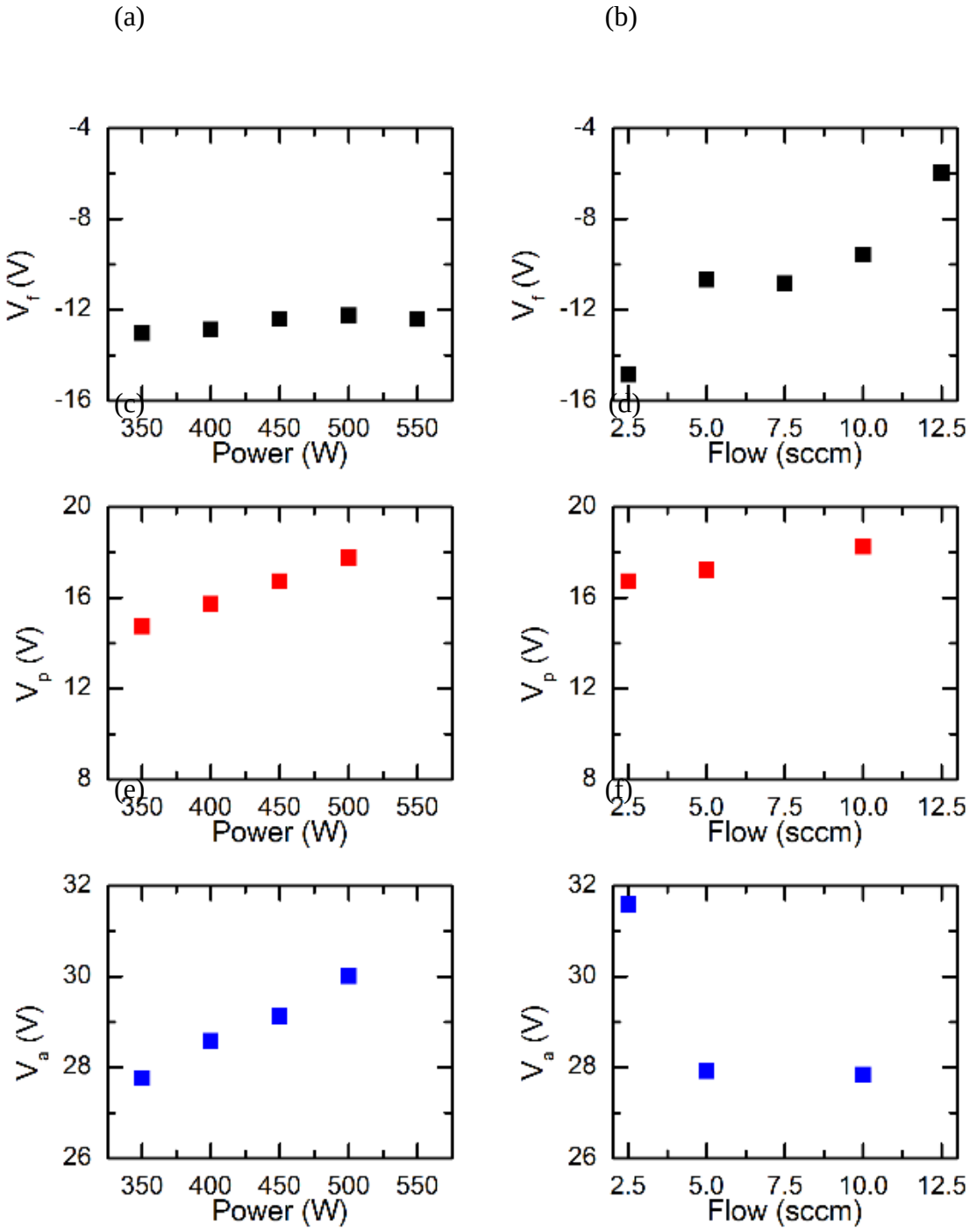

Figure 2.9. Plasma parameters extracted from the Langmuir probe current-voltage characteristics: (a-b) floating potential, (c-d) plasma potentials, and (e-f) acceleration potentials for various RF powers and nitrogen flows.

As seen in Figure 2.9, the magnitude of V_f is significantly reduced (by approximately 8 V) when increasing the nitrogen flow from 2.5 to 12.5 sccm, however, it negligibly changes by increasing the RF power from 350 to 550 W. In addition, the V_p increases by increasing the power and flow, which results in increased plasma density. The increase in the plasma density can be seen in Figure 2.10, as V_p linearly increases with the square root of the RF power.

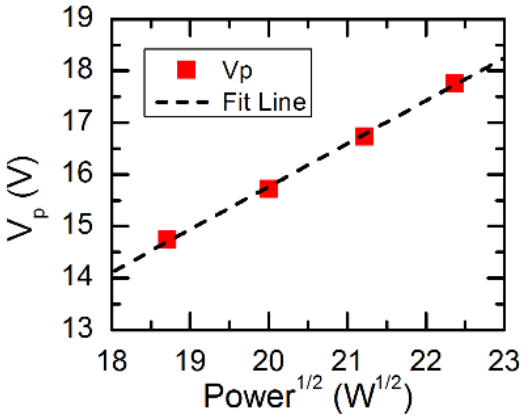

Figure 2.10. Plasma potential vs the square root of the RF power and the associated linear fit.

The combined effects of V_p and V_f result in a rise of V_a by ~1.4 V for an increase in the power from 350 to 500 W and a fall of ~3.8 V for an increase in the nitrogen flow from 2.5 to 10.0 sccm.

2.3.4 Characterization of the Nitrogen Plasma via Optical Emission Spectroscopy

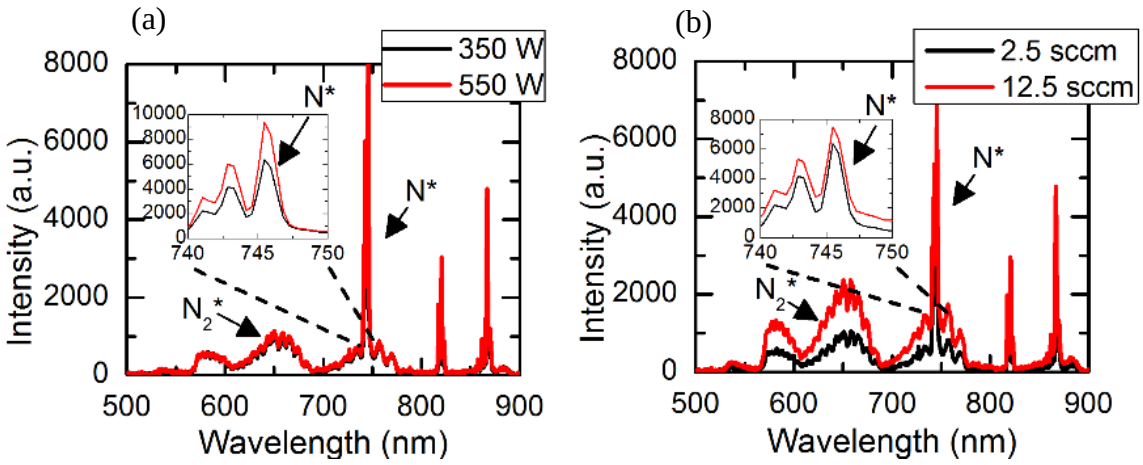

Figure 2.11. Optical emission spectroscopy for different conditions: (a) 350 and 550 W RF applied power with a constant 2.5 sccm N_2 flow, and (b) 2.5 and 12.5 sccm N_2 flow with a constant 350 W RF applied power (inset: a narrow wavelength range (740-750 nm) to view excited atomic nitrogen peaks).

The excited molecular (N_2^*) and atomic nitrogen (N^*) contents of the plasma are extracted from the OES data. The broad and low intensity peaks, displayed in Figure 2.11(a) and Figure 2.11(b), are excited molecular nitrogen, while the sharp and narrow peaks are associated with excited atomic nitrogen [35], [121]. The spectrum lines of 582 and 745 nm are chosen as representatives of N_2* and N*, respectively. Figure 2.12 displays atomic and molecular peak intensities vs plasma power and flow. Interestingly, the atomic peak intensity monotonically increases with increasing power, as seen in Figure 2.12(a), but saturates at high flows (see Figure 2.12(b)). Additionally, the molecular peak intensity has little correlation with increasing power (see Figure 2.12(c)), but monotonically increases with the increasing flow (see Figure 2.12(d)). While the excited atomic nitrogen peak intensity is much higher than the molecular nitrogen in Figure 2.11 and Figure 2.12, the integral width of the spectra is dominated by the molecular species suggesting that the atomic nitrogen percentage of the plasma is relatively small.

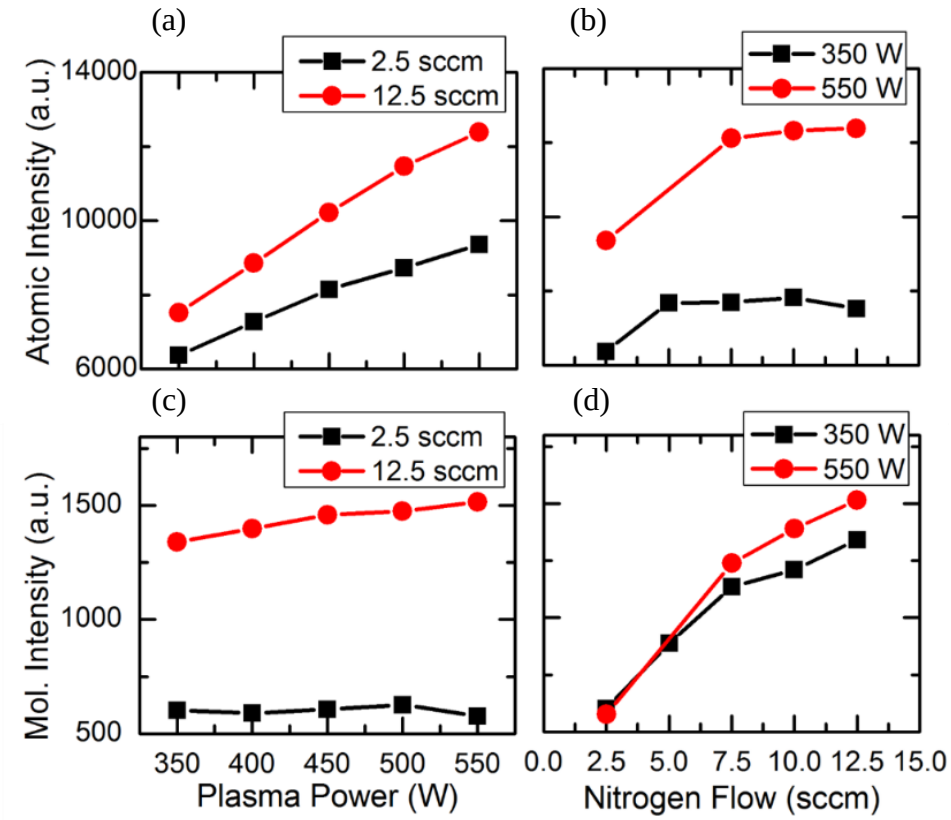

Figure 2.12. Peak OES intensity data for various plasma conditions at (a-b) atomic 745 nm emission and (c-d) molecular 582 nm emission.

By comparing the OES and Langmuir probe data, one can conclude that by raising the plasma RF power, the significant rise in N* only results in a slight increase of positive ion content and V_a. The negligible difference in Langmuir probe data would imply that the percentage of the total plasma density and the ion content of the plasma are minimally affected by the atomic nitrogen content and this is consistent with the growth rate data which will be presented later. As will be also shown later, even though the atomic nitrogen content does not dominate the plasma characteristics, it correlates to the defect concentration of the films and, likely, is the source of surface roughening, observed in Figure 2.1, and the unintentional background electron concentrations of InN films.

Next, the effects of increasing the plasma nitrogen flow on the OES and Langmuir

probe data are compared. The large increase in excited molecular nitrogen content from an increase in flow results in a larger positive ion content and reduced ion acceleration potential. At first, the increase in positive ion content with the increased flow may appear disconcerting. However, it is accompanied by a significant decrease in the acceleration potential responsible for the kinetic energy of ionized species that potentially causes degradation of the film quality. This is not surprising as the increased flow results in increased plasma bulb pressure and, thus, a decrease in the mean free path, described by Eq. (1), where the mean free path (l) is calculated from the Boltzmann constant (k), the temperature (T), the pressure (p), and the molecular diameter (d_m^2). This equation dictates that the smaller atomic nitrogen will have a longer mean free path than molecular nitrogen, thus, traveling longer before being scattered, leading to higher kinetic velocities.

$$l = \frac{kT}{\sqrt{2}\pi p d_m^2}, \qquad (1)$$

The drop in the mean free path with higher flow results in increased scattering within the plasma bulb, limiting the kinetic energy of species and consequently lowering the floating potential of the remote plasma (over 8 V for an increase in flow from 2.5 to 10.0 sccm). The conductance of the aperture of the plasma bulb sets operational limits over which the plasma can be sustained. For the aperture used in this study, the pressure in the plasma bulb ranges from 1.5 to 7.4 mT and, consequently, a molecular nitrogen mean free path of 31 to 6 mm for a flow rate of 2.5 to 12.5 sccm. The atomic nitrogen mean free path for the same flow range, assuming independent gas species (for comparison purposes only), varies from 1,400 to 270 mm. Below the lower pressure limit, the plasma density is

insufficiently high to support a plasma. At these lower flows, the acceleration potential is substantial due to the longer mean free path and, thus, higher obtainable scattering limited kinetic energies. At higher plasma pressures, the plasma mean free path is insufficiently long to allow energy transfer, thus, extinguishing the plasma. However, at the upper end of the allowable flow, the floating and acceleration potentials are substantially lower resulting in (as will be shown below) minor film damage. In a similar way, as the electrical conductance of the path from the aperture of the plasma to the sample (chamber ground) is increased by increased flow, the floating potential drops significantly due to the inability to support large voltages across a highly conductive remote plasma glow.

2.3.5 Growth of InN films to Determine Optimal Plasma Conditions

After optical and electrical characterization of the plasma, InN films are grown at various plasma conditions. Seven ~1 μm-thick InN films were grown via MME on GaN templates to determine the effect of plasma power and nitrogen flow on the material quality. First, three films were grown with a nitrogen flow of 2.5 sccm and varied plasma powers of 350, 450, and 550 W. Next, four additional films were grown with a standard plasma power of 350 W and nitrogen flows of 3.75, 5.0, 6.25, and 7.5 sccm. The InN films' surface morphologies, X-ray diffractograms, background electron concentrations, and photoluminescence spectra are compared to elucidate the origin of the plasma damage, and predict optimal growth conditions. A representative x-ray diffraction scan of an InN grown film at ~4.0 μm/hr is shown in Figure 2.13. All InN films resulted in the (0002) omega rocking curve full width at half maximum (FWHM) values between 137 and 167". In addition, the $(10\bar{1}5)$ omega rocking curve FWHM values are between 316 and 337" for

all films. This is the fastest grown InN film with the lowest XRD FWHM figures of merit when compared to the current literature.

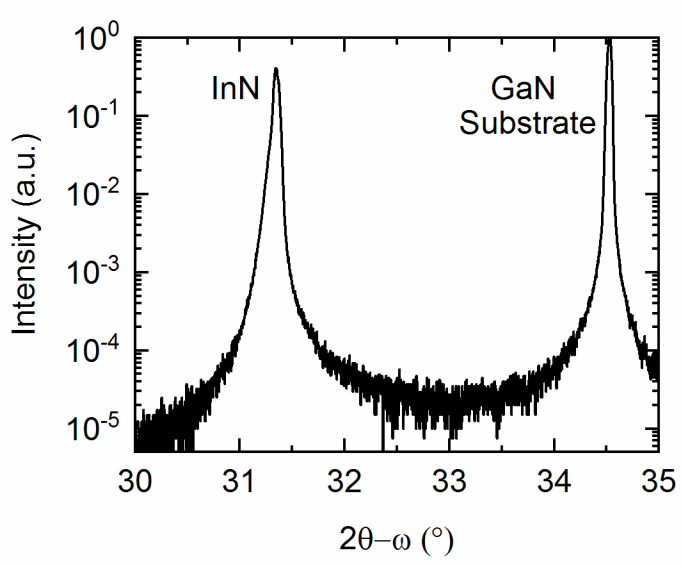

Figure 2.13. X-ray diffraction 2theta-omega for (0002) InN grown at ~4.0 µm/hr and the underlying GaN substrate.

A 5 x 5 μm^2 AFM image of the sample with the highest growth rate (grown with 350 W RF plasma power, 7.5 sccm N_2 flow and a corresponding growth rate of ~4.6 µm/hr) is shown in Figure 2.14. The film shows a RMS roughness of ~0.9 nm and a smooth spiral-hillock surface morphology, which is observed for all the grown InN films. Notably, the MME growth method with high growth rates yields high-quality InN films.

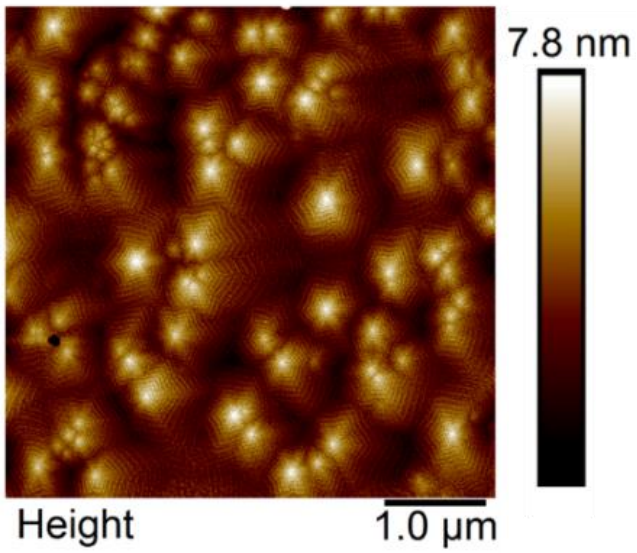

Figure 2.14. A 5 x 5 μm^2 AFM image of an InN film grown at 4.6 μm/hr exhibiting a 0.9 nm RMS roughness.

Since both ion damage and background contamination can affect the unintentional electron concentration, the films' growth rate and background electron concentration are compared, as shown in Figure 2.15, for both power and flow rate variations. The plasma condition of 350 W and 2.5 sccm nitrogen flow resulted in a growth rate of 2.01 μm/hr and a background electron concentration of 1.36 x 10^{19} cm^{-3}. Growing an InN film with a plasma power of 550 W with 2.5 sccm nitrogen flow increased the growth rate up to 2.54 μm/hr, and the background electron concentration escalated to 1.49 x 10^{19} cm^{-3}. Interestingly, when growing a film with a nitrogen flow as high as 7.5 sccm, the resulting growth rate was 4.58 μm/hr, and the background electron concentration reduced significantly to 3.54 x 10^{18} cm^{-3}, unlike the trend for increasing plasma power. As a) both the residual background electron concentration and b) the change in electron concentration as a function of flow and, thus, growth rate are higher than expected for contamination, it is likely that the residual electron concentration is controlled predominantly by the ion

damage. For example, when the growth rate increases from 2.01 to 4.58 µm/hr (by a factor of 2.28), the residual electron concentration drops from 1.36 x 10^{19} cm^{-3} to 3.54 x 10^{18} cm^{-3} (by a factor of 3.84). The reduction in the unintentional electron concentration suggests that the defect density in InN is controlled largely by the ion damage.

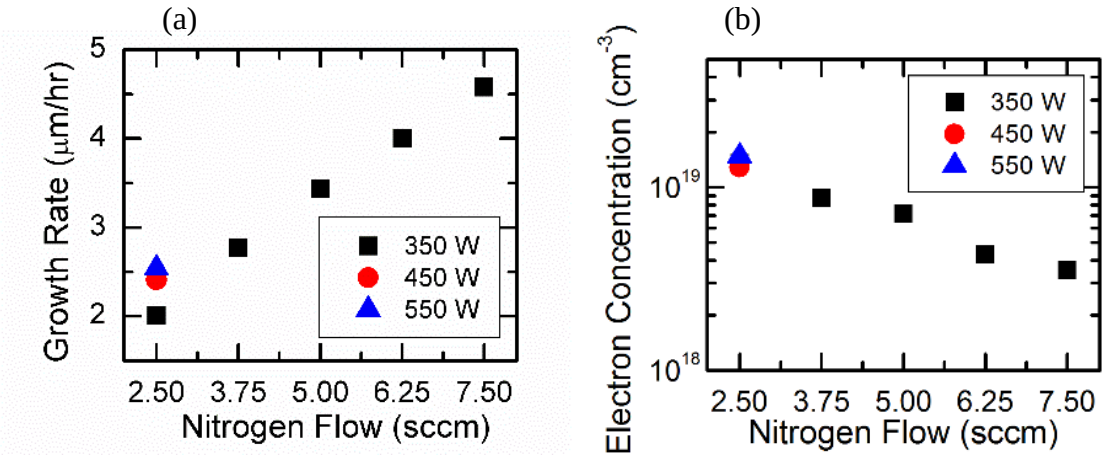

Figure 2.15. Comparison of (a) growth rates and (b) background electron concentrations for InN films grown at various nitrogen flow rates and plasma powers.

The increase in background electron concentration with increasing power may be attributed to the increase in atomic nitrogen species, as evident in Figure 2.12(a), with a negligible increase in the molecular content, as shown in Figure 2.12(c). The ion acceleration potential in Figure 2.9(e) is also slightly increased with increased power. Thus, it is speculated that a larger ratio of atomic nitrogen to molecular nitrogen as well as an increased acceleration potential can cause damage to the crystal which results in a higher background electron concentration, similar to previous work for GaN [35].

2.3.6 Photoluminescence of InN Films

Photoluminescence (PL) spectra at low temperature (4 K) and room temperature were taken for all seven InN films, as seen in Figure 2.16. The low temperature spectrums seem to be made up of two components: one invariant to changes in electron concentration and one dependent on electron concentration. The films' spectra show an emission at 0.77 eV which is invariant to electron concentration, well above the fundamental bandgap energy of ~0.65-0.7 eV for InN [128]–[130]. The 0.77 eV peak is also present in room temperature PL. While a future, more in-depth PL study is planned, it is presently speculated that the 0.77 eV emission is associated with the surface electron accumulation layer due to the commonly reported fermi-level pinning observed in InN [131]. At low temperatures, a second peak is also observed that varies with electron concentration. This peak is likely the band-to-band, or possibly the previously reported band-to-acceptor transition [132], [133] and can be seen varying from ~0.81 to 0.71 eV for electron concentrations varied from 1.49×10^{19} to 3.54×10^{18} cm^{-3}. The ~100 meV shift from the highest to lowest electron concentration is likely due to the Moss-Burstein effect [134]. The smallest electron concentration samples' PL peak location approaches the fundamental bandgap. Thus, plasma optimization is essential for InN films, as observed both electrically and optically.

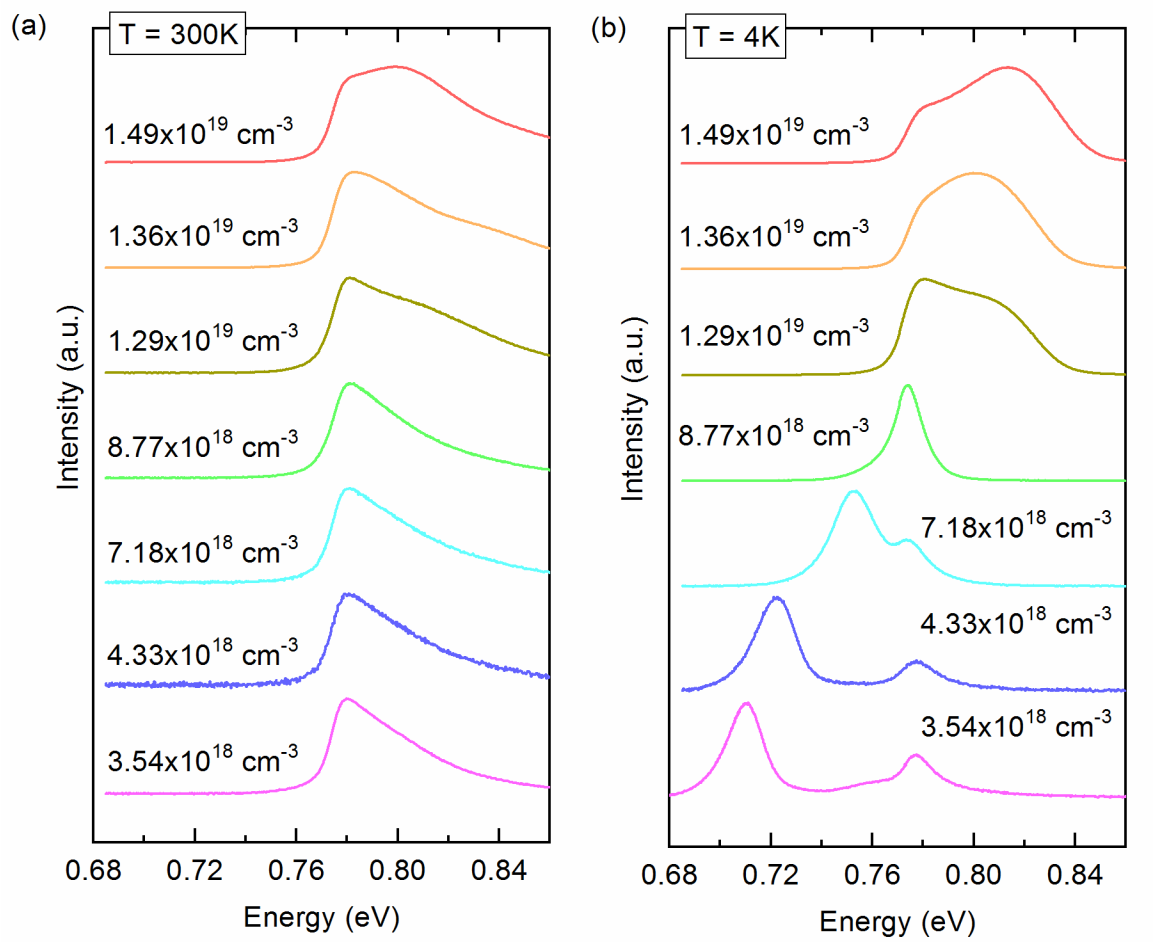

Figure 2.16. Photoluminescence spectra for ~1 µm thick InN films grown under various plasma conditions at 4 K.

In order to minimize the plasma damage in high In content films, one must minimize the atomic nitrogen species per unit thickness (or growth rate) and minimize the ion acceleration potential. Ptak *et al.* demonstrated that the molecular nitrogen species are the species that control the growth rate and the atomic nitrogen species were speculated to generate point defects in the crystal [35]. Thus, one should maximize the molecular to atomic nitrogen ratio and also minimize the ion acceleration potential in the plasma to minimize the plasma damage per unit thickness. Ptak *et al.* showed that the size of the holes in the aperture plate could be used to adjust the atomic to molecular species but did not

show the effect on the acceleration potential.

By plotting the OES molecular to atomic peak intensity ratio, one can determine the plasma condition necessary to maximize the molecular to atomic content and, thus, minimize the plasma damage. Figure 2.17 illustrates that at high flow and low power, the maximum ratio of molecular to atomic nitrogen is achieved, in agreement with the experimental results. This condition also results in the lowest floating potential and consequently the lowest acceleration potential as evident in Figure 2.9(b). Thus, minimizing the plasma damage for III-nitride films is achievable at low RF power and high nitrogen flow, while still maintaining smooth morphology.

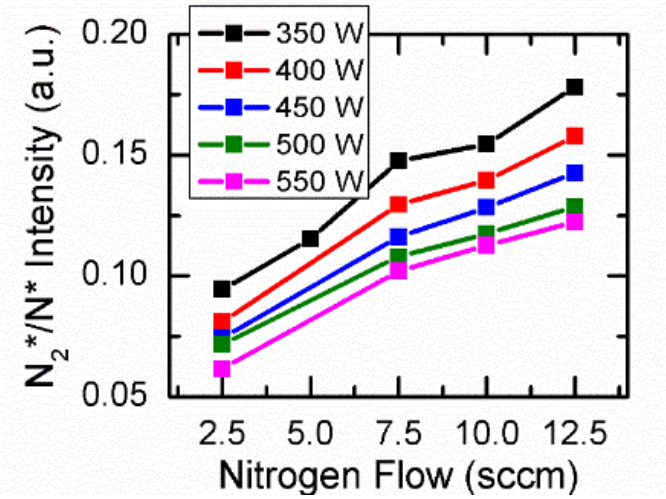

Figure 2.17. OES molecular to atomic peak intensity ratio for various plasma nitrogen flow rates and applied RF power.

2.4 Conclusions

Plasma-induced damage has been observed in III-nitride films and has been isolated from other effects such as roughening from low adatom mobility, InN decomposition, and indium desorption. By utilizing a flux gauge as a Langmuir probe in combination with OES, the RF plasma in the PAMBE reactor can be characterized. It is determined that atomic nitrogen and a plasma induced acceleration potential result in damage to InN films as observed via an elevated background electron concentrations. A low RF applied power and a high nitrogen flow enable a high molecular to atomic nitrogen ratio as well as a high growth rate and minimal acceleration potential which is the optimal plasma condition for continuous growth of high indium content III-nitrides, necessary for future III-nitride optoelectronics.

CHAPTER 3: EXTREME N-TYPE AND P-TYPE DOPING OF GaN VIA METAL MODULATED EPITAXY

3.1 Introduction

Metal modulated epitaxy (MME) is a growth technique in an MBE chamber that involves shuttering group-III metal sources and dopants, while constantly exposing the substrate to a nitrogen plasma. The growth rate is not reduced due to the shuttering in MME, unlike some other shuttered growth techniques that also modulate the nitrogen flux. In this work, Ga is used as the group III metal to form GaN via MME, while the dopant elements are Si and Ge for n-type doping, and Mg for p-type doping. MME of GaN is a physical growth technique which can enable extremely high impurity and thus doping concentrations, as well as precise control of the surface mobility of adatoms and surface chemistry.

3.2 Results and Discussion

3.2.1 MME Shuttering and Morphology of Si- and Ge-Doped N-type GaN

N-type doping of GaN is achieved via MME growth with added Si or Ge. Both Si and Ge are n-type dopants in wurtzite GaN, with activation energies of 22 and 31 meV, respectively [135]. Si is the most commonly used n-type dopant, but excessive Si doping can lead to edge-type threading dislocation propagation that adds tensile stress and eventual

cracking [136]. It has been demonstrated that Ge is more suitable for extreme doping of GaN, since both Ge and Si sit on Ga crystal sites, but Ge is closer in size to Ga and thus does not generate as much stress or the cracking that is observed in Si doping at similar doping concentrations [137]. Although Ge and Si both work as effective n-type dopants occupying Ga sites in GaN, the two dopants are more different when doping $Al_xGa_{1-x}N$ films. Bogusławski *et al*. calculated that the highest x for which the dopants are energetically favorable is 0.3 for Ge and 0.6 for Si. Therefore, for device structures that require n-type doping of high Al content AlGaN layers, Si is the chosen dopant.

In this work, extreme n-type doping of GaN is achieved for both Ge and Si. The MME shuttering scheme is plotted in Figure 3.1. The nitrogen flux from the plasma is kept constant and exposed to the growth substrate at all times which allows for continual GaN growth. Both the Ga and the n-type dopant cells are shuttered open and closed for 10 sec each resulting in 20 sec MME cycles. The III/V ratio is typically 1.8, and thus results in a metal-rich growth.

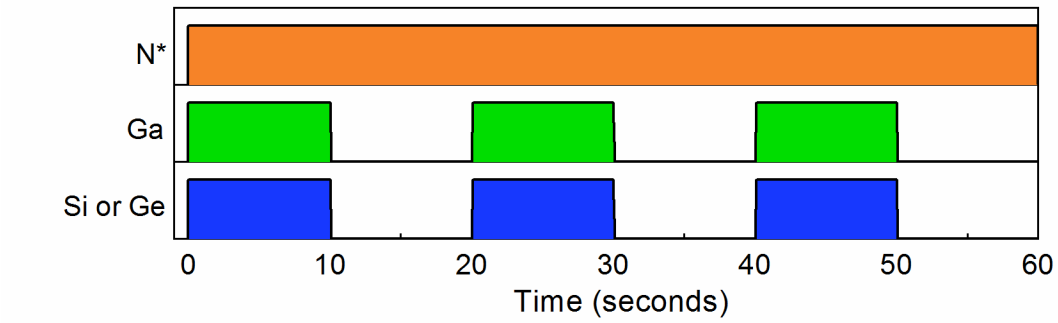

Figure 3.1. MME shuttering scheme for n-type GaN. The nitrogen flux from the plasma is kept constant, while the Ga and Si or Ge are shuttered open or close every 10 s.

The MME cycle can be tracked *in-situ* via reflection high energy electron diffraction (RHEED) intensity transients. An example RHEED intensity transient for an n-type GaN film is shown in Figure 3.2, where the green highlighted region represents the period of time that the Ga and Si shutters are open, while the white region represents the time they are closed. When the metal shutters are opened, the RHEED intensity decreases due to the electron beam scattering off the excess metal on the surface. In this example, at ~18 s the slope of the intensity transient decreases, which indicates that metal droplets are forming on the surface [138]. Once the metal shutters are closed, the nitrogen consumes the excess metal on the surface until the intensity flattens out and reaches the value it was before the metals were initially opened, and then the sequence is repeated.

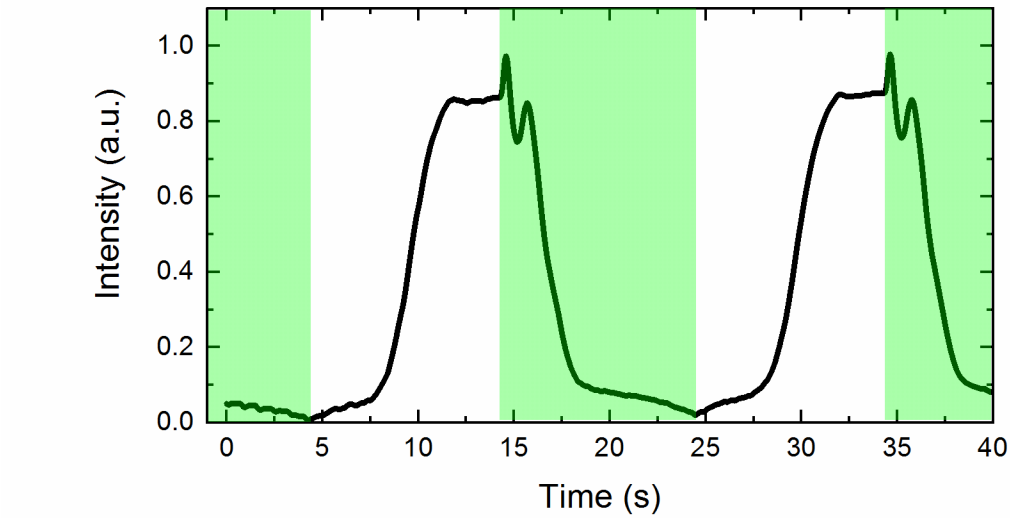

Figure 3.2. RHEED intensity transient for an MME-grown n-type GaN film with 10 s metal shutter open (green) and close (white) times.

The n-type MME condition involves large metal doses as a result of a high III/V ratio of 1.8 and a long metal shutter open time of 10 s. The large metal dose promotes high adatom mobility and results in smooth two-dimensional step-flow growth of the GaN crystal, even at low growth substrate temperatures. An example 1x1 μm^2 AFM scan of an n-type GaN film is shown in Figure 3.3. The AFM scan shows the smooth step-flow growth mode, which results in a ~0.2 nm RMS roughness or approximately the roughness limited by single atomic steps. The inset RHEED image shows a streaky pattern, with a 2x reconstruction that indicates a smooth Ga-polar surface [139].

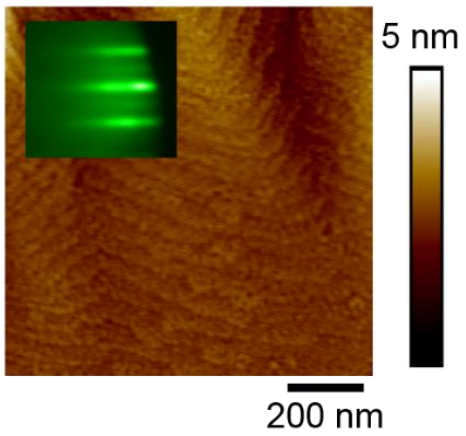

Figure 3.3. 1x1 μm^2 AFM of a representative n-type GaN film grown via MME demonstrating smooth step-flow growth. The RHEED inset exhibits a 2x reconstruction which further indicates a smooth Ga-polar surface.

3.2.2 MME Shuttering and Morphology of Mg-Doped P-type GaN

P-type doping GaN via MME is achieved with Mg doping. P-type doping is significantly more difficult in the III-nitrides for a variety of reasons. One major reason is

that the Mg activation energy is extremely high at ~170 meV above the valence band edge, and thus it is difficult to thermally activate acceptors efficiently at room temperature [140]. Additionally, GaN has a background doping level that is n-type and can be as high as 10^{16} – 10^{17} cm^{-3} range [141]. Thus, in order to measure hole concentrations in GaN, the background electron concentration must be first compensated and then overcome with more holes. Another challenge with p-type doping is that any hydrogen incorporated into the crystal can form a complex with Mg and reduce the overall hole concentrations, which is a major concern for the MOCVD technique, as well as the ammonia-based MBE approach [140]. Lastly, another large issue for p-type doping GaN with Mg is that N vacancies in the crystal can act as donors that compensate the intentional Mg doping and hole concentration [142]. This N vacancy issue is problematic because GaN is most commonly grown Ga-rich to promote smooth and high quality films, but excessively Ga-rich films can form high concentrations of compensating N vacancies. All of these concerns must be avoided to realize high hole concentration GaN films.

A high hole concentration MME shuttering sequence is utilized, where the metal-rich growth is precisely controlled to enable smooth surfaces, but limits the N vacancy concentration. The shuttering scheme is detailed in Figure 3.4, where the Ga and Mg cells are opened for 5 s and then closed for 10 s to form each 15 s cycle. The III/V ratio for these high hole concentration p-type GaN films is ~1.3.

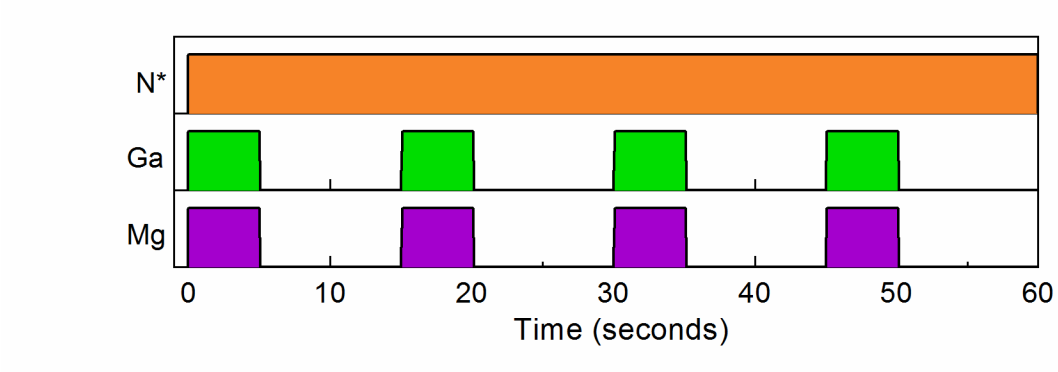

Figure 3.4 MME shuttering scheme for p-type GaN. The nitrogen flux from the plasma is kept constant, while the Ga and Mg are shuttered open for 5 s and closed for 10 s to form a 15 s cycle.

An example RHEED intensity transient for the growth of high hole concentration p-type GaN via MME is shown in Figure 3.5. The green highlighted region indicates when the Ga and Mg shutters are open. Similar to the n-type results, when the metal shutters are opened, the RHEED intensity decreases from scattering, and then rises back to the initial value when the excess metal is consumed to reach a dry, or metal-free surface. Unlike the n-type transient in Figure 3.2, the p-type intensity transient in Figure 3.5 does not change slope significantly during the metal shutter open time (highlighted in green) and thus Ga metal droplets are not accumulating. Preventing Ga droplets is key to achieving high hole concentrations in GaN.

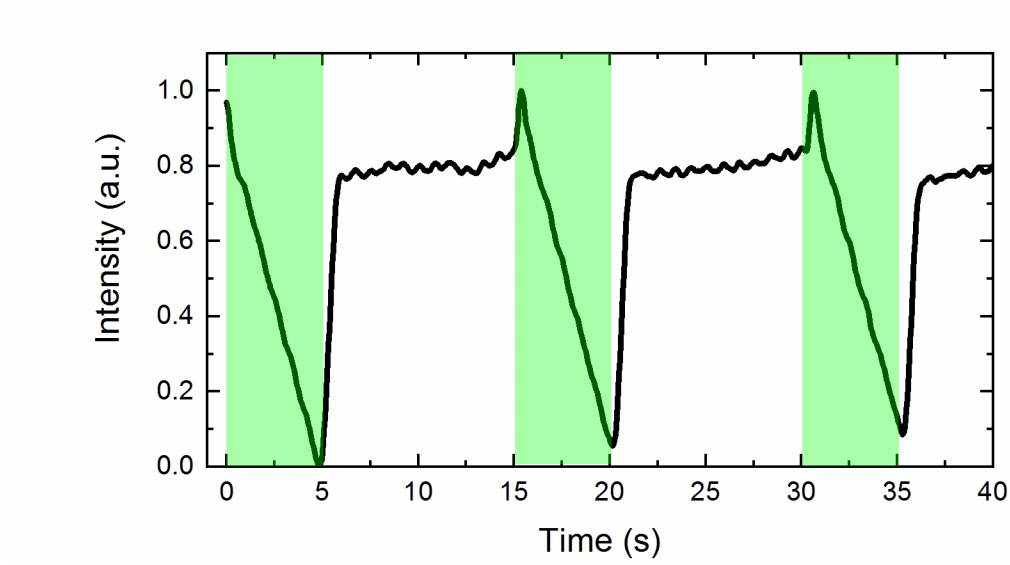

Figure 3.5. RHEED intensity transient for an MME-grown p-type GaN film with 5 s metal shutter open (green) and 10 s close (white) times.

The p-type films grown under these conditions have less adatom mobility when compared to the more metal rich n-type condition. The reduced metal-richness and lack of Ga droplets on the surface results in a worse morphology of p-type GaN. An example 1x1 μm^2 AFM scan of a p-type GaN film is shown in Figure 3.6 with a RHEED pattern inset. The image indicates texturing of the film in this condition, and results in a ~1-2 nm RMS roughness still comparable with state of the art MBE and MOCVD p-type films.

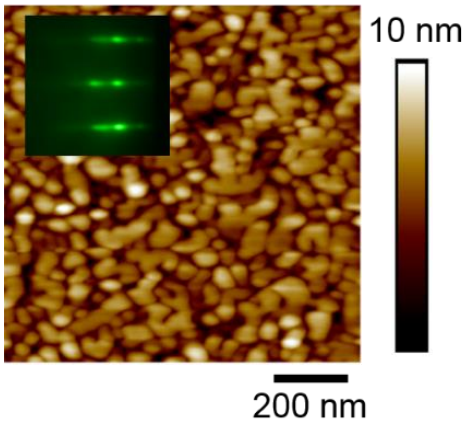

Figure 3.6. 1x1 μm^2 AFM (RHEED inset) of a representative p-type GaN film grown via MME demonstrating a textured surface.

3.2.3 Secondary Ion Mass Spectrometry Calibration of Mg and Si Dopants

Secondary ion mass spectrometry (SIMS) measurements were taken to calibrate the cell temperatures and flux of the Si and Mg dopant cells in the MBE system with specific MME shuttering schemes and a N-limited growth rate ~ 1µm/hr. A single calibration sample was grown and is detailed in Figure 3.7. The structure is shown in Figure 3.7(a), where alternating layers of Mg-doped and Si-doped layers are grown to calibrate dopant incorporation at various dopant cell temperatures. The SIMS measurement data is shown in Figure 3.7(b), with sharp near step-like profiles for Mg and Si layers. Al markers are utilized to mark the interfaces between the Si-doped and Mg-doped layers, with the Al counts corresponding to the right y-axis. Interestingly, the highest Mg-doped layer went through a transition during the growth, possibly indicating Mg-precipitates were formed and the solubility limit of ~7.7 x 10^{20} cm^{-3} was reached with this technique, which is higher than previously reported [143], [144].

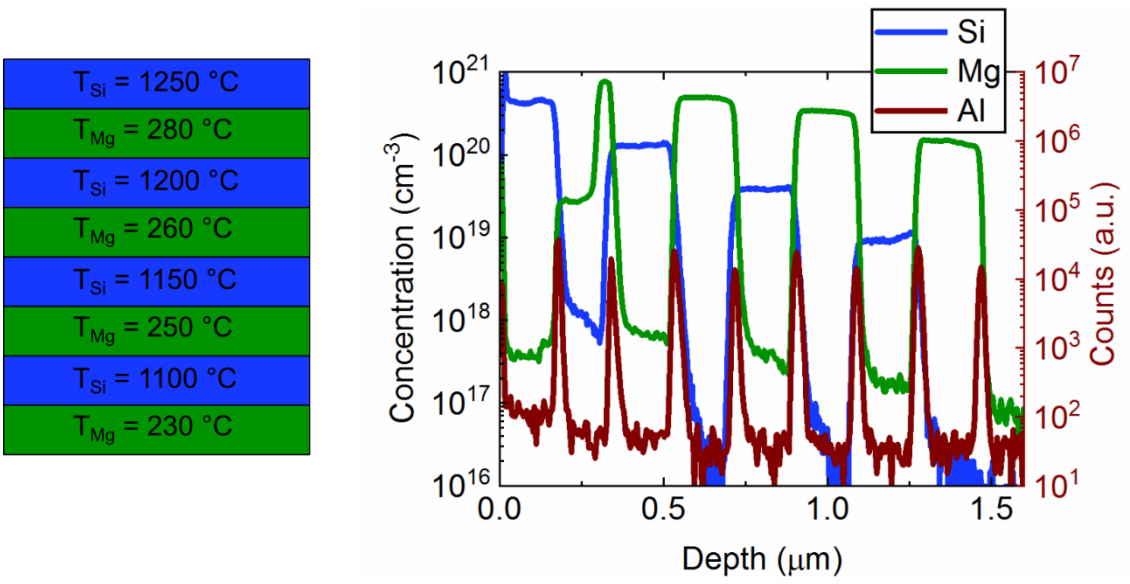

Figure 3.7. SIMS Mg-doped and Si-doped GaN calibration sample (left) structure and (right) measurement results to determine dopant incorporation for specific MME conditions and growth rates.

3.2.4 Electrical Results for Extreme Si Doping of GaN

MME-grown GaN films are doped with Si at various concentrations determined from the SIMS results. The resistivity and electron concentration at several Si concentrations is shown in Figure 3.8. At a Si concentration of 4.6 x 10^{20} cm^{-3}, the electron concentration reaches a maximum of 3.1 x 10^{20} cm^{-3}, and a low resistivity of 2.7 x 10^{-4} Ω-cm. This activation ratio is ~ 2/3 which deviates somewhat form the theoretical values expected from degenerate Fermi-Dirac statistics for single donor states using a spin degeneracy factor of 2 as is normally assumed. The reasons for this deviation is likely due to impurity band formation and thus a deviation at high doping from the single donor state model validity. These results are promising for III-nitride devices, e.g. to reduce contact resistances, and form tunnel junctions.

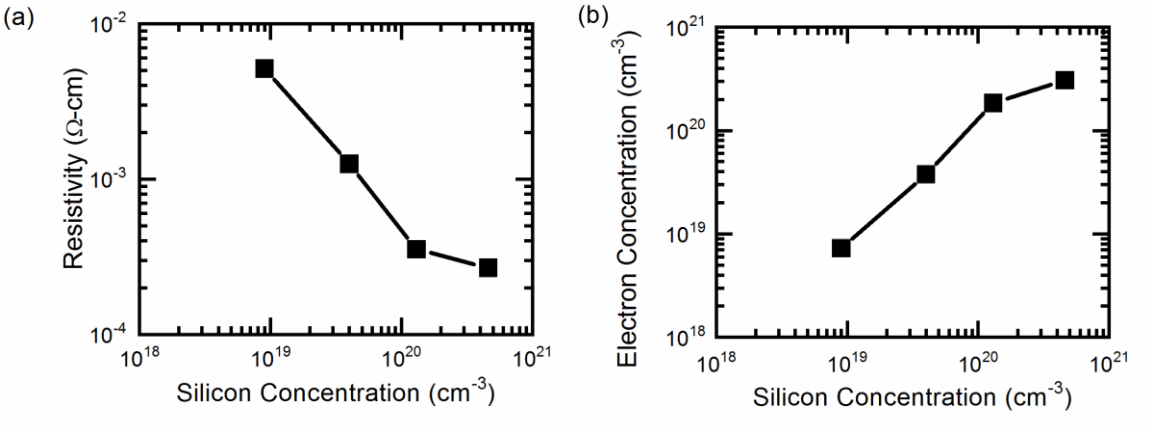

Figure 3.8. Si-doped MME GaN films (a) Van der Pauw resistivity, and (b) Hall-effect electron concentration.

When comparing to the literature, the heavily doped MME-grown films in this work have some of the lowest reported resistivities for Si-doped GaN. Figure 3.9 compares the resistivities in this work with values found in the literature. Additionally, given that these data fall on the same trend line for various growth techniques including MOCVD, it indicates that MBE can produce state of the art material at least within the highly doped regime where impurity scattering dominates conduction.

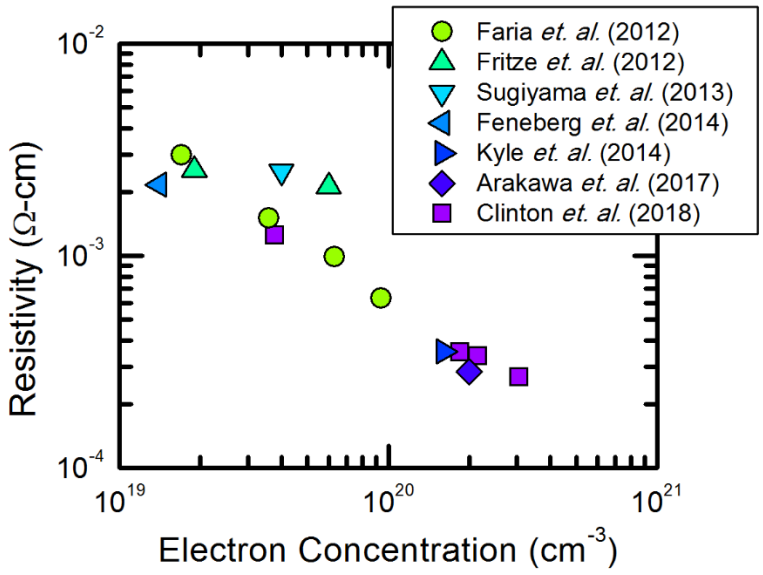

Figure 3.9. Resistivity of Si-doped GaN in this work compared to others in the literature.

3.2.5 Photoluminescence Spectra of Heavily Si- and Ge-Doped GaN

As previously discussed at the beginning of this chapter, Ge and Si are both common n-type dopants in GaN, while Si doping is more capable for higher Al content AlGaN films. In order to compare the extreme n-type doping capabilities of Ge and Si for GaN, a variety of films are grown with either Si or Ge doping and corresponding electron concentrations spanning from ~2-3 x 10^{17} cm^{-3} to ~2-3 x 10^{20} cm^{-3}. Photoluminescence spectra are taken and shown in Figure 3.10 to demonstrate how both Si and Ge are capable of degenerately n-type doping GaN via the MME technique.

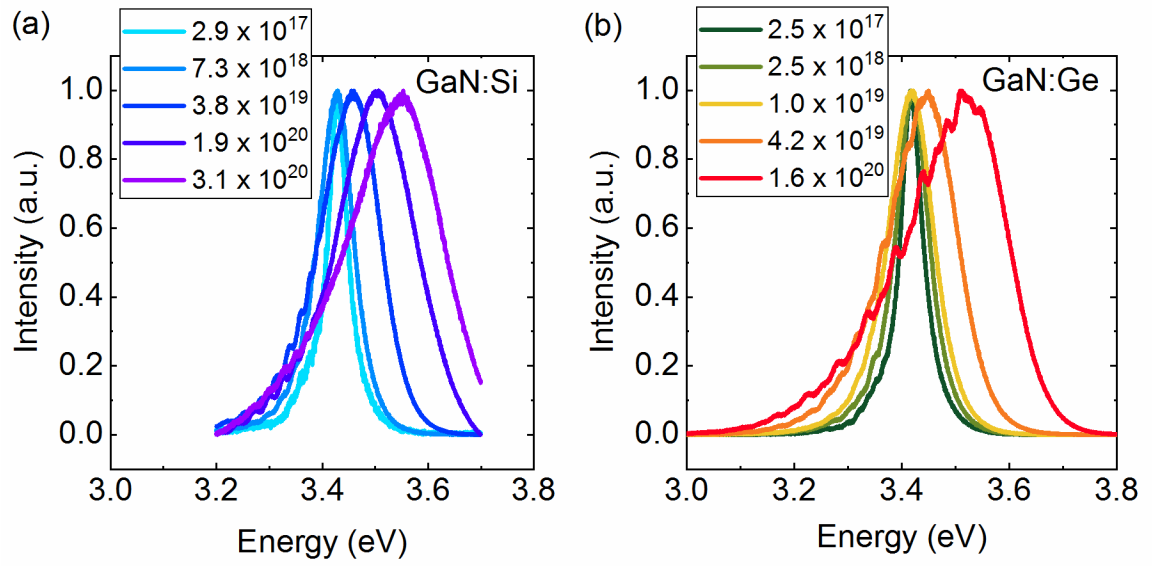

Figure 3.10. Photoluminescence spectra of n-type GaN films with various electron concentrations resulting from doping with (a) Si and (b) Ge.

The photoluminescence spectras in Figure 3.10 show similar trends for extreme doping. For both dopants, when increasing the doping from ~2-3 x 10^{17} cm^{-3} to ~1 x 10^{19} cm^{-3}, the peaks begin to broaden but remain at the same peak energy position. When further increasing the doping above ~1 x 10^{19} cm^{-3} the peak position shifts to higher energies, and the spectra begin to more significantly broaden. This shift in the peak energy position and broadening is due to the Moss-Burstein effect, as well as bandgap renormalization [145]. The Ge and Si peak energy positions from the photoluminescence spectra at each electron concentration are plotted in Figure 3.11. The highest doped film results in a ~0.12 eV peak emission energy than the lowest doped film. The slightly higher peak position for the lighter doped Si samples is likely due to Si being ~9 meV closer to the conduction band edge than Ge.

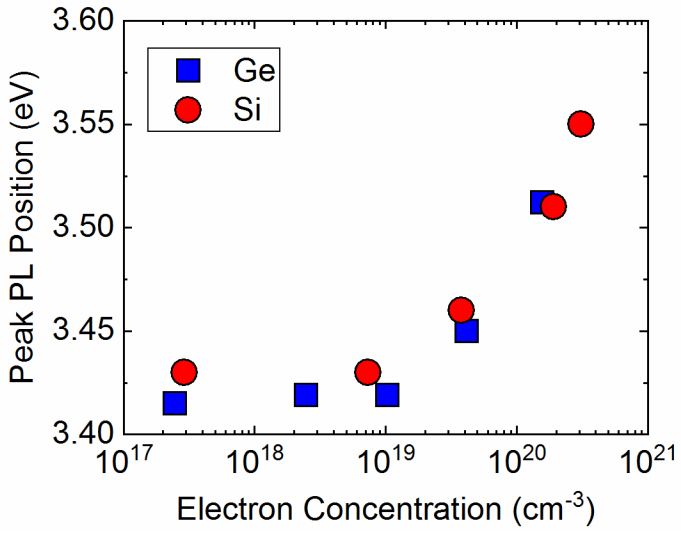

Figure 3.11. Ge and Si peak photoluminescence energy positions at various electron concentrations indicating degenerate doping and a Moss-Burstein shift is achieved with both dopants.

The extreme n-type doping presented here can be used for traditional applications such as improving contact resistance, as well as for tunnel junctions which will be explored later, but also in epitaxial distributed Bragg reflectors (DBRs). A DBR is a multi-layer reflector where changes in the index of refraction at each interface result in partial reflection of any incident light. If the DBR layers are engineered in a particular way so that the reflected light from each interface constructively interferes with other reflections, then the stack can act as a high reflectivity mirror. DBRs are especially useful in optoelectronic devices such as LEDs by aiding in the light extraction, and in lasers to help promote the necessary optical confinement for lasing. Most optoelectronic DBRs are dielectric DBRs that are placed on a device during fabrication. Lasers often require complicated flip-chip bonding in order to incorporate bottom and top dielectric DBR. Epitaxial DBRs may provide an alternative to the complicated fabrication process for devices that require two

dielectric DBRs.

Extremely n-type doped GaN results in a change in the refractive index, and thus an epitaxial DBR can be formed by simply alternating doping concentrations [146]. The refractive indices at different wavelengths of two films with electron concentrations of 2 x 10^{18} cm^{-3} and 2 x 10^{20} cm^{-3} are shown in Figure 3.12(a). The inset in Figure 3.12(a) is the difference between the two refractive indices at each wavelength, and shows the lowest difference of about 6% at 450 nm and the highest difference of about 14% at 370 nm, which was the lowest wavelength measured. The calculated ideal reflectivity is displayed in Figure 3.12(b) for 10, 20, 40 and 80 pair quarter-wavelength DBR stacks at center wavelengths of 383, 451, and 650 nm. The peak reflectivity for the 383, 451, and 650 nm reflectors with 80 pairs is 99.5, 97.2, and 98.9%, respectively. The 451 nm reflector is the least reflective because the two doped layers have the lowest difference in refractive index at that wavelength.

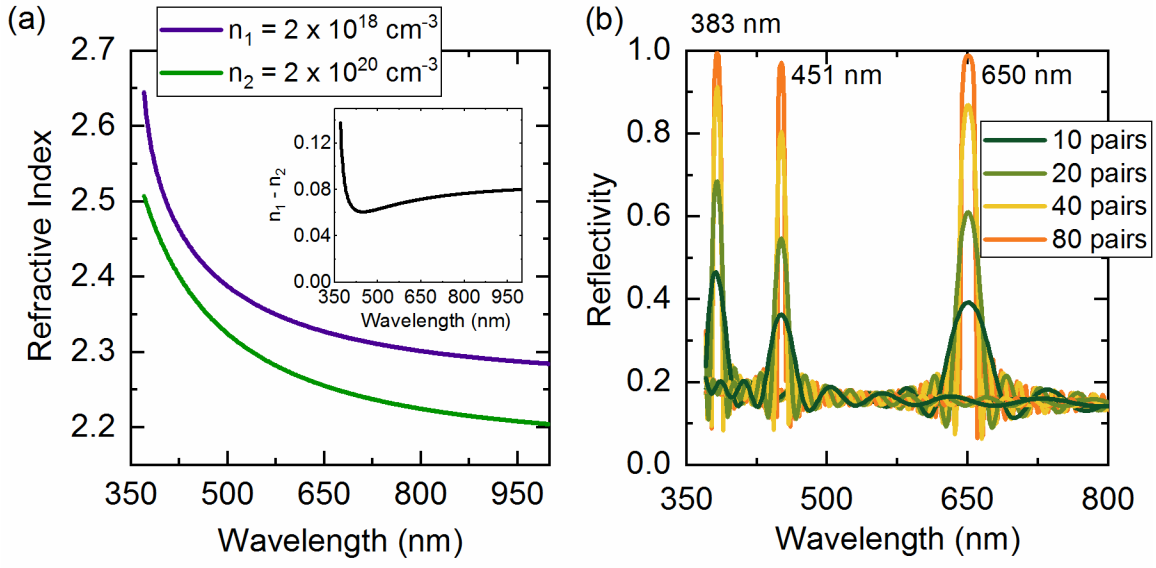

Figure 3.12. (a) Refractive index measurements (inset: difference) for a lightly and degenerately n-type doped GaN film and (b) Calculated reflectivity for DBRs with

different numbers of pairs and center wavelengths.

Epitaxial n-type GaN DBRs can thus be engineered to reflect light at a variety of wavelengths, as long as the change in doping is enough to get a large change in the refractive index that leads to a high reflectivity. The main drawback to this technique is that these DBRs require many pairs to reach > 90% reflectivity, and thus thick reflecting layers that add cost to the overall device. Therefore, they may be best utilized in tandem with a dielectric DBR or metal mirror.

Others have investigated further improving the DBRs reflectivity by selectively electro-chemically etching the heavily doped layers to make them porous and a lower refractive index [147], [148]. This approach has been successfully demonstrated, but does increase the vertical resistivity of the stack if the design involves injecting carriers through the DBR [148].

The epitaxial DBR presented here is conductive to allow for carrier injection through the DBR stack. Since the DBR involves a degenerately n-type layer, it is also inherently compatible with tunnel junctions and alternative emitter designs such as a laser with two n-type DBRs on either side of the active area where one DBR is tunnel injecting into the p-type layer. Epitaxial DBRs are therefore exciting for alternative LED and laser designs as the main reflector, or possibly in tandem with other traditional reflectors.

3.2.6 Electrical Results for Extreme Mg Doping of GaN

Four 100 nm thick Mg-doped MME p-type GaN films are grown resulting in a wide range of hole concentrations from 7.1 x 10^{17} cm^{-3} to 2.7 x 10^{19} cm^{-3} at room temperature.

The resistivity of these films is measured at temperatures from 90 to 350 K, and is shown in Figure 3.13. The room temperature resistivity spans from 7.3 to 0.9 Ω-cm for the lowest to highest hole concentrations.

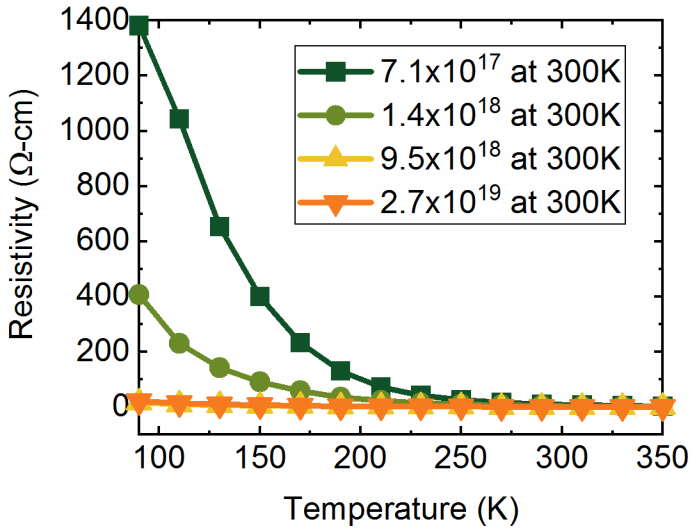

Figure 3.13. Temperature dependent resistivity measurements for various MME-grown p-type GaN films at low and high hole concentrations.

The temperature-dependent hole concentrations for the four p-type GaN films are measured, and are shown in Figure 3.14(a). As the temperature is reduced, the carrier freezeout is most significant for the lightest doped sample, reducing the hole concentration from 1.7 x 10^{18} cm^{-3} at 350 K down to 5.7 x 10^{16} cm^{-3} at 170 K. The effective activation energy of Mg in each film can be extracted from the slope of the traces in Figure 3.14(a), where a steeper slope corresponds to a higher effective activation energy. The activation energies for the four samples are plotted in Figure 3.14(b) at their corresponding hole concentrations. Notably, the effective activation energy decreases from a value of 149 meV for the film with a hole concentration of 7.1 x 10^{17} cm^{-3}, which is close to the literature

value of 170 meV for lighter doped p-type GaN, to 16 meV for the film with a hole concentration of 2.7 x 10^{19} cm^{-3}. The small effective activation energy and minimal carrier freezeout are indicators that an impurity band is formed in the heavily doped samples, and not a single acceptor energy level. These results are promising and indicate that with the MME growth technique, the effective activation energy can be significantly lowered, enabling extremely high hole concentrations and high activation efficiencies.

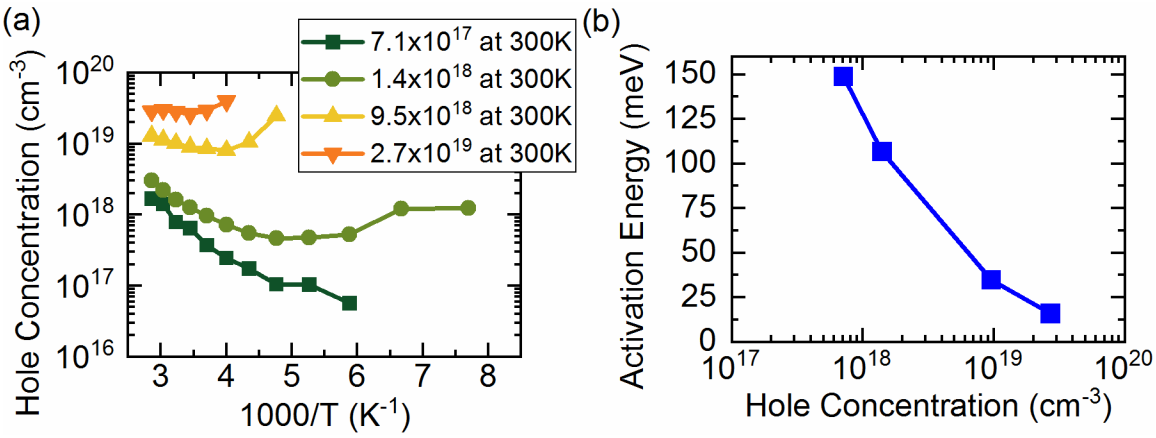

Figure 3.14. MME grown p-type GaN films' (a) temperature-dependent hole concentrations and (b) their corresponding activation energies

Next, more heavily doped MME p-type GaN films are grown with Mg concentrations from 1.5 x 10^{20} cm^{-3} to 5.3 x 10^{20} cm^{-3} at the optimal MME shuttering condition detailed previously in this chapter. The Mg concentration is determined from the SIMs results. The Van der Pauw resistivity of these films is first measured and displayed in Figure 3.15(a). The resistivity curve for Mg-doped GaN typically has this shape. The resistivity decreases as expected with additional Mg doping due to the inverse relationship with resistivity and carrier concentration and reaches a minimum value of 0.109 Ω-cm for a Mg concentration of 3.5 x 10^{20} cm^{-3}, but increases to 0.118 Ω-cm at an extreme Mg

concentration of 5.3 x 10^{20} cm^{-3}. The increase in resistivity is due to self-compensation from Mg-related defects, such as prismatic inclusions acting as donors and compensating the hole concentration [79], [81]. The hole concentrations for these films are shown in Figure 3.15(b). Similar to the resistivity curve, for these growth conditions the hole concentration reaches an optimal maximum value of 1.5 x 10^{20} cm^{-3} before the extreme doping generates compensating defects which lower the hole concentration.

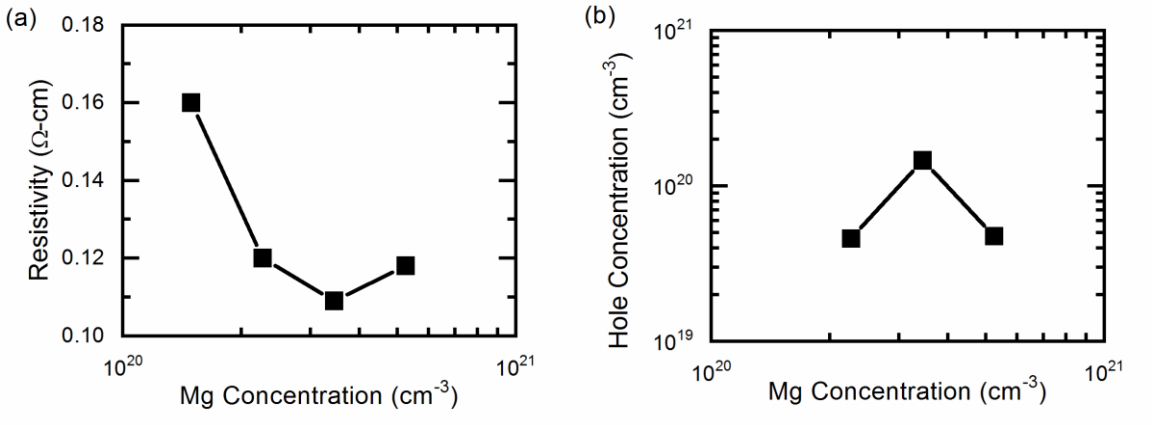

Figure 3.15. Mg-Doped MME-grown GaN films' (a) Van der Pauw resistivity and (b) Hall-effect hole concentration.

The resistivities of the MME-doped p-type GaN films presented here are some of the lowest values reported in the literature due to these films having the highest hole concentrations in literature. The resistivity values in this work are compared to the literature and are shown in Figure 3.16.

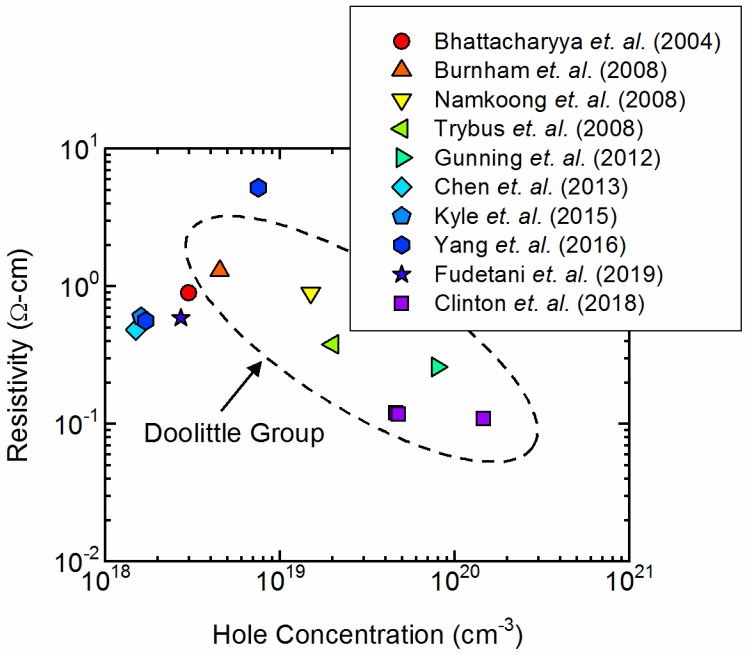

Figure 3.16. Resistivity values of heavily Mg-doped p-type GaN via MME in this work compared to others.

3.3 Conclusions

In this chapter, MME shuttering conditions are established to enable extreme doping of GaN without significantly degrading the GaN surface morphology. The dopant incorporation using these MME conditions is calibrated for Si and Mg via SIMS. Extreme electron concentrations are achieved with Si or Ge. The degenerately doped n-type GaN films show a Moss-Burstein shift in photoluminescence spectra, and are show promise for applications such as epitaxial DBRs. Additionally, for Mg-doped p-type GaN, low resistivities and high hole concentrations are achieved with the MME technique. The ability

to achieve such elevated carrier concentrations is a unique advantage of MME, and is critical towards forming tunnel junctions in the next chapter.

CHAPTER 4: NEGATIVE DIFFERENTIAL RESISTANCE IN GaN HOMOJUNCTION TUNNEL DIODES AND LOW VOLTAGE LOSS TUNNEL CONTACTS

4.1 Introduction

Tunnel junctions (TJs) have been investigated since Esaki discovered the negative differential resistance (NDR) phenomenon in a heavily doped germanium pn junction in forward bias [95]. After Esaki's initial discovery, TJs have since become essential for devices such as high frequency oscillators [96] and amplifiers [97], multi-junction solar cells [98], laser diodes [99], and light emitting diodes (LEDs) [100].

An Esaki TJ is a heavily doped p++/n++ junction with a sufficiently narrow depletion width that allows electrons to tunnel between conduction and valence bands in reverse bias as well as low forward bias. In the non-degenerate limit, a simple analytical expression for the depletion width of a p/n junction at zero bias may identified

$$w = \sqrt{\frac{2\varepsilon}{q}\frac{N_A+N_D}{N_A N_D}\left[\frac{kT}{q} ln\left(\frac{N_A N_D}{n_i^2}\right)\right]}, \quad (1)$$

from which some qualitative insight may be gained for the degenerate case considered here. The symbol ϵ is the free-space permittivity, k is Boltzmann's constant, q is the electron charge, n_i is the intrinsic carrier concentration, and N_A and N_D are the acceptor and donor concentrations, respectively. To decrease the depletion width and consequently enhance the tunneling probability, one can increase the donor and acceptor concentrations and/or

reduce the built-in voltage. However, as the bandgap of the material increases, so does the built-in junction voltage, and achieving high acceptor and donor concentrations becomes more challenging due to increased dopant ionization energies. Both these factors conspire to increase the depletion width and reduce the tunneling probability under bias. Therefore, forming homojunction Esaki-style TJs in wide bandgap semiconductors such as gallium nitride (GaN) with a bandgap of 3.4 eV poses a challenge. Furthermore, the current-voltage characteristics of GaN diodes and LEDs are often associated with trap-assisted tunneling (TAT), and not just traditional thermionic emission [149]. TAT is further evidenced by ideality factors in excess of 2 [150]. TAT offers an additional non-Esaki mechanism for which tunneling can occur for heavily doped p++/n++ junctions.

Tunnel junctions for III-nitride devices such as LEDs are mainly demonstrated as n-type tunnel contacts to resistive p-type layers [104]–[107]. N-type tunnel contacts to p-type layers can improve current spreading, avoid high p-type contact and sheet resistances, and eliminate at least one device fabrication step. In addition to TJs implemented as tunnel contacts, Grundmann *et al*. demonstrated a III-nitride series-connected LED with an InGaN interlayer TJ [100], and Kurokawa *et al*. demonstrated a series-connected solar cell with an InGaN interlayer TJ [109]. III-N laser diodes incorporating tunnel junctions for hole injection have also been demonstrated [151] to both reduce the contact resistance and to reduce the loss associated with optical absorption [152]. Furthermore, Hamamatsu has used a tunnel junction to connect two laser diodes stacked one on top of another [108]. Although various devices incorporating TJs have been fabricated, further efforts to minimize III-nitride TJ resistance in both forward and reverse bias is necessary to improve design freedom and device performance.

GaN homojunction-tunnel diodes are particularly difficult to realize due to the high activation energy of magnesium doping with conventional growth techniques, preventing the sufficient hole concentrations at the junction [153]. Thus, polarization engineered TJs using p-GaN/AlN/n-GaN and p-GaN/InGaN/n-GaN heterojunction structures were used to facilitate tunneling by engineering the valence and conduction bands, and by reducing the effective tunneling distance for carriers [101]–[103]. Nevertheless, for certain device applications inserting a heteroepitaxial interlayer can introduce additional defects and cause undesirable photon absorption and reduction in light extraction efficiency. Thus, GaN homojunction tunnel diodes are preferred for many III-nitride optoelectronic devices.

Metal-organic chemical vapor deposition (MOCVD) is the growth technique for most commercially grown III-nitride devices. But GaN homojunction tunnel diodes are difficult to grow via MOCVD because of the difficulty in obtaining abrupt and sharp p/n junctions due to the Mg memory effect [154], [155], low p-type doping activation efficiency, and the annealing requirement to activate p-type doping [77].

The magnesium memory effect is when remnant magnesium in an MOCVD reactor unintentionally incorporates into the subsequent grown layers, which makes achieving GaN homojunction TJs difficult [154], [155]. Hwang *et al*. demonstrated that a GaN tunnel contact can be formed entirely via MOCVD by growing the structure up to the p-type TJ interface, removing it for a cleaning treatment, and then finally reloading the wafer into the reactor to complete the structure [156].

MOCVD grown Mg-doped GaN typically requires an activation anneal and is limited to electrically active hole concentrations in the low 10^{18} cm^{-3} range [77]. Hydrogen will diffuse out of the film by annealing or otherwise cause n-type compensating defects.

In a TJ device with a buried p-type layer, the activation anneal becomes significantly more problematic as the hydrogen no longer easily diffuses vertically through the n-type layers above the p-type layer [157], but instead diffuses laterally out through the sidewalls [156]. MOCVD grown GaN tunnel-contacted LEDs with larger device areas have reduced current densities and, thus, reduced light output, likely from insufficient hydrogen out-diffusion.[156] Therefore, the necessary lateral hydrogen diffusion out of buried p-type layers for a single-reactor MOCVD grown TJ limits device area required for LEDs and solar cells.

The metal modulated epitaxy (MME) growth technique performed in a molecular beam epitaxy (MBE) reactor enables high carrier concentrations while also achieving an abrupt doping profile necessary to realize a GaN homojunction tunnel diode [158]. Hole concentrations above $7\text{x}10^{19}$ cm^{-3} have been achieved with the MME growth technique without an anneal [159]. When comparing typical maximum MOCVD (N_A^- ~$5\text{x}10^{18}$ cm^{-3}, N_D^+ ~$1\text{x}10^{20}$ cm^{-3}) and MME (N_A^- ~$8\text{x}10^{19}$ cm^{-3}, N_D^+ ~$5\text{x}10^{20}$ cm^{-3}) doping concentrations, and assuming an abrupt p++/n++ junction, the calculated depletion widths are ~27 and ~7 nm at zero bias, respectively, making the probability of tunneling insignificant for Esaki style tunneling under forward bias. A map of the depletion width for a GaN p/n homojunction is shown in Figure 4.1, highlighting the requirement for extreme n- and p-type doping to achieve the sub-10nm depletion width range. Notably, MOCVD p-type acceptor concentrations limit the depletion widths to > 30nm, even if the doping on the n-side of the junction is $3\text{x}10^{20}$ cm^{-3}.

Three defect-assisted mechanisms may enable tunneling for wide depletion widths: (1) if electrons tunnel first into intermediate states, such as defects, instead of directly into

the conduction band, tunneling becomes more likely. (2) Alternatively, as current flows through the junction, charge can accumulate at defects effectively acting as additional dopants, reducing the depletion width, and enhancing the tunneling probability. Note that this charge accumulation can be time dependent when current is flowing. (3) Furthermore, excessive doping can result in band gap narrowing which also improves the tunneling probability. While the devices analyzed below show strong evidence of at least (1) defect assisted tunneling and (2) charge trapping at defects as evidenced by current induced drifts in the I-V curves, significantly more characterization is needed to elucidate which combination of defect related enhancements are active in the present devices.

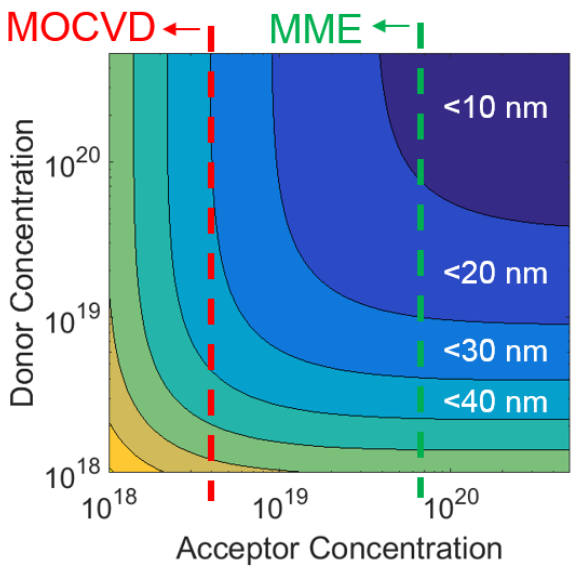

Figure 4.1. Depletion width map for GaN p/n homojunctions at various donor and acceptor concentrations. The acceptor concentration limitations are shown for both MOCVD and MME.

In addition to the heavy doping necessary for TJs, MME and traditional MBE are capable of growing high-quality and single-phase InGaN films throughout the miscibility

gap [49]–[52]. GaN homo-tunnel junctions in combination with single-phase InGaN films can enable improved III-nitride device design freedom.

In this work, we explore the current-voltage characteristics and effects of extreme doping via MME on p++/n++ junctions in order to minimize the depletion width and thus, tunneling distance for electrons. Additionally, it is found that defects appear to be a source of tunneling, not purely Esaki-style interband tunneling. Trapped charges at the defects seem to modify the tunnel characteristics. Afterward, we utilize tunnel junctions as tunnel-contacts for p/i/n diodes to improve device performance.

4.2 Experimental Procedure

All samples discussed here are grown in a Riber 32 plasma-assisted molecular beam epitaxy (PAMBE) reactor. Growths are initiated on Saint-Gobain Lumilog MOCVD-grown n-type c-plane GaN templates on sapphire.

Two types of structures are grown and fabricated into circular devices. Device structure A is a p++/n++ tunnel junction diode, while device structure B is an n++/p++/i/n tunnel-contacted pin diode. Both device structures are illustrated in Figure 4.2. The MME growth technique is utilized to grow the entirety of the two structures. Further details about the MME growth technique were discussed by Moseley *et al.* [138] and Gunning *et al.* [158].

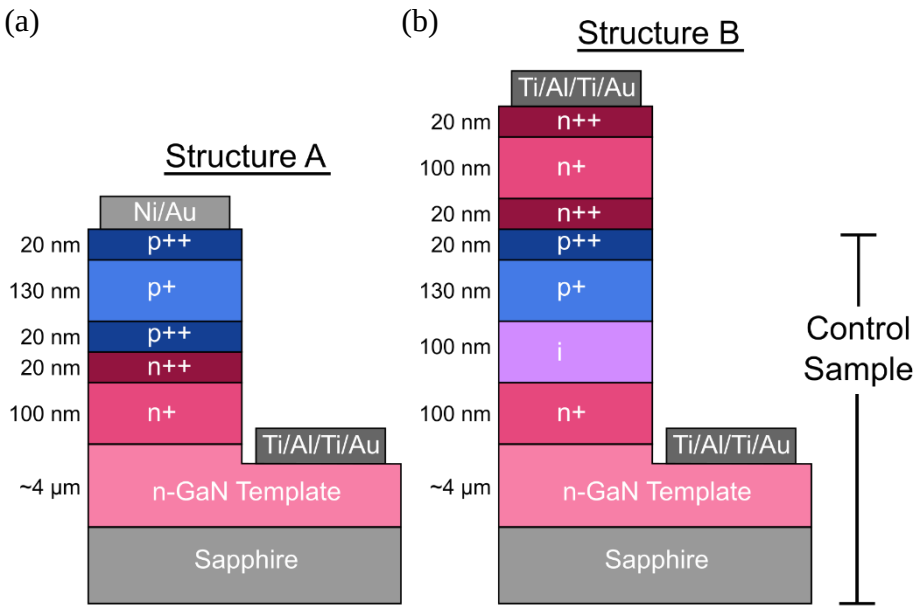

Figure 4.2. Device structures for (a) p++/n++ diode with a GaN homo-tunnel junction (sample A) and (b) n++/p++/i/n diode with a GaN homo-tunnel contact (sample B). Samples B1-B3 have a mesa top n-type contact metallization of Ti/Al/Ti/Au, while the control sample B4 has a mesa top p-type contact metallization of Ni/Au.

The approximate dopant concentrations based on doping calibrations for the TJs used in both structures are detailed in Table 4.1. Doping concentrations in the TJ for both A1-A3 and B1-B3 are matched. The magnesium concentration in the TJ is further increased for sample A4 when compared to sample A3 by growing a 3 nm heavily doped p-type layer at the TJ interface. Additionally, a p/i/n control sample (B4) was grown to compare to the tunnel contacted samples of structure B.

100 μm diameter circular mesas were defined with standard photolithography and an inductively coupled plasma (ICP) etching process with BCl_3 and Cl_2 gases used to electrically isolate individual cells. Metal stacks of Ti (300 Å)/Al (1000 Å)/Ti (300 Å)/Au (500 Å) and Ni (500 Å)/Au (500 Å) were deposited using e-beam evaporation as contacts to n-GaN and p-GaN, respectively. The tunnel-contacted devices (B1-B3) have a mesa top

n-type contact metallization, while the control sample B4 has a mesa top p-type contact metallization. The contacts were not annealed due to the extremely high doping levels used in this study. Both contacts showed ohmic behavior measured by circular transmission line measurement (CTLM) patterns, as demonstrated in our previous work [69].

Table 4.1. The approximate dopant concentrations at the TJ interface used in this study verified by secondary ion mass spectrometry (SIMS) at Evans Analytical Group. Sample B4 is the p/i/n control sample with no TJ contact.

Sample ID	TJ Silicon Concentration (cm^{-3})	TJ Magnesium Concentration (cm^{-3})
A1,B1	4.0×10^{19}	3.4×10^{20}
A2,B2	1.9×10^{20}	3.4×10^{20}
A3,B3	4.6×10^{20}	3.4×10^{20}
A4	4.6×10^{20}	7.7×10^{20}
B4	NA	NA

4.3 Results and Discussion

4.3.1 Current-Voltage Measurements of GaN Homojunction Tunnel Diodes

Tunnel junction diode current-voltage characteristics of samples A1-A4 are displayed in Figure 4.3. As the doping concentration increases at the TJ interface, conductivity in reverse and low forward biases increases. The higher current densities at low reverse bias compared to low forward bias indicate increased reverse bias tunneling. Additionally, sample A3 demonstrates tunneling in forward bias with the presence of NDR with a peak current density (PCD) at ~1.35 V. We have observed consistent and similar NDR results for all the tested devices on sample A3. The PCD of ~10.25 A/cm^2 at the onset of NDR and the valley current density of ~10.19 A/cm^2 resulted in a low peak-to-valley

current ratio (PVCR) of ~1.006, similar to the results reported by Akyol *et al.* [160]. on bulk GaN. No attempts were made to enhance the PVCR. Future refinements in the doping structures, primarily fine-tuning the doping at the TJ interface, are certainly proposed for improving the PVCR. In this study, the silicon concentration was varied over an order of magnitude from $4.0x10^{19}$ cm^{-3} in sample A1 to $4.6x10^{20}$ cm^{-3} in sample A3. Future devices with 10, 20, 30%, etc. lower and higher doping concentrations at the tunnel junction for both dopants may be one way to optimize the PVCR with sample A3 as a reference point.

The sample with the highest doping density (A4) exhibits a particularly high forward bias conductivity, and a near linear behavior up to ~200 A/cm^2, which is promising for multi-junction solar cells where the TJ is operated in forward bias. Sample A4 not exhibiting NDR is further evidence of a non-Esaki tunneling mechanism in forward bias. If the tunneling were of Esaki origin, the increase in doping would result in a higher NDR voltage and a larger PVCR. Contrarily, the magnesium doping at the interface, $7.7x10^{20}$ cm^{-3}, is ~67% higher in sample A4 than A3 and results in a dramatic >10X current increase. This along with the fact A3 and A4 already exceed the solubility of Mg in GaN [143] suggest the current increase results from more defect states for which to tunnel through. In trap assisted tunneling, the drop in current for NDR likely results from misalignment of the defect states with the majority band edges similar to a resonant tunneling diode. Thus, since there is >10x more current in A4 than A3, it is also likely there are many more defects broadening the defect tunneling band in A4 compared to A3, facilitating a wider range of voltages wherein conductive alignment occurs such that NDR disappears. It is worth considering that an equally plausible alternative explanation describing increased current and no NDR is simply metallic Mg precipitates pinning the fermi level near the

metallurgical junction, effectively shunting the junction. At present, insufficient data exists to provide a conclusion.

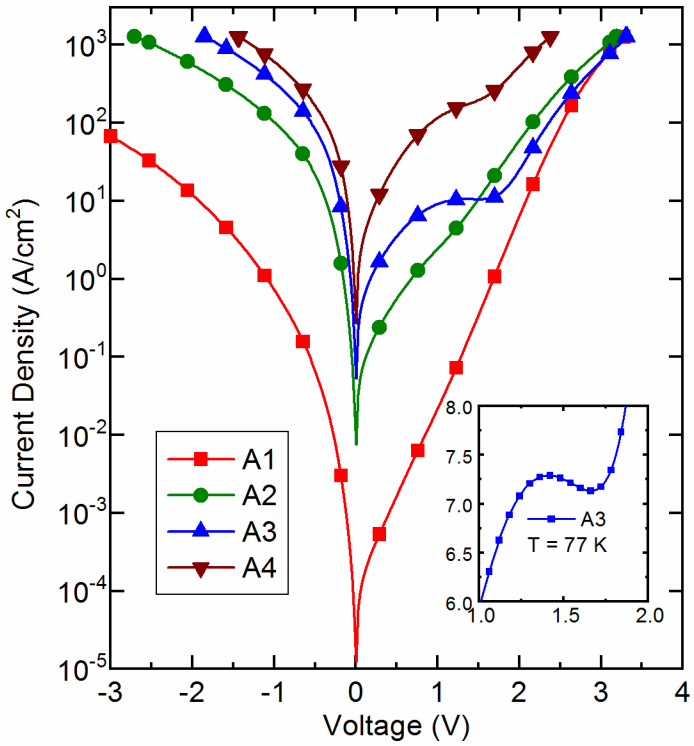

Figure 4.3. Semi-log current-voltage characteristics of 100 μm diameter circular mesa devices (samples A1-A4), with sample A3 demonstrating NDR at ~1.35 V. Inset: linear current-voltage characteristic for sample A3 at 77 K.

The inset in Figure 4.3 illustrates the current-voltage characteristic for the first scan of sample A3 at 77 K. The mechanism producing the NDR in forward bias is still active at 77 K. Low-temperature NDR confirms a tunneling mechanism, possibly defect-assisted tunneling, since the tunneling probability is not strongly temperature-dependent. Further temperature-dependent current-voltage analysis and additional characterization will be performed in a future work to elucidate the exact tunneling mechanism. Appreciable forward bias current at 77 K further substantiates previous evidence of reduced Mg

activation energy in heavily doped p-GaN due to impurity band conduction [158], [159].

4.3.2 Repeatability and Drift in the Negative Differential Resistance Region

The repeatability of the NDR feature in sample A3 was examined. Current-voltage traces of a representative device are shown in Figure 4.4. Each scan resulted in a higher current density in the valley of the NDR, regardless of sweep direction, until no NDR is observed, as shown in Figure 4.4(a). Outside the narrow NDR range, the current-voltage characteristics are nearly identical to sample A3 in Figure 2 for all scans. Figure 4.4(b) plots the current density at the valley of the NDR, which corresponds to a voltage of ~1.48 V. As the scan number increases, the valley current density increases roughly logarithmically. The NDR degradation trend is irreversible at room temperature, and by limiting the applied current or voltage, the number of scans demonstrating NDR can be extended. In addition, thermal annealing up to 400 ºC did not fully recover the NDR characteristic. Increased current density with each consecutive scan may indicate charge trapping at defects. Injected electrons may become trapped at neutral (un-ionized) magnesium acceptors and/or defects shrinking further the depletion width and consequently modulating conductance via increased tunneling probability. The repeatability of the current-voltage characteristics in reverse bias where the tunneling barrier is greatly reduced is likely due to Zener (band-to-band) tunneling becoming dominant. Presently, we speculate that the existence of forward bias tunneling implies at least the defect assisted tunneling mechanism (1) exists. Furthermore, in addition to mechanism (1) the metastable valley current in the forward bias NDR region suggests mechanism (2) which is trapping of charge at the defect-assisted tunneling sites.

Specifically, as current flows through the junction, time-dependent charge accumulates at defects and effectively acts as additional dopants, narrowing the depletion width, and enhancing the tunneling probability. A more extensive study of the doping concentrations at the TJ interface will be explored to study NDR degradation and permanence in a future work.

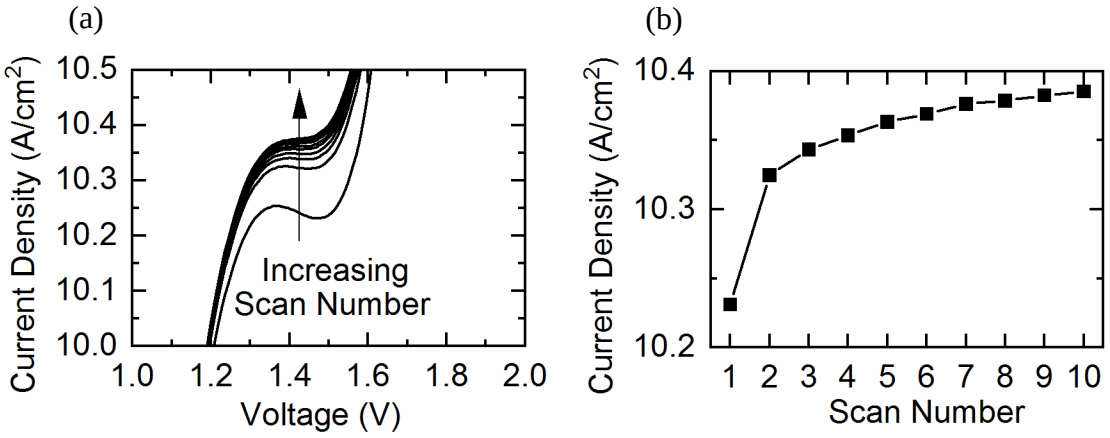

Figure 4.4. Current-voltage traces for sample A3 demonstrating (a) NDR degradation at room temperature, (b) valley current density increases logarithmically for each consecutive scan regardless of the sweep direction. Outside the narrow NDR range, the current-voltage characteristics are nearly identical to sample A3 in Figure 2 for all scans.

Others have reported similar NDR degradation after cycling the device, which might indicate a trap-assisted tunneling mechanism and not purely interband tunneling. Andrews *et al.* observed increased current density in the vicinity of the NDR region for GaAs tunnel diodes when the device was electrically cycled, or exposed to light of an appropriate wavelength [161]. They were able to identify Au-Ge traps in the depletion region which contributed to both irreversible and reversible tunneling processes [161]. NDR degradation is also observed in AlGaN/GaN double barrier resonant tunneling diodes (RTDs) [162], [163]. Bayram *et al*. revealed that less degradation was observed in the

RTDs with less aluminum content or lattice mismatch at the barriers, and less strain-induced defects [162], [163]. Additionally, they determined the substrate dislocation density greatly affects the repeatability and peak-to-valley ratio of the NDR when comparing lateral epitaxial overgrowth (LEO) GaN on sapphire to free-standing GaN templates [163]. Most AlGaN/GaN RTDs and GaN tunnel junctions are thus grown on free-standing GaN templates that can exhibit up to 50 times fewer threading dislocations when compared to the GaN templates grown on sapphire in this work. This work demonstrates a GaN homojunction exhibiting NDR that was not grown on a free-standing GaN template, but on a GaN template on sapphire instead.

4.3.3 Current-Voltage Measurements of Tunnel-Contacted GaN Devices

The current-voltage plots of samples B1-B4 with the n++/p++/i/n structure are shown in Figure 4.5. Note that the TJs are reverse biased when the underlying p/i/n diode is forward biased. Since the TJs are reverse biased, there is no variability of the current-voltage characteristics with consecutive scans as is only found for the tunnel junction in forward bias in the NDR region only. As the silicon doping at the tunnel junction increases from sample B1 with the lowest silicon doping to sample B3 with the highest silicon doping, the TJs become more conductive in reverse bias, as illustrated in Figure 4.3. Thus, as the silicon doping increases from samples B1 to B3, the TJ resistance decreases, and the current-voltage characteristic becomes more comparable to that of sample B4 (the control sample without a TJ). The turn-on voltages of sample B1, B2, B3, and B4 are 4.37, 3.18, 3.12, and 2.98 V, respectively. The specific on-resistance is 9.43×10^{-4}, 4.85×10^{-4}, 3.24×10^{-4}, and 3.75×10^{-4} Ω-cm^2 for sample B1, B2, B3, and B4, respectively. Even though the

best TJ contacted diode (sample B3) turns on at a barely higher voltage, the specific on-resistance is slightly (13%) lower compared to the control device, most likely due to a higher p-type contact resistance for sample B4. The highest silicon doped device only resulted in a ~0.14 V increase in the turn-on voltage when compared to the control device, which is an acknowledgment that even though the TJ contacted device has lower series resistance at high current, the added TJ requires voltage drive. It is worth noting that while TJ sample A3 had a ~1.8 V reverse bias drop at ~1250 A/cm^2, when the same TJ is added in series to the pin device B3, its added voltage drop at the same current was only ~0.1 V. This discrepancy is likely related to a high mesa top p-contact resistance as determined from separate TLM test structures similar to sample A3 of ~6.6 x 10^{-3} Ω-cm^2 compared to the mesa top n-contact resistance of ~2.8 x 10^{-5} Ω-cm^2 for a TLM structure similar to sample B3.

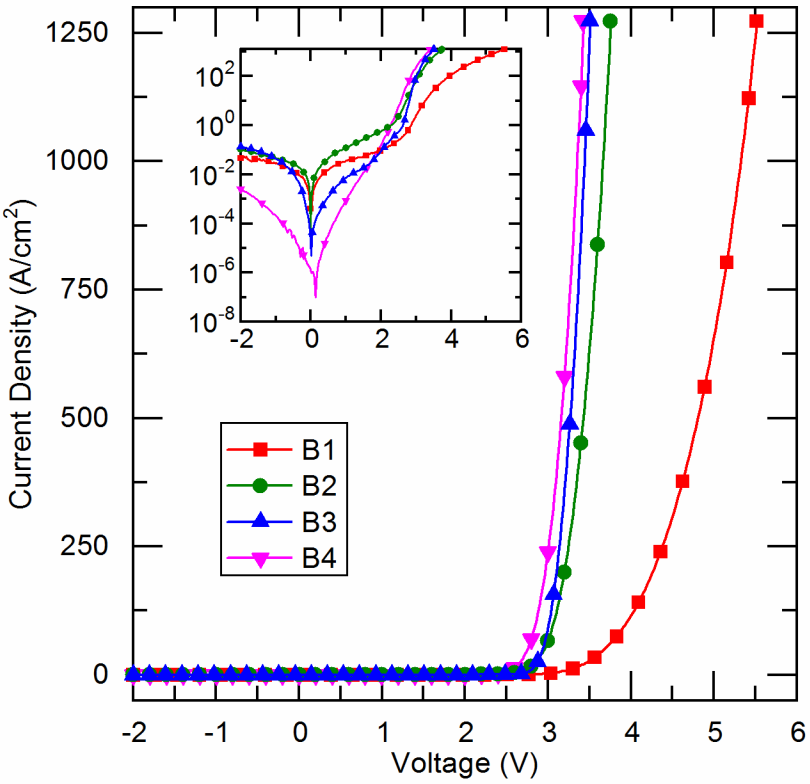

Figure 4.5. Current density versus voltage for 100 µm diameter circular mesa devices fabricated from samples B1-B4. As the silicon doping concentration increases from the lowest doping in B1 to the highest in B3, the tunnel contacted diodes approach the control sample B4. Inset: semi-log current-voltage characteristics of B1-B4.

4.4 Conclusions

In conclusion, metal modulated epitaxy is capable of producing high doping concentrations and abrupt doping profiles necessary for growing low resistance tunnel junctions without an annealing step. Negative differential resistance at room temperature and 77 K is observed for a GaN homojunction diode grown on highly dislocated templates on sapphire. The presence of charge trapping, resulting in an increased tunnel current with

consecutive voltage sweeps, and a large theoretical depletion width both suggest that the defect assisted tunneling is more likely the main tunneling mechanism rather than Esaki style band-to-band tunneling. Initial efforts to incorporate MME TJs as tunnel contacts to p/i/n diodes resulted in a low ~0.14 V increase in the turn-on voltage and a 13% decrease in the series resistance when compared to a control device without a TJ. TJs grown via MME can enable series-connected devices with embedded p-type layers and improve the overall performance of III-nitride-based devices and their design freedom.

CHAPTER 5: EXTREME Mg-DOPED AND DELTA DOPED GaN HOMOJUNCTION TUNNEL DIODES

5.1 Introduction

Initial GaN homojunction tunnel diodes are explored in chapter 4. In that chapter, a heavily doped TJ interface is formed in the tunnel diode, where the Si concentration and thus electron concentration is modulated at the tunnel junction interface. The results in chapter 4 indicate that some sort of trap-assisted tunneling in combination with the extremely narrow depletion width and high doping can enable tunneling.

The understanding of the tunneling and negative differential resistance in forward bias is still unclear. The type of defect that is promoting tunneling, and that particular defect's relationship to the extreme n- and/or p-type doping process is desired. Thus, a further exploration of the doping at the tunnel junction is performed in this chapter.

5.2 Experimental Procedure

Four GaN homojunction tunnel diodes C1-C4 are grown on n-type GaN templates with various Mg doping concentrations ranging from 1.5×10^{20} cm^{-3} to 7.8×10^{20} cm^{-3} at the TJ interface, since the previous study in chapter 4 was only investigating changing the Si concentration. The doping details of the four samples are listed in Table 5.1. The samples

were fabricated into 200 μm diameter circular mesas using standard GaN fabrication techniques.

Table 5.1. Doping concentration details for the GaN homojunction tunnel diodes. The extreme Si concentration is kept at a high value, while the Mg concentration is varied.

Sample ID	**TJ Si (cm^{-3})**	**TJ Mg (cm^{-3})**
C1	4.6×10^{20}	1.5×10^{20}
C2	4.6×10^{20}	3.4×10^{20}
C3	4.6×10^{20}	5.3×10^{20}
C4	4.6×10^{20}	7.8×10^{20}

The range of Mg doping was selected based on the doping calibration in chapter 3. The Mg concentrations result in hole concentrations reaching a maximum 1.5×10^{20} cm^{-3} for sample C3, and then begin to self-compensate for C4. Sample C4 will explore if the compensating defects help or limit the tunneling mechanism. On the n-type side of the TJ, the Si concentration is set to a high value of 4.6×10^{20} cm^{-3}, which results in an electron concentration of ~3.1×10^{20} cm^{-3}. The structure of the GaN homojunction tunnel diodes is the same as the one in chapter 4, and is shown in Figure 5.1.

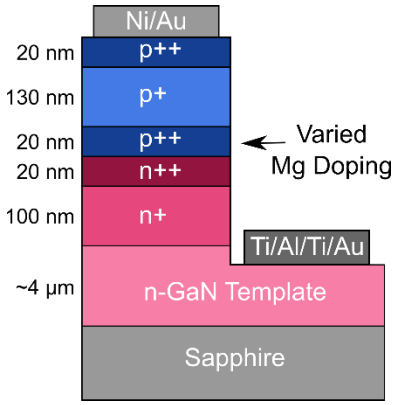

Figure 5.1. GaN homojunction tunnel diode structure with a varied Mg doping concentration at the tunnel junction interface.

5.3 Results and Discussion

5.3.1 Current-Voltage Measurements of Extreme Mg-Doped GaN Tunnel Diodes

The current-voltage measurements were taken on samples C1-C4 and are shown in Figure 5.2. When increasing the Mg concentrations from C1-C3, the hole concentrations increase up to the maximum 1.5 x 10^{20} cm^{-3}, resulting in negative differential resistance in forward bias for sample C3, as seen in Figure 5.2(a). The NDR voltage is 1.8 V, while the peak current density is 146 A/cm^2, and the peak-to-valley current ratio is 1.09. Additionally, the reverse bias and forward bias conductivity is increased when the Mg concentration increases from C1 to C3. The higher current density in the low reverse bias condition between -1 and 0 V when compared to the low forward bias condition between 0 and 1 V indicates reverse bias tunneling is present.

When the Mg concentration is further increased and the hole concentration is self-compensated, the NDR vanishes, and the conductivity of device C4 decreases in comparison to C3.

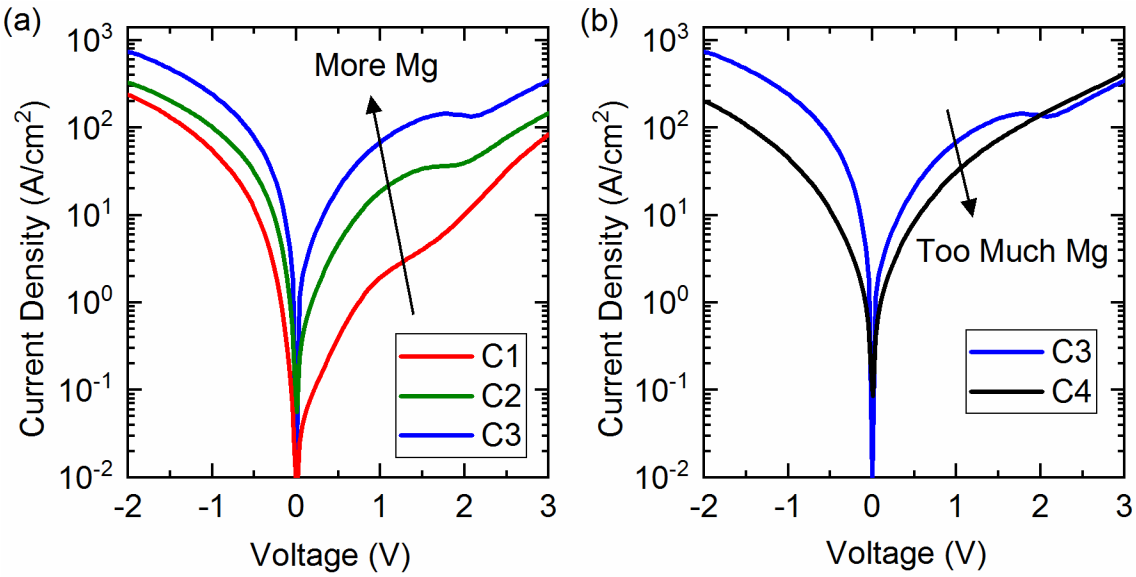

Figure 5.2. Semi-log current-voltage measurements for the GaN homojunction tunnel diodes (a) C1-C3 and (b) C3-C4 with various Mg concentrations in the p++ layer at the TJ interface.

The results in Figure 5.2 indicate that there is an interplay between the extreme hole concentrations and the defect concentrations that contribute to tunneling. It is speculated that the defect concentration that limits the conductivity in C4 prevents the tunneling mechanism. Either the defects that contribute to tunneling in sample C3 are different than the ones that limit tunneling in C4, or the hole concentration reduction for sample C4 causes an increase in the depletion width that reduces the tunneling probability for electrons.

5.3.2 Structural Analysis of a GaN Homojunction Tunnel Diode with NDR

In order to further examine the structural quality of the sample C3 with negative differential resistance, scanning transmission electron microscopy (STEM) high-angle annular dark field (HAADF) cross-sectional images are taken and are shown in Figure 5.3. The STEM images indicate that there are no significant defects generated by the MME-grown GaN layers. The extreme doping at the TJ does not add additional defects that propagate to the layers above and subsequent epitaxy.

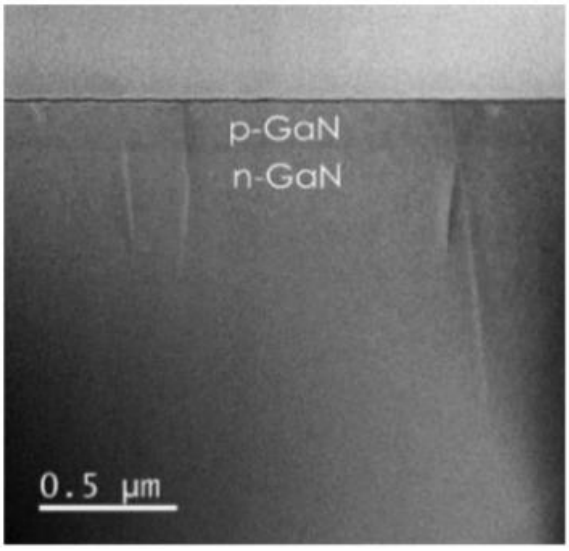

Figure 5.3. Scanning transmission electron microscopy high-angle annular dark field (HAADF) image of the GaN homojunction tunnel diode sample C3 with NDR.

These STEM results are promising, because they indicate that MME-grown TJs can be implemented into optoelectronic devices, such as tunnel-contacted LEDs or lasers, as well as series connected devices. If the layers above the TJ were highly defective, they would limit optoelectronic device performance, such as the light extraction efficiency (LEE) for a tunnel contact, or the quantum efficiency for an LED grown on top of a TJ.

5.3.3 Temperature-Dependent Current Voltage Measurements

Temperature-dependent measurements from 77 to 300 K for sample C3 are taken and shown in Figure 5.4. Notably, the NDR in the device is present even at 77 K, which further indicates a temperature-insensitive tunneling mechanism is present. An increased series resistance in the device (*e.g.* contact resistance) may also shift the peak voltage higher and the peak current density lower at low temperatures.

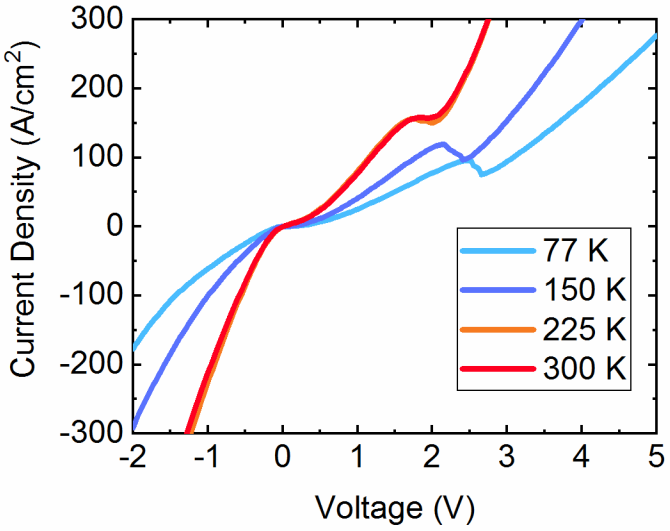

Figure 5.4. Temperature-dependent current-voltage measurements for sample C3. The negative differential resistance and reverse-bias tunneling are present even at 77 K, indicating a tunneling mechanism is present.

The NDR peak voltage increases to 2.4 V and the peak current density reduces to 96 A/cm^2 as the temperature lowers. The PVCR increases from 1.09 at room temperature up to 1.24 at 77 K. It is speculated that the defect alignment for any defect-assisted tunneling may shift in such a way to require a higher voltage drive. Alternatively, any

carrier freezout or temperature-dependent process that increases the contact resistance and thus total device resistance may result in a similar temperature-dependent trend.

5.3.4 A Comparison of Tunnel Diodes Grown on Sapphire and Free-Standing GaN

The GaN homojunction tunnel diodes discussed in this work are speculated to have negative differential resistance in forward bias due to some form of defect-assisted tunneling, which results in a high peak voltage. Traditionally, in other material systems the peak voltage for tunnel diodes is in the millivolt range, and is related to the doping degeneracy of both the n- and p-type sides of the TJ.

In order to help determine the defect associated with the tunneling mechanism, a GaN homojunction tunnel diode was grown on a free-standing GaN template and compared to the previously discussed devices grown on sapphire. The devices grown on free-standing templates have dislocation densities of ~10^7 cm^{-2}, while the devices on sapphire have dislocation densities of ~10^9 cm^{-2}. Furthermore, the free-standing GaN templates have ~300 μm of a conducting template, and thus better current spreading underneath the device.

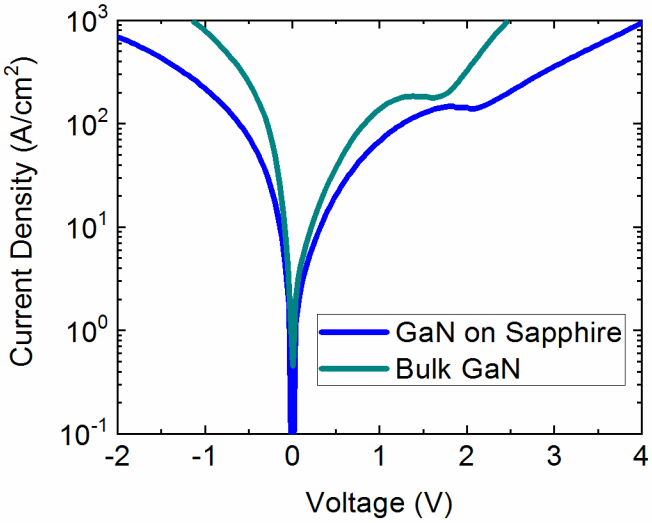

Figure 5.5. Semi-log current-voltage measurements for GaN homojunction tunnel diodes grown on low dislocation density bulk GaN and on high dislocation density sapphire. Both devices exhibit tunneling in reverse bias and negative differential resistance in forward bias.

The semi-log current-voltage measurements for the GaN homojunction tunnel diodes grown on both a free-standing bulk template, as well as on a sapphire template are shown in Figure 5.5. For the entire voltage range, the current density for the device grown on the free-standing templates is higher than on sapphire, due to the lower resistance substrate. The negative differential resistance regime peak voltage, peak current density, valley current density, and peak-to-valley current ratio are listed for both samples in Table 5.2. The peak voltage, and current densities are higher for the device grown on bulk GaN, indicating that the substrate resistance may be the only difference between these devices.

Table 5.2. GaN homojunction tunnel diode negative differential resistance parameters for

devices grown on different substrates.

Substrate	V_{peak} (V)	J_{peak} (A/cm^2)	J_{valley} (A/cm^2)	PVCR
GaN/Sapphire	1.80	146.9	140.0	1.05
Bulk GaN	1.39	184.2	178.6	1.03

Interestingly, the 100x reduction in dislocation density for the sample grown on bulk free-standing GaN does not eliminate the tunneling mechanism, and the PVCR remains similar. Thus, it is speculated that the defect-assisted tunneling is not primarily due to threading dislocations, but instead some other defect such as stacking faults or point defects associated with the extreme doping.

5.3.5 Delta-Doped GaN Homojunction Tunnel Diodes

Delta-doping is explored and applied to GaN homojunction tunnel diodes to further examine the tunneling mechanisms and ranges of conductivity for the devices. Delta doping is a technique where a high dose of a dopant is inserted into a structure in an ideally ultrathin layer. Delta doping can provide high concentrations of impurities for doping, while limiting the impurity induced scattering to a thin layer, and thus is well suited for lateral carrier injection. Some research has shown that Si delta doping can annihilate threading dislocations that have a screw component [164]. The Si will bend the trajectory of the threading dislocation and increase the likelihood that it will interact or pair with another dislocation and annihilate by forming a loop.

5.3.6 Experimental Procedure for Delta Doping

Four GaN homojunction tunnel diodes with various amounts of delta doping around 2-5 x 10^{14} cm^{-2} are grown and fabricated into devices and compared to a sample without delta doping. The delta-doping details and sample IDs are detailed in Table 5.3.

Table 5.3. Delta-doping details for GaN homojunction tunnel diodes

Sample ID	**TJ Si (cm^{-3})**	**TJ Mg (cm^{-3})**	**δ-Doping (cm^{-2})**
δ-0s	4.6 x 10^{20}	5.3 x 10^{20}	0
δ-Si 20s	4.6 x 10^{20}	5.3 x 10^{20}	2.3 x 10^{14}
δ-Si 40s	4.6 x 10^{20}	5.3 x 10^{20}	4.6 x 10^{14}
δ-Mg 20s	4.6 x 10^{20}	5.3 x 10^{20}	1.5 x 10^{14}
δ-Mg 40s	4.6 x 10^{20}	5.3 x 10^{20}	3.0 x 10^{14}

The delta-doping is inserted in between the heavily n- and p-type doped layers forming the tunnel junction. The position of the delta-doping, as well as the MME shuttering scheme to achieve the delta doping is shown in Figure 5.6.

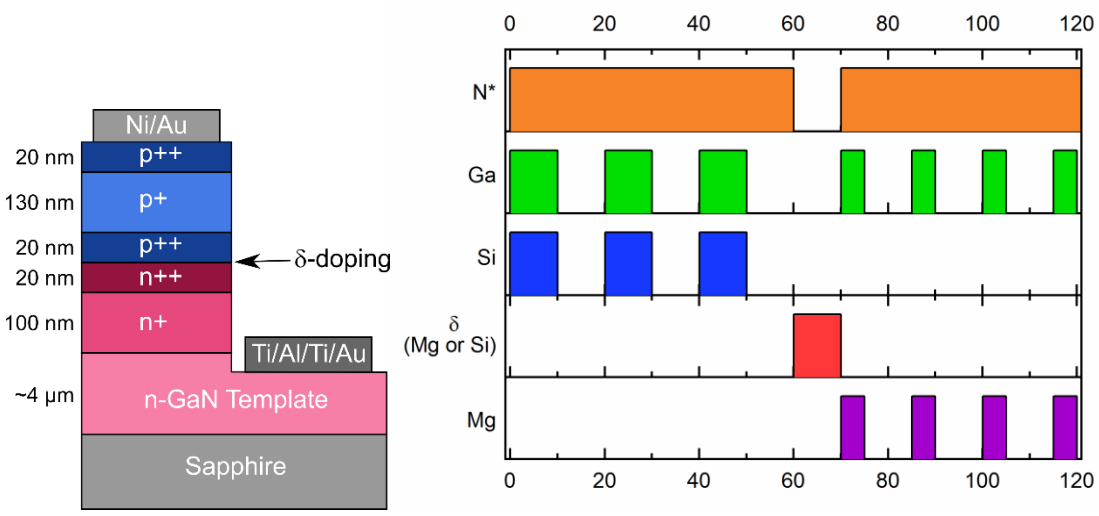

Figure 5.6. Delta-doped GaN homojunction tunnel diodes (left) structure and (right) MME shuttering scheme.

The shuttering scheme shown in Figure 5.6(b) is an example of a 10s dose of delta doping. To form the tunnel junction, the MME Si-doped n-type GaN is grown by shuttering the Ga and Si open and closed (from 0 to 60 s), and once completed, the nitrogen shutter is closed and the delta dopant (either Mg or Si) is exposed to the surface (from 60 to 70 s). The nitrogen shutter is closed to limit any Si_xN_y or Mg_xN_y compounds from forming. Next, the MME Mg-doped p-type GaN is grown by shuttering the Ga and Mg open and closed (from 70 to 120 s). Since these devices are p-side up and the p-layer is grown directly on top of the delta doped layer, there is a chance that there is some amount of incorporation of the delta dopant into the initial few angstroms of the p-type GaN. When Mg is the delta dopant, the initial few angstroms may simply be more heavily Mg-doped. When Si is the delta dopant, the initial few angstroms of the p-layer may have both Mg and Si, and thus be compensated via co-doping. Further delta doping studies with p-down structures may reveal if this is an issue.

5.3.7 Current-Voltage Measurements of Delta-Doped Tunnel Diodes

The current-voltage results for the delta-doped samples are shown in Figure 5.7. All four of the delta-doped samples are more conductive than the control in low forward bias, but they have higher series resistance, likely due to elevated impurity scattering. No delta-doped sample exhibits NDR. A future study involving a lighter dose of both the delta doping and the TJ doping may provide the best NDR. The Mg delta doping seems to perform better than the Si delta doping. This is either because the defect-assisted tunneling mechanism is Mg related, or because the Si delta doping compensates the Mg doping in the subsequent p-type layers in this p-up structure.

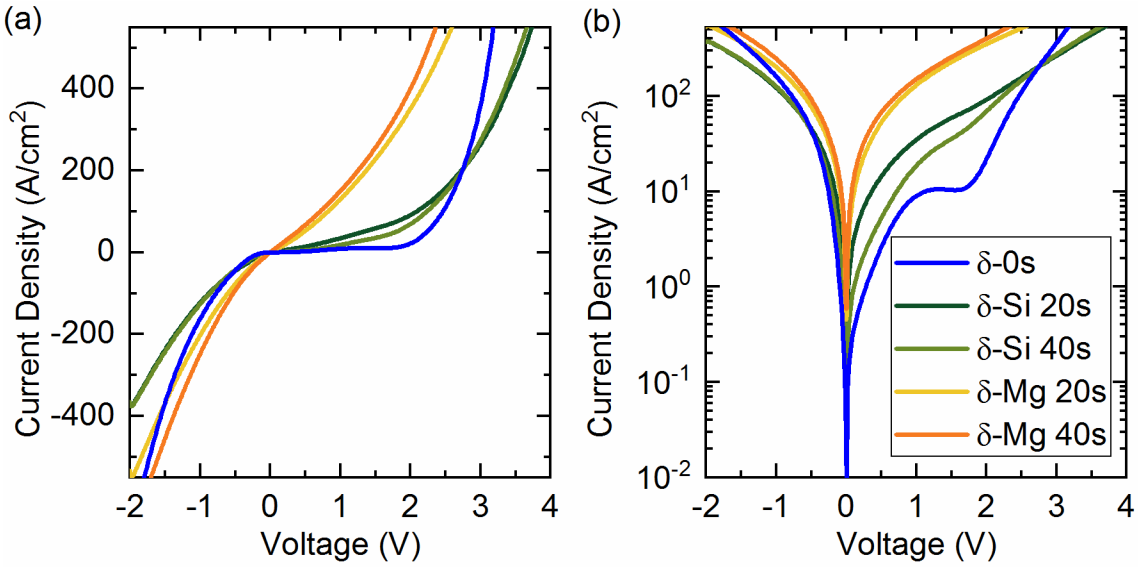

Figure 5.7. Delta-doped GaN homojunction tunnel diode (a) linear and (b) semi-log current-voltage measurements.

5.3.8 Structural quality of Delta-Doped Tunnel Diodes

The Mg delta-doped samples were measured in AFM to examine if any major structural degradation occurred due to the extreme doping. The AFM 5 x 5 μm^2 scans of

the Mg delta-doped samples are shown in Figure 5.8. Both samples are ~1.3 nm RMS roughness.

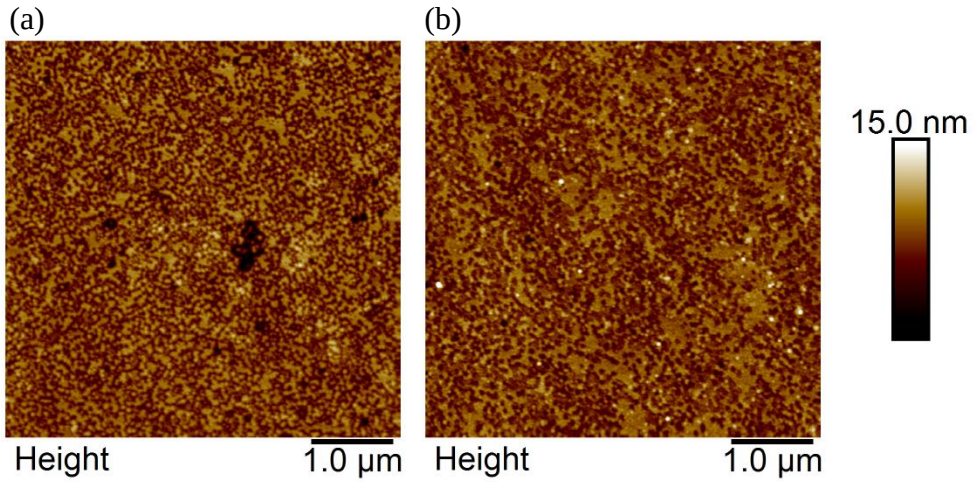

Figure 5.8. Atomic force microscopy 5 x 5 μm^2 scans of the Mg delta-doped samples (a) δ-Mg 20s and (b) δ-Mg 40s.

STEM high resolution images were taken on the δ-Mg 40s sample and are shown in Figure 5.9. Figure 5.9(a) shows a threading dislocation generating at the delta doping layer, but this may be an anomaly since it is the only threading dislocation in the image. The subsequent p-GaN layer does not appear to have deteriorated quality from the underlying delta-doped layer other than the threading dislocation. Figure 5.9(b) is a high resolution image at the tunnel junction interface where the delta doping can be identified. These results are encouraging for incorporating delta doped TJs into optoelectronics.

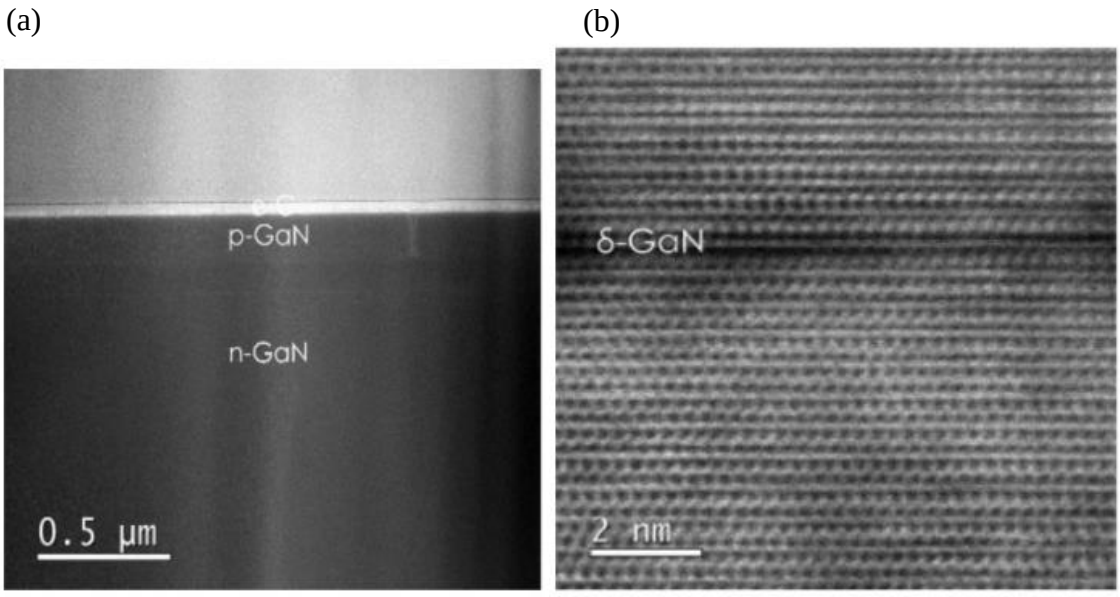

Figure 5.9. STEM images of the δ-Mg 40s sample (a) entire structure and (b) delta-doping tunnel junction interface

5.4 Conclusions

In conclusion, extreme Mg-doped and delta-doped GaN homojunction tunnel diodes are studied. The Mg-doping can be tuned to enable NDR that is measurable even down to 77 K. Threading dislocations are likely not the main contributor to the defect-assisted tunneling mechanism. Delta doping can result in highly conductive tunnel diodes in a forward bias application, such as a solar cell, or an LED that may require less significant doping. Although this work demonstrates very conductive tunnel junctions, the extreme bulk doping and delta doping must be implemented into devices to determine the consequences of the doping on the device performance.

CHAPTER 6: HYBRID MBE-GROWN TUNNEL-CONTACTS TO MOCVD-GROWN LEDS AND SOLAR CELLS

6.1 Introduction

Tunnel contacts can be grown atop other epitaxial stacks that are previously grown in a different system, as long as the underlying layer structure is compatible. Most III-nitride optoelectronic devices are grown with a p-type surface layer, and thus, a tunnel-contact can be added by simply re-growing an n-type layer on top, or by re-growing a p- and n-type layer to form the junction.

The hybrid approach is most commonly implemented by growing n-type MBE tunnel contacts atop MOCVD grown structures such as LEDS [152], [165], [166]. The motivation for this approach is that the MOCVD technique has been optimized for high efficiency LEDs and is benefitted by In clustering which enhances brightness [167]. The MOCVD LED wafer structure is completed with a surface p-type layer. The wafer is then transferred to an MBE where the n++ tunnel contact is grown because the physical vapor deposition allows for extreme n-type doping.

The MBE on MOCVD hybrid approach is convenient because it avoids the Mg memory effect, where Mg tends to linger in an MOCVD system after the p-type layer is grown, and thus Mg can unintentionally incorporate into subsequent layers [154]. If a tunnel junction were to be grown entirely in an MOCVD system, forming an abrupt junction is difficult due to the Mg memory effect, because the n-type layer may be

compensated with unintentional Mg.

Another convenient benefit of the hybrid MBE on MOCVD approach is that it is compatible with the p-type anneal which is required to activate Mg-doped GaN grown via MOCVD [77]. The MOCVD technique requires the p-type anneal to out-diffuse hydrogen from the Mg-doped p-layer, since hydrogen can form complexes with Mg in un-annealed p-type layers resulting in low hole concentrations. If a tunnel junction were formed completely via MOCVD, the buried p-type layer would be difficult to anneal out the H from since H does not diffuse as well vertically through n-type layers [157]. Although some groups have demonstrated that for buried p-type layers in micro-LEDs that hydrogen can laterally out-diffuse from the mesa sidewalls if they are sufficiently small to enable diffusion from the innermost hydrogen [156], [168]. Recent work has demonstrated the ability to *in-situ* anneal MOCVD p-layers, and is promising for buried p-layer devices [169]. Nevertheless, it is convenient for the hybrid approach to form the tunnel contact with an MBE system after the traditional *ex-situ* annealing step of the MOCVD p-layer is performed.

One of the major difficulties with a hybrid approach is the contamination at the regrowth interface. Yonkee *et al*. have measured these interfaces with the SIMs technique and observed that an elevated oxygen content at the regrowth interface can result in a large voltage penalty for the tunnel junction and that an aqua regia or HF clean of the wafer before the regrowth of the tunnel contact can lower the oxygen content and voltage penalty [170]. The contaminants at the interface can compensate the doping concentrations and be extremely detrimental to the tunnel contact performance, especially if the tunnel junction interface is at the regrowth interface. Thus, the regrowth cleaning and sample preparation

steps are critical to the hybrid approach.

6.2 Experimental Procedure

Two sets of hybrid MBE on MOCVD solar cell and LED structures are grown and characterized. First, two different hybrid MBE tunnel contacts are grown on MOCVD-grown solar cells and compared to a control sample with a conventional indium tin oxide (ITO) current spreading layer. The MOCVD-grown wafers are cleaned with a piranha solution and an HF dip to remove any oxides prior to the MBE regrowth. The MOCVD solar cell consists of a 20x InGaN/GaN multi-quantum well region for absorbing light. Next, two different tunnel contacts are grown on an MOCVD-grown LED and similarly compared to a control sample with ITO. The MOCVD LED consists of a 9x InGaN/GaN multi-quantum well active region for emitting light. When the solar cell and LED are in operation, the tunnel junctions will be biased in different directions. In the solar cell, absorbed photons will generate electron-hole pairs, where the holes and thus current will drift towards the p-layer and then tunnel into the MBE-grown contact. In the LED, holes will be injected from the tunnel contact and diffuse towards the active region to emit light. Therefore, the tunnel junction will be in forward bias for the solar cell and in reverse bias for the LED. The effects of the tunnel contacts atop these two structures will investigate the viability for MME-grown tunnel contacts in forward and reverse bias.

The hybrid-grown MME on MOCVD solar cell structure is shown in Figure 6.1. The device starts with a 1 µm thick lightly doped n-type GaN buffer layer, followed by a more heavily doped Si-doped 4.5 µm thick n-type GaN contact layer. The MQW region consists of 20x pairs of 3.0 nm thick InGaN wells and 5.6 nm thick GaN barriers. A 150 nm p-type GaN layer with $2x10^{19}$ cm^{-3} Mg doping followed by a 10 nm p+ contact layer with $1x10^{20}$ cm^{-3} Mg doping is grown above the MQW stack. The hole concentration for the p+ layer was measured to be ~$2x10^{18}$ cm^{-3}, much lower than achievable via MME.

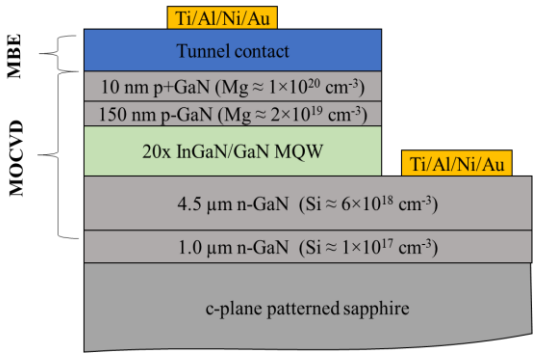

Figure 6.1. Device structure for a tunnel-contacted hybrid MBE on MOCVD solar cell consisting of a 20x InGaN/GaN MQW absorbing region.

The MME tunnel contact is grown on top of the MOCVD-grown p+ GaN contact layer. Two types of tunnel contacts are grown. First, sample N++ consists of a 170 nm n++ layer grown to form the tunnel junction interface between the MBE n++ layer and the MOCVD p-type layer. Next, sample N++/P++ consists of a 20nm thick MME-grown heavily Mg-doped p++ layer on top of the MOCVD p-type layer and then a 170 nm thick n++ layer. Sample N++ will have the TJ interface at the growth interface, while sample P++/N++ will have the TJ interface 20 nm away from the growth interface. The two structures are detailed in Table 6.1 and are compared to a control sample that has ITO

deposited on top of the MOCVD p-type layer for current spreading.

Table 6.1. Doping details for the hybrid MBE on MOCVD tunnel contacted solar cells

Sample ID	TJ Si (cm^{-3})	TJ Mg (cm^{-3})	Regrowth Thickness (nm)
N++	4×10^{20} (MBE)	1×10^{20} (MOCVD)	170
N++/P++	7×10^{20} (MBE)	7×10^{20} (MBE)	190
Control	NA	NA	NA

6.3 Results and Discussion

6.3.1 Structural Quality of Hybrid-Grown Solar Cells

5 x 5 μm^2 AFM images of the three samples are measured and are shown in Figure 6.2. The control sample's p+ MOCVD layer (before ITO deposition) is shown in Figure 6.2(a), and is the starting surface for the regrowth layers. Sample N++ and N++/P++ both exhibit spiral hillocks, which are indicative of step-flow growth and a smooth film. The RMS roughness of all three surfaces in Figure 6.2 is <0.5 nm. The AFM results are promising because they demonstrate the hybrid technique is feasible. A wafer can be epitaxially grown in an MOCVD reactor, then exposed to air, and epitaxial growth can resume in another system such as an MBE chamber.

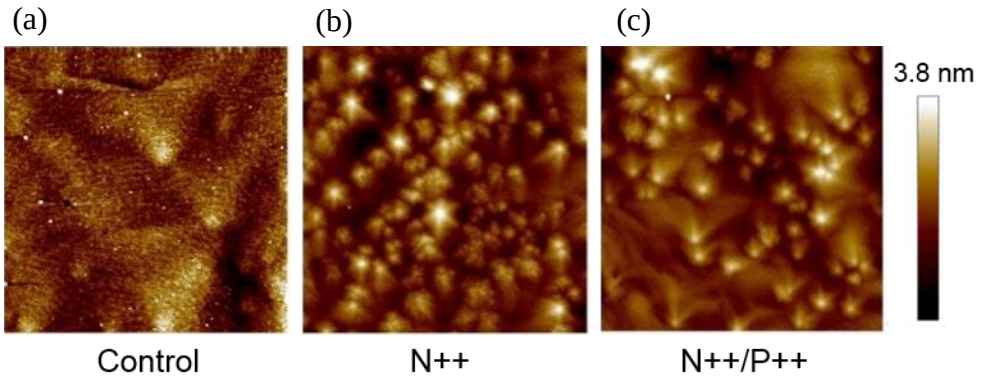

Figure 6.2. 5 x 5 μm^2 AFM images for the (a) control sample before ITO deposition, (b) N++ sample, and (c) N++/P++ samples.

Next, the samples were measured in XRD, and a representative diffractogram for sample N++/P++ is shown in Figure 6.3. Superlattice features are present in the scan from the MQW active layer. The periodicity of the superlattice features is measured to be ~8.5 nm, which corresponds with the designed QW and QB thickness of ~8.6 nm. Notably, the XRD does not indicate any extreme phase separation, but instead a single InGaN peak at ~34.3°. The tallest peak at ~34.6 corresponds to the GaN layers, which primarily consists of the thick GaN substrate.

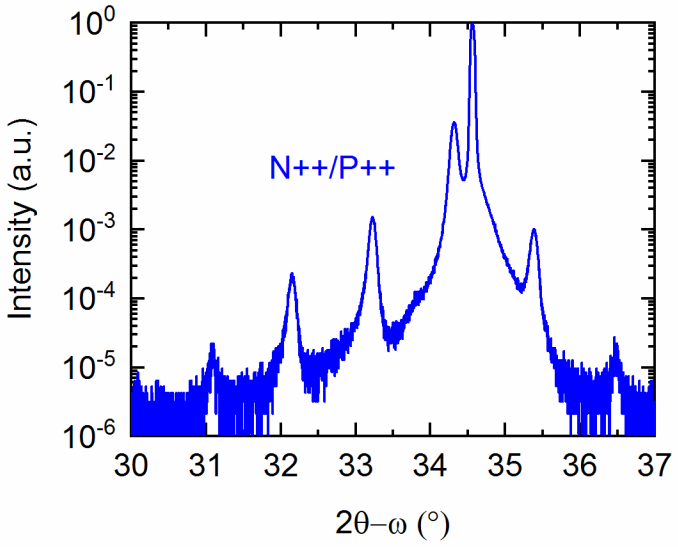

Figure 6.3. Sample N++/P++ representative X-ray diffraction (0002) 2θ-ω scan for the hybrid-grown InGaN solar cells.

6.3.2 Electrical and Solar Measurements for Hybrid-Grown Solar Cells

The solar cells' current-voltage measurements are taken in the dark, and under one-sun AM1.5G illumination using an Oriel class A solar simulator. The results are shown in Figure 6.4. The dark J-V measurements in Figure 6.4(a) indicate that the turn-on voltage for the control sample is the lowest, while the N++/P++ sample and the N++ sample have voltage penalties associated with turning on the extra TJ. The higher turn-on voltage will reduce the carrier extraction of the cell. The illuminated J-V results in Figure 6.4(b) illustrate how well each cell collects light.

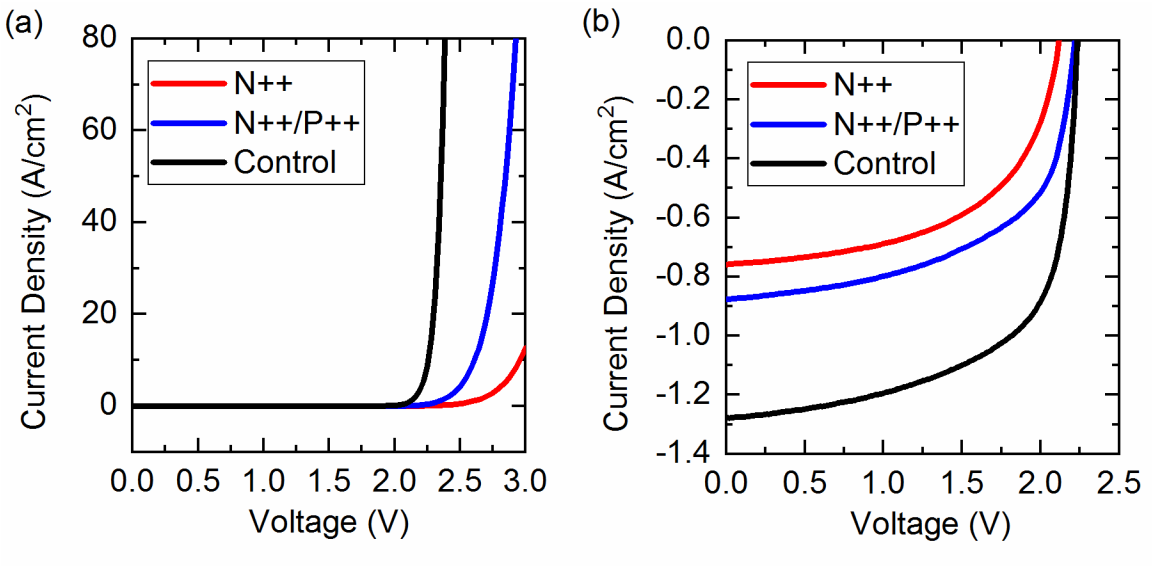

Figure 6.4 Solar cell current-voltage measurements for (a) no illumination, and (b) under AM1.5G solar illumination.

The solar cell parameters for each sample is listed in Table 6.2. The short-circuit current density (J_{sc}) of the control sample, sample N++/P++, and sample N++ are 1.28, 1.02, and 0.76 mA/cm^2, respectively. The open-circuit voltage (V_{oc}) for the control sample, sample N++/P++, and sample N++ are 2.24, 2.20, and 2.00 V, respectively. By moving the tunnel junction away from the growth interface for sample N++/P++, the efficiency increases significantly from 0.9% in sample N++ to 1.32 %.

Table 6.2. Electrical characteristics for the hybrid and the control InGaN solar cells.

Sample ID	**Jsc (mA/cm^2)**	**V_{oc} (V)**	**FF (%)**	**η (%)**	**W_{oc} (V)**
N++	0.76	2.00	59	0.90	0.95
N++/P++	1.02	2.20	59	1.32	0.75
Control	1.28	2.24	64	1.82	0.71

These first attempt hybrid-grown samples do not perform as well as the control sample. One potential reason is that the series resistance is high in the hybrid structures. The series resistance for the N++/P++ sample is 3.2 Ω-cm^2, while it is only 0.08 Ω-cm^2 for the control sample. To further examine where the control sample outperforms the hybrid grown tunnel-contacted samples, external quantum efficiency measurements are taken and shown in Figure 6.5. The control sample is significantly more efficient in the 300-360 nm wavelength range. This is likely because the additional 170-190 nm MBE-grown GaN layers absorb light in that range. Thus, it is advised to optimize the hybrid growth thickness to minimize this effect.

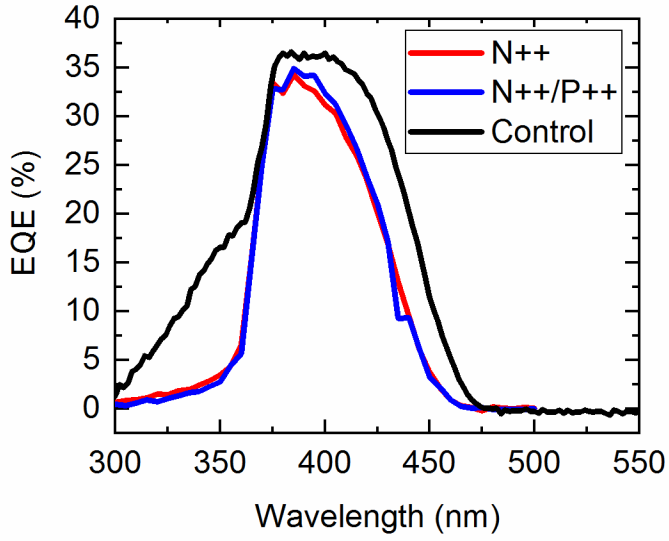

Figure 6.5. External quantum efficiency for the hybrid and control InGaN solar cells. The control cell has better performance in the shorter wavelength region.

While the hybrid tunnel-contacted samples are not as efficient solar cells when compared to the control sample, but they are an exciting result and a first demonstration of a forward biased GaN tunnel contact in operation. These heavily doped tunnel contacts can

be inserted in series between two cells for a tandem or multi-cell stack. The tunnel junctions are conductive in forward bias and compatible with subsequent epitaxy, but must be thin to prevent unwanted absorption.

6.3.3 Electrical and Light-Output Measurements for Hybrid-Grown LEDs

A hybrid grown tunnel contact study is performed on an LED structure and is similar to the solar cell study discussed above, with the major difference being the LED structure contains a 9x InGaN/GaN MQW active region. The entire LED structure is shown in Figure 6.6. The tunnel contacts are similar in nature to the solar cell study, and the TJ doping details and sample surface morphology can be found in Table 6.1 and Figure 6.2, respectively.

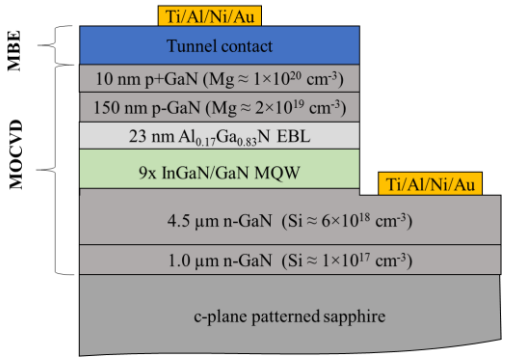

Figure 6.6. Device structure for a tunnel-contacted hybrid MBE on MOCVD LED consisting of a 9x InGaN/GaN MQW emitter.

The current-voltage results for the LEDs are shown in Figure 6.7. Similar to the solar cell results, the N++ sample has the highest voltage penalty in comparison to the

control sample, which is likely because the p-side of the N++ tunnel junction is a lower hole concentration MOCVD-grown p-type layer. The N++/P++ sample still has a voltage penalty in comparison to the ITO sample, indicating that even with a high hole concentration regrowth layer, the regrowth contaminants may be compensating the tunnel junction doping and thus contributing to the voltage penalty.

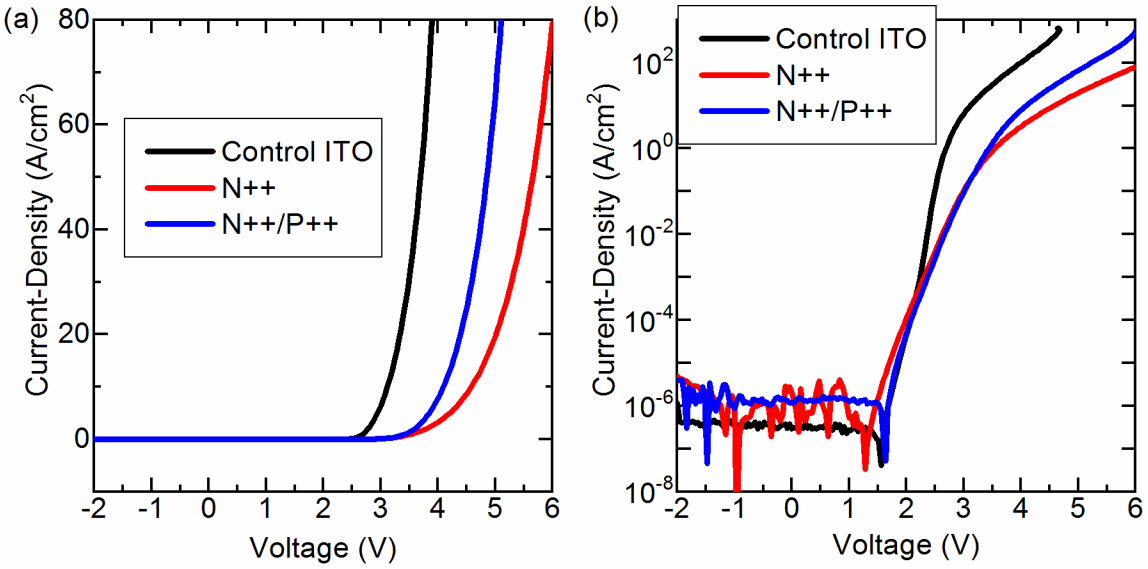

Figure 6.7. Hybrid tunnel contacted and control LEDs' (a) linear and (b) semilog current-voltage measurements.

Although the control LED with an ITO current spreading layer requires less power to drive the device to a particular current, the N++/P++ sample has superior current spreading at 0.5 mA injection, and is shown in Figure 6.8. The low resistance n-type surface layer provides built-in current spreading for the tunnel-contacted devices without requiring an additional current spreading layer deposition. These tunnel-contacted LEDs may be compatible with high temperature operation, unlike the ITO which breaks down.

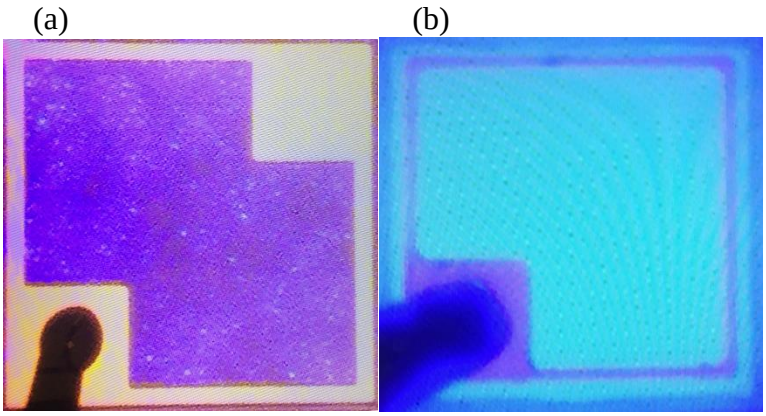

Figure 6.8. Images of the (a) control LED with ITO and (b) tunnel contacted N++/P++ LED at 0.5 mA operation

The emission spectra are compared at an injection current of 0.5 mA and shown in Figure 6.9. The control and tunnel contacted LEDs have similar spectra, centered at ~470 nm, with the tunnel-contacted sample being only slightly broader. Therefore, the process of depositing an MBE-grown tunnel contact does not significantly deteriorate the active area's light emission, but merely requires additional voltage to power the device which may be reduced in the future with optimized cleaning, doping, and layer thicknesses.

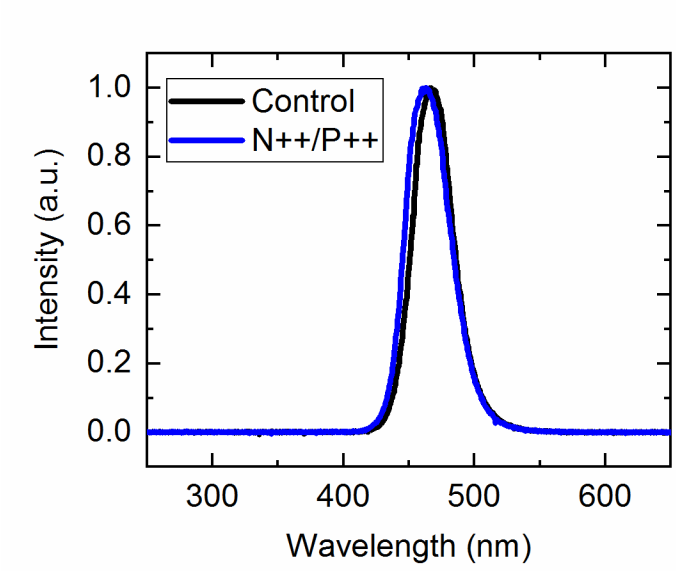

Figure 6.9. Emission spectra for the control and tunnel-contacted LEDs.

6.4 Conclusions

Hybrid MBE on MOCVD tunnel contacted solar cells and LEDs are demonstrated, and successfully operate. The hybrid technique is proven to be feasible and maintain epitaxial step-flow growth. The heaviest doped tunnel contacts with tunnel junctions away from the regrowth interface perform the best. The tunnel junctions are conductive in forward bias, which is essential for a solar cell and future tandem cells, but must be kept thin to prevent unwanted absorption. The tunnel-contacted LEDs are able to withstand high current densities, and have the benefit of built-in current spreading via the n-type top layer. Further optimization is required for both structures, but the results are encouraging for future series-connected and tandem devices.

CHAPTER 7: ULTRA-WIDE-BANDGAP AlGaN HOMOJUNCTION TUNNEL DIODES WITH NEGATIVE DIFFERENTIAL RESISTANCE

7.1 Introduction

AlGaN-based ultraviolet (UV) emitters, light-emitting diodes (LEDs) and lasers, have a broad range of applications, such as water and air purification, medical sterilization, and biochemistry [171]. However, the external quantum efficiency of AlGaN-based UV emitters dramatically reduces when reducing the emission wavelength further into the deep UV due to multiple growth and fabrication issues [92]. The low efficiencies and weak light extraction of AlGaN-based UV LEDs mainly stems from high threading dislocation densities, high UV absorption coefficients, poor hole injection of p-GaN layers, and high resistance of p-GaN contact layers [92]–[94].

Generally, as the bandgap and Al composition increases, the AlGaN film suffers from elevated defect densities, and increased ionization energies of dopants for both n- and p-type AlGaN (with different rates). The latter issue contributes to asymmetric carrier injection into the active region of LEDs (*e.g.*, lack of efficient hole injection), which causes electron leakage out of the active region. It is reported that among all causes of efficiency droop in LEDs, such as Auger recombination and defect-assisted Shockley-Read-Hall (SRH) recombination, insufficient hole injection is the key loss mechanism [172]–[174]. The hole injection issue can be dramatically improved by forming a homojunction tunnel junction (TJ), in which a transparent n-AlGaN top tunnel contact (TC) layer can be

connected to the p-AlGaN contact layer to improve light extraction and eliminate the need for flip-chip bonding. The use of an AlGaN TC instead of p-GaN leads to the reduction of parasitic optical absorption in the p-GaN contact layer while also providing high hole current with an ideally low turn-on voltage penalty resulting from the additional junction. In addition, AlGaN TJs can be connected to p-AlGaN cladding layers in edge-emitting lasers and n-type distributed Bragg reflectors in vertical-cavity surface-emitting lasers.

III-nitride-based TJs have been studied to series-connect devices, to reduce device fabrication steps (*e.g.*, combining n- and p-type contact patterning and metallization), but primarily as n-type TCs to p-type layers to substantially reduce contact resistance by orders of magnitude [74], [100], [175]. Low-resistance polarization engineered TJs have been demonstrated to enhance tunneling probabilities (*e.g.*, for GaN by inserting an interlayer typically InGaN or AlN) [176]. Nevertheless, the use of a heterojunction interlayer introduces material degradation due to lattice mismatch and parasitic light absorption. Furthermore, heterojunction TJs become increasingly more problematic as the AlGaN bandgap is increased. With higher Al compositions, the change in piezoelectric properties needed to form a polarization engineered junction is difficult without significant changes in the Al composition, and with higher growth temperatures is less practical by adding In.

Recently, GaN homojunction tunnel diodes (TDs) with negative differential resistance (NDR) and tunnel contacts to p/i/n devices have been introduced using plasma-assisted molecular beam epitaxy (PAMBE) with voltage penalties as low as 0.1 V [175]. The NDR in forward bias in these devices is suspected to be from defect-assisted tunneling and not from Esaki-style band-to-band tunneling. Although the tunneling mechanism is defect-assisted, the extreme n- and p-type doping is still required to narrow the depletion

width enough to enable any defect-assisted tunneling in forward bias. GaN-based homojunction and heterojunction TJs have been integrated into optoelectronic devices, such as LEDs [107], solar cells [74], vertical-cavity surface-emitting lasers (VCSELs) [177], and cascade LEDs [100]. However, achieving a low-resistance TJ for wide-bandgap AlGaN materials is extremely challenging because of high depletion widths (due to low doping concentrations in AlGaN) and large barrier heights (related to the bandgap of AlGaN). AlGaN homojunction TJs for UV optoelectronics are particularly difficult with traditional growth techniques such as metal-organic chemical vapor deposition (MOCVD) and MBE, where p-type doping is insufficiently low. Recently, polarization engineered TJs using AlGaN/GaN structures have been reported exhibiting low tunneling resistances of 9.4×10^{-4} Ω-cm^2 at 1.0 kA/cm^2 for a tunnel-contacted UV-LED operating at 292 nm [178], [179]. Similar to GaN, the aforementioned polarization engineered TJ can generate defects, light absorption, and growth complications. In this work, we demonstrate stand-alone heavily doped AlGaN p++/n++ homojunction TDs with NDR up to 19% Al and reverse bias tunneling characteristics up to 58% Al.

To achieve tunneling in homojunction AlGaN TJs, it is necessary to achieve both heavily doped n- and p-type films at high Al compositions. It has been reported that using silicon as an n-type dopant for $Al_xGa_{1-x}N$ is more favorable than germanium.[137] Silicon doping of $Al_xGa_{1-x}N$ in an MOCVD reactor has been reported up to x=1, but the ionization energy was measured to increase from ~8 (GaN) to 86 meV (AlN) [180]. P-type doping remains problematic for all III-N-based materials when employing traditional growth techniques, such as MOCVD or MBE. For MOCVD, the activation energy increases from ~170 meV for GaN to 510 meV for AlN [76].

In this work, the metal-modulated epitaxy (MME) growth technique at low temperatures (<720 °C) in a PAMBE chamber is implemented. MME has been reported to achieve hole concentrations up to 7×10^{19} cm^{-3} for GaN and lower the effective activation energy down to 43 meV [181]. Additionally, a hole concentration of 2.3×10^{19} cm^{-3} for an $Al_{0.27}Ga_{0.73}N$ film was reported using MME growth technique [158]. Such extreme p-type doping of AlGaN is likely due to a combination of the lower growth substrate temperature employed and the shuttered MME technique, which may allow Mg atoms to stick and more effectively incorporate under favorable surface chemistry to minimize compensating defects [182]. Although the growth substrate temperature is low, the metal adlayer in the MME technique enables large adatom diffusion lengths, and the films maintain smooth surface morphologies [123]. With this hydrogen-free technique and more traditional MBE, the Mg atoms are activated as-grown without an activation annealing step that is common for MOCVD growth of p-GaN [77]. The MOCVD annealing step is required to allow for hydrogen out-diffusion from the material and is difficult for buried p-type layers unless they are of a suitably small geometry to allow for lateral diffusion out from the sidewalls [168]. The low-temperature MME growth technique enables high hole concentrations as well as device design flexibility with buried p-type layers as-grown, without an anneal.

7.2 Results and Discussion

7.2.1 Single Phase Metal Modulated Epitaxy of AlGaN Films

The MME growth technique can be employed to form single-phase AlGaN films for all Al contents from 0 to 100% as long as the metal dose on the surface is precisely controlled and limited to prevent phase separation. With excessive amounts of Al and Ga

metal on the surface, the film tends to form initially Al-rich then Ga-rich layers upon consumption with the nitrogen plasma, instead of the desired uniform composition [183], [184]. Two $Al_{0.55}Ga_{0.45}N$ films were grown with different metal shutter open times of 14 s and 2.5 s to demonstrate the effects of a large and small metal dose of Al and Ga. Figure 7.1 displays the x-ray diffraction (0002) 2θ-ω scans of both samples. As seen in Figure 7.1(a), the long shutter open time causes phase separation in the growth direction, and a superlattice-like periodic stack of Al-rich and Ga-rich sublayers that form during each MME shutter cycle. The smaller metal dose displayed in Figure 7.1(b) results in a single-phase $Al_xGa_{1-x}N$ peak.

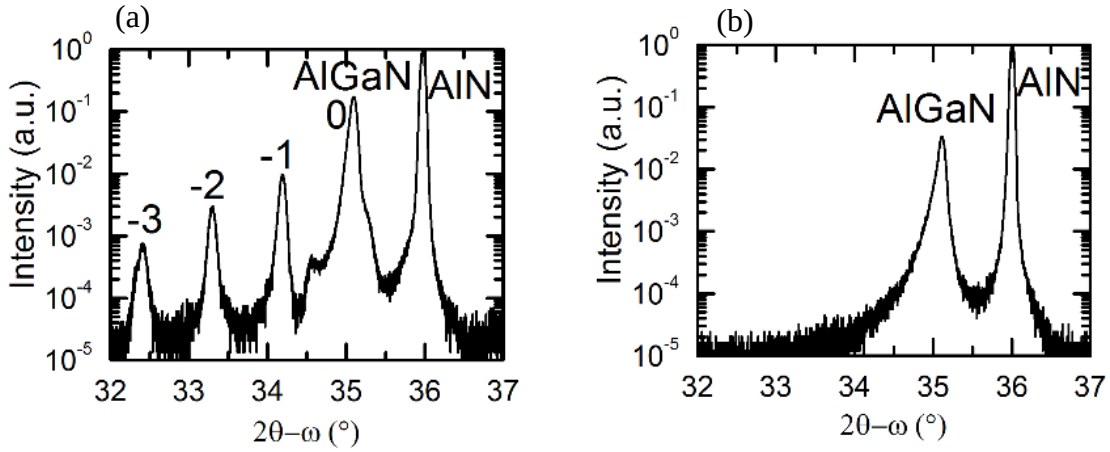

Figure 7.1. X-ray diffraction (0002) 2θ-ω scans of two $Al_xGa_{1-x}N$ films for x = 0.5 and different metal shutter open times of (a) 14 s and (b) 2.5 s

The periodic superlattice structure in Figure 7.1(a) is further analyzed. The measured data agrees with a simulated structure that consists of a 7.7 nm thick 69% Al AlGaN layer, followed by a 2.5 nm thick 10% Al AlGaN layer. The total amount of Al is still ~55%, but it mainly incorporates in the first layer. The total thickness for the pair is

10.2 nm, which closely agrees with the expected ~10.4 nm thickness from growth rate calculations where one superlattice pair is grown each MME cycle. The film with the superlattice was measured in TEM, and is shown in Figure 7.2. The superlattice is clearly observed in TEM and this measurement is in agreement with the XRD simulations, with a similar periodicity of ~11 nm.

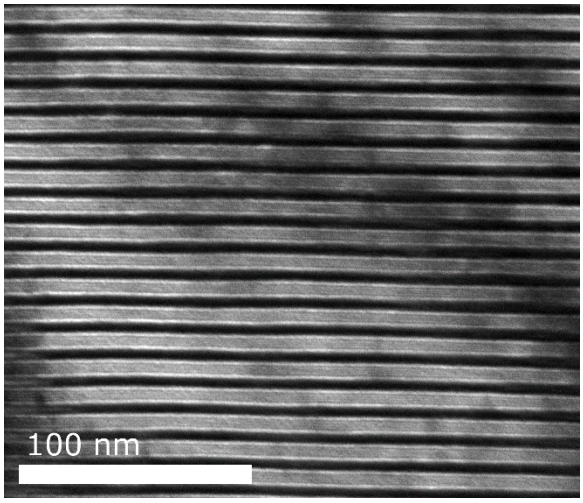

Figure 7.2. TEM image of the superlattice structure for an MME-grown AlGaN film with a large metal dose.

7.2.2 Extreme Doping of Various Al Content AlGaN Films

In order to explore the effect of increasing Al content on the resistivity and electron concentration of the n- and p-AlGaN films, three 100 nm-thick n-type and three p-type AlGaN calibration samples were grown with Al compositions up to ~60% via MME on AlN buffer layers grown on AlN templates (threading dislocation density ~2×10^{9} cm^{-3} obtained from the Sandia National Laboratories, NM, USA) at growth temperatures between 680-720 °C (depending on the Al composition).

The n-AlGaN films were grown with a silicon flux ([Si] = 1.9×10^{20} cm^{-3} for GaN calibrations). Figure 7.3 illustrates that with increasing Al composition, the Van-der Pauw resistivity increases by a factor of 83 from 3.5×10^{-4} to 2.9×10^{-2} Ω-cm, while the Hall electron concentration only decreases by a factor of 4.8 from 1.8×10^{20} to 3.8×10^{19} cm^{-3}. The reduction in electron concentration is likely due to the increase in the dopant activation energy [137]. The mismatch in the rate of increasing resistivity with the rate of decreasing electron concentration is the result of elevated alloy disorder scattering or defect scattering for higher Al content films.

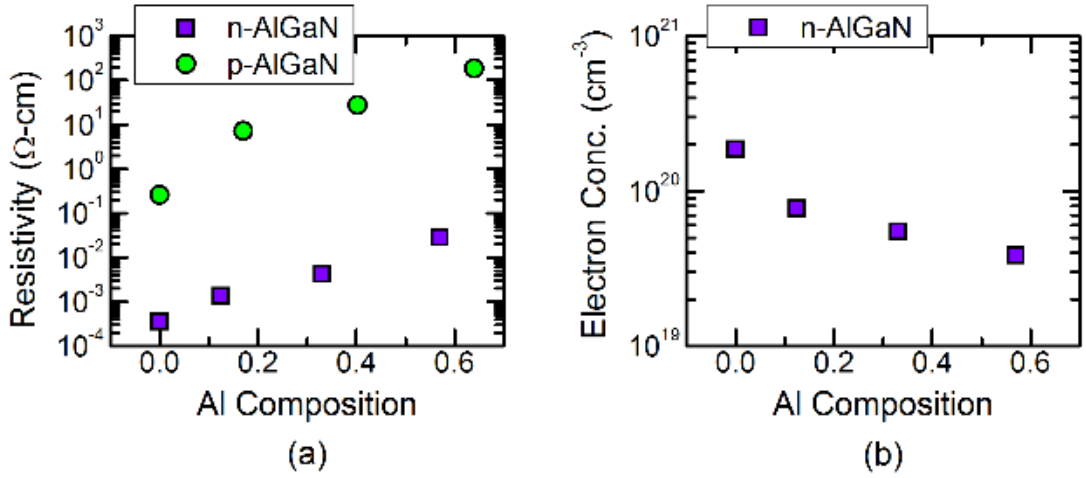

Figure 7.3. Effect of Al composition on (a) Van-der Pauw resistivity of n- and p-AlGaN films and (b) Hall electron concentration of n-AlGaN films (p-AlGaN hole concentrations were unmeasurable for the Hall effect with a fixed magnet of 0.3 T but clearly showed p-type conduction in thermal probe measurements).

The p-AlGaN films were grown with a constant flux of magnesium ([Mg] = 5.3×10^{20} cm^{-3} for GaN). The room-temperature Hall hole concentrations were not compared for the p-AlGaN films because they were unmeasurable with the Hall effect due to a low strength fixed magnet of 0.3 T, but clearly showed p-type conduction in thermal probe

measurements. Given p-GaN films with this excessively high doping are already near the lower limit of Hall mobility measurement capability, it is not surprising the heavily doped random alloy is unmeasurable. As seen in Figure 7.3(a), the p-type films exhibit a large (~730x) increase in the Van-der Pauw resistivity from 2.6×10^{-1} Ω-cm for p-GaN to 1.9×10^{2} Ω-cm for p-$Al_{0.64}Ga_{0.36}N$. The resistivity of the n- and p-AlGaN films with high Al compositions resulted in higher resistances and reduced doping concentrations, which will increase the depletion widths for AlGaN TJs and significantly decrease the tunneling probability.

7.2.3 Low Al Content AlGaN Homojunction Tunnel Diode

Next, a first attempt at a low Al content $Al_xGa_{1-x}N$ homojunction tunnel diode was grown on a GaN template with x = 0.08. The low Al content x = 0.08 was chosen to limit the drop off in doping concentration that is demonstrated at higher Al contents, and thus, similar results to the GaN tunnel diode devices are expected. The device structure, X-ray diffraction (XRD) $(10\bar{1}5)$ reciprocal space map (RSM), and current-voltage characteristics are shown in Figure 7.4. In Figure 7.4(a) the tunnel junction is formed at the p++/n++ interface, and the n-type contact was deposited on the n-$Al_{0.08}Ga_{0.92}N$ layer in order to limit conduction into the GaN template and better represent a true homojunction device. The RSM in Figure 7.4(b) displays the asymmetric $Al_{0.08}Ga_{0.92}N$ film is coherently strained to the GaN template and the $Al_{0.08}Ga_{0.92}N$ film does not exhibit in-plane tensile relaxation. Due to the lack of strain relaxation, the measured (0002) and $(10\bar{1}5)$ omega rocking curve full-width at half-maximum (FWHM) values are low and 313 and 325 arcsec, respectively. The current-voltage characteristics of a device are shown in Figure 7.4(c) and exhibit

negative differential resistance, likely due to some sort of defect assisted tunneling between 2.5-2.7 V and a peak-to-valley current ratio (PVCR) of ~1.06. Reverse-bias tunneling is also observed, i.e. -47 A/cm^2 at -1 V compared to 23 A/cm^2 at +1 V. Both forward and reverse-bias tunneling is achieved in an $Al_xGa_{1-x}N$ homojunction device as a result of the low-temperature heavily doped MME growth technique.

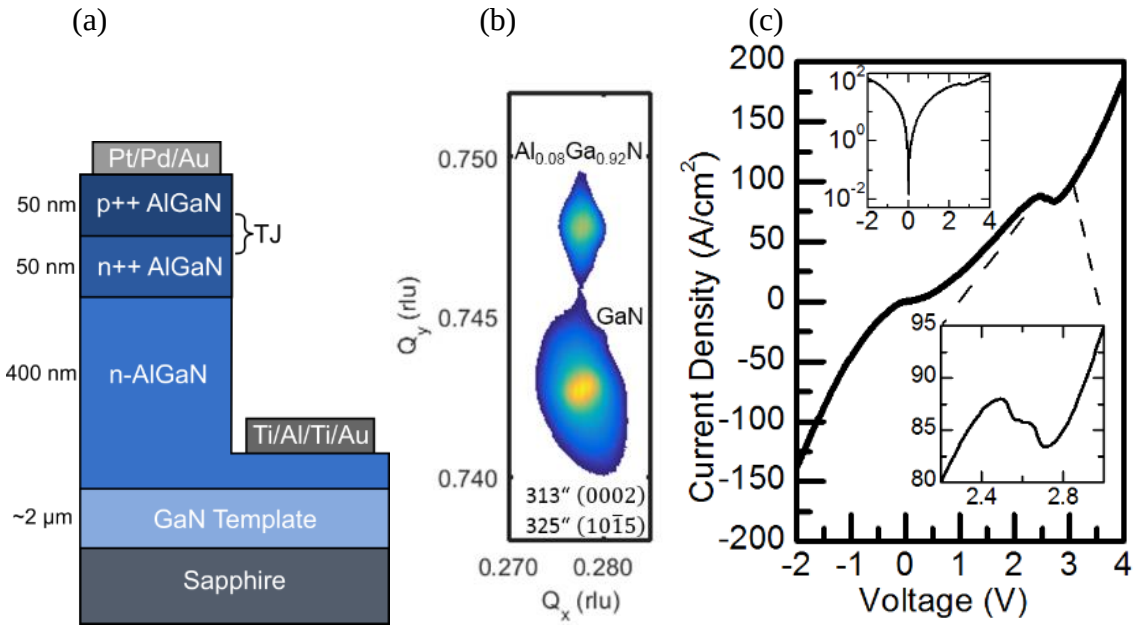

Figure 7.4. $Al_{0.08}Ga_{0.92}N$ tunnel diode (a) device structure (b) XRD (10$\bar{1}$5) RSM exhibiting the $Al_{0.08}Ga_{0.92}N$ film is coherently strained to the GaN substrate and (c) current-voltage characteristics of a 300 um circular mesa device (Inset: (top) semilog current-voltage characteristic and (bottom) negative differential resistance regime)

Temperature-dependent current-voltage measurements were taken on a similar device on the same $Al_{0.08}Ga_{0.92}N$ tunnel diode sample, and are shown in Figure 7.5. Remarkably, the NDR is still present even down to 85 K, further indicating that a tunneling mechanism is present. At low temperatures (< 131 K), the device seems to have a higher resistance which shifts the NDR voltage to higher values, which is likely due to carrier

freezout, and possibly higher contact resistances. At higher temperatures (> 309 K), it appears that the current contribution from thermionic emission shifts to lower voltages, and starts to overlap with the current contribution from tunneling, until NDR is no longer observable at high temperatures.

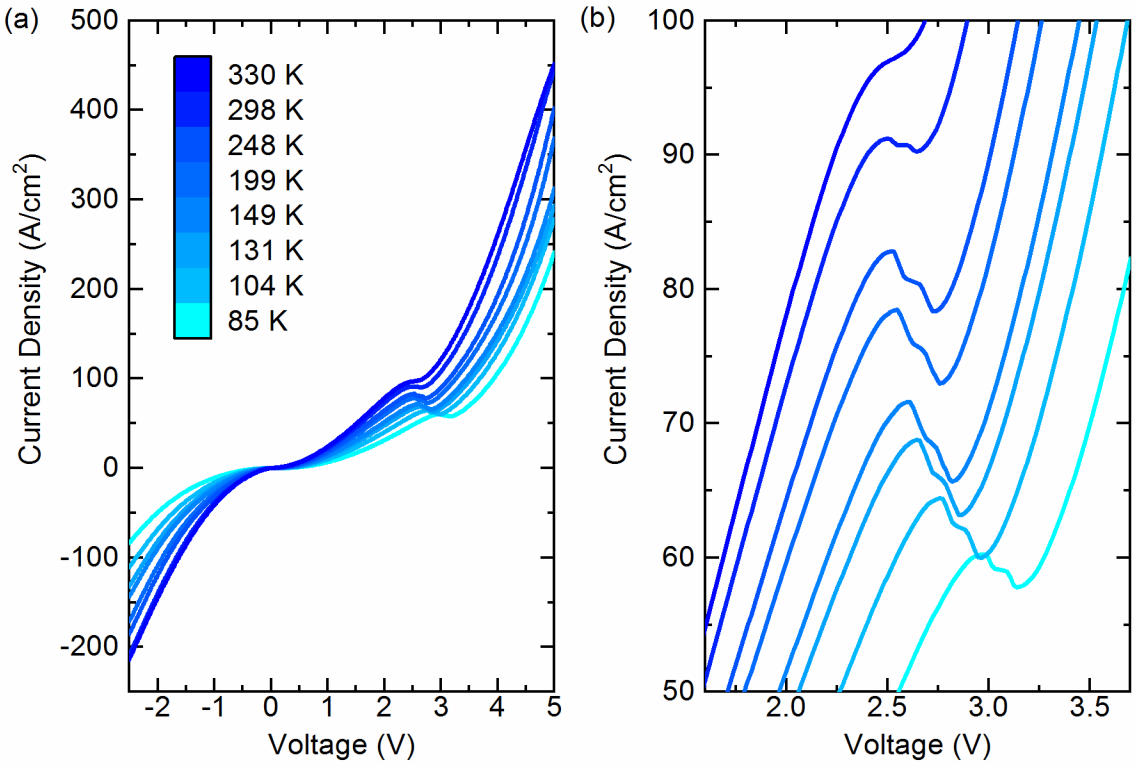

Figure 7.5. Temperature dependent current-voltage characteristics for (a) a wide range of voltages and (b) the negative differential resistance regime

The NDR peak-to-valley current ratio (PVCR) and the voltage range of the NDR regime are extracted for a wide range of temperatures from 85 to 309 K. The PVCR increases as the device is cooled, and reaches a maximum value of ~1.09 at 146 K. Below 146 K the PVCR begins to decrease again, likely due to carrier freezout which lowers the carrier concentrations, increases the depletion width, and thus reduce the probability of any

tunneling current. Interestingly, the NDR voltage range remains somewhat constant at 0.22 V between 146 and 235 K.

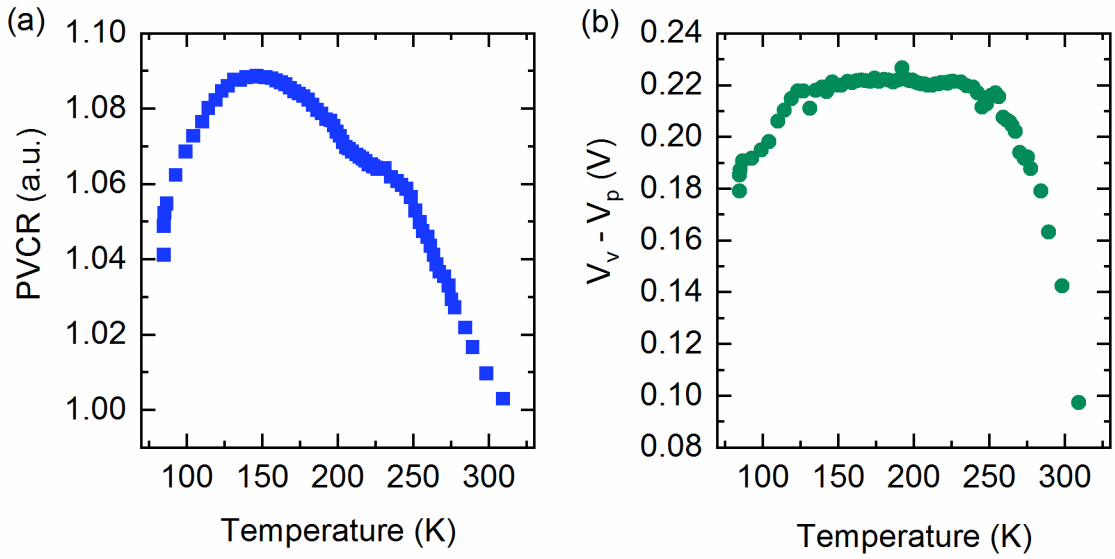

Figure 7.6. Temperature-dependent negative differential resistance (a) peak-to-valley current ratio (PVCR) and (b) voltage range.

7.2.4 Fabrication and Characterization of AlGaN Homojunction Tunnel Diodes

In order to investigate tunneling in higher Al content AlGaN devices, three heavily doped p++/n++/n AlGaN homojunction TDs (B1, B2, and B3) were grown at Al compositions of ~19, 42, and 58%, respectively, and are shown in Figure 7.7(b). Since increased conduction can be attributed to either fundamental tunneling mechanisms or merely leakage current, three AlGaN p++/i/n control diodes (A1-A3) were grown at similar Al contents and are compared to the p++/n++/n TDs and are shown in Figure 7.7(a). The depletion widths in the control diodes with the 50 nm intrinsic layers are sufficiently wide

to prevent tunneling, while the heavy doping in structure B significantly decreases the depletion widths to promote tunneling.

Growths for both structure A and B were initiated by 100 nm of unintentionally doped AlN buffer layers on AlN templates. An AlN template was chosen to electrically isolate the template from the homojunction devices, and to ensure the films are either relaxed or compressively strained to prevent material degradation or cracking. The 130 nm lower n- and 50 nm top p-type layer dopant concentrations in both structures were [Si] = 1.9×10^{20} cm^{-3} and [Mg] = 5.3×10^{20} cm^{-3}, respectively. These dopant concentrations are the same as those used in the calibration samples, shown in Figure 7.3, but with slightly different Al compositions of 19, 42, and 58%, which are within the calibrated range. Structure B contains an additional heavily doped n-type layer (instead of the i-layer in Structure A) with a concentration of [Si] = 4.60×10^{20} cm^{-3} to form a TJ at the p++/n++ interface.

The growth temperature was changed depending on the Al composition. The growth temperature was set to 680, 700, and 720 °C for the Al compositions of 19, 42, and 58%, respectively. Atomic force microscopy (not shown here) confirmed a two-dimensional growth mode was maintained and demonstrated RMS roughness values of ~1-2 nm.

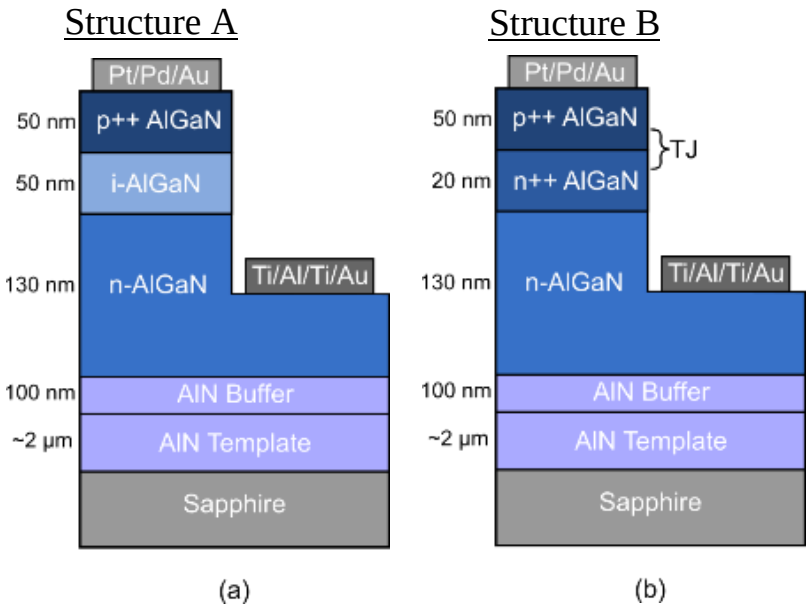

Figure 7.7. AlGaN homojunction device structures for (a) p++/i/n (structure A) and (b) p++/n++/n (structure B) devices.

Samples A1-A3 and B1-B3 shown in Figure 7.7 were fabricated into 200 µm circular mesa devices using standard photolithography and an inductively coupled plasma (ICP) etching procedure with BCl_3 and Cl_2 gases to define the mesa structure. A metal stack of Ti(300 Å)/Al(1000 Å)/Ti(300 Å)/Au(500 Å) and Pt(50 Å)/Pd(50 Å)/Au(500 Å) was deposited using e-beam evaporation for n- and p-type contacts, respectively. The contacts were not annealed in this study, because the heavily Mg-doped layers behave differently when annealed [185]. These results are similar to our previous work with GaN, where the heavy doping and activated, as-grown n- and p-type layers enabled Ohmic conduction [175].

The semi-log current-voltage characteristics for A1-A3 and B1-B3 are presented in Figure 7.8. Device B1, shown in Figure 7.8(a), exhibits NDR in forward bias with a low peak-to-valley current ratio (PVCR) of ~1.003 at a peak voltage of 2.35 V, slightly lower than those of previously reported in homojunction GaN TDs (PVCR of 1.01 to 1.1) [160],

[175]. The ideality factor (*n*) for B1 is much greater than two, which is common in nitride-based devices, especially those grown on inexpensive sapphire substrates. Homoepitaxially grown GaN devices on bulk GaN substrates with low dislocation densities have been demonstrated to achieve record low n = 1.1 [186]. The high peak voltage and ideality factor n >> 2 further suggests a defect-assisted tunneling mechanism and not Esaki-style band-to-band tunneling. For band-to-band tunneling in forward bias the peak voltage is related to the degenerate doping on both sides of the junction and would take place at low voltages (*e.g.*, < 0.4 V) [95].

Samples B1-B3 display asymmetric current density profiles. The current densities of samples B1-B3 at -1.0 V is 118, 68, and 49% higher than those at 1.0 V. The increased conductivity in reverse bias indicates tunneling via a narrowed depletion width, and the tunneling reduces with increasing Al content, as previously discussed due to the wider depletion widths resulting from lower dopant concentrations at elevated Al content. The control diodes A1-A3 do not exhibit tunneling, as expected. Diodes A1-A3 current-voltage characteristics represent more traditional rectification, but they do have higher than predicted reverse-bias leakage currents, especially for A1 and A2, likely due to thin intrinsic layers and the presence of defects in the heteroepitaxial growth performed here (see later discussion). When comparing the current densities at a reverse bias of -4.0 V of the control devices to the tunnel devices, both the lowest and highest Al content pairs of samples (A1 to B1 in Figure 7.8(a), and A3 to B3 in Figure 7.8(c)) exhibit an increase of almost four orders of magnitude indicating tunnel conduction is indeed the responsible mechanism, not merely leakage current. Thus, by separating the n++ and p++ regions by 50 nm, which is beyond the tunneling length, tunneling is suppressed in the control

structure. Additionally, each pair of structures (*e.g.*, A1 and B1) has a similar current density at higher forward biases when thermionic emission begins to dominate, and tunneling is negligible.

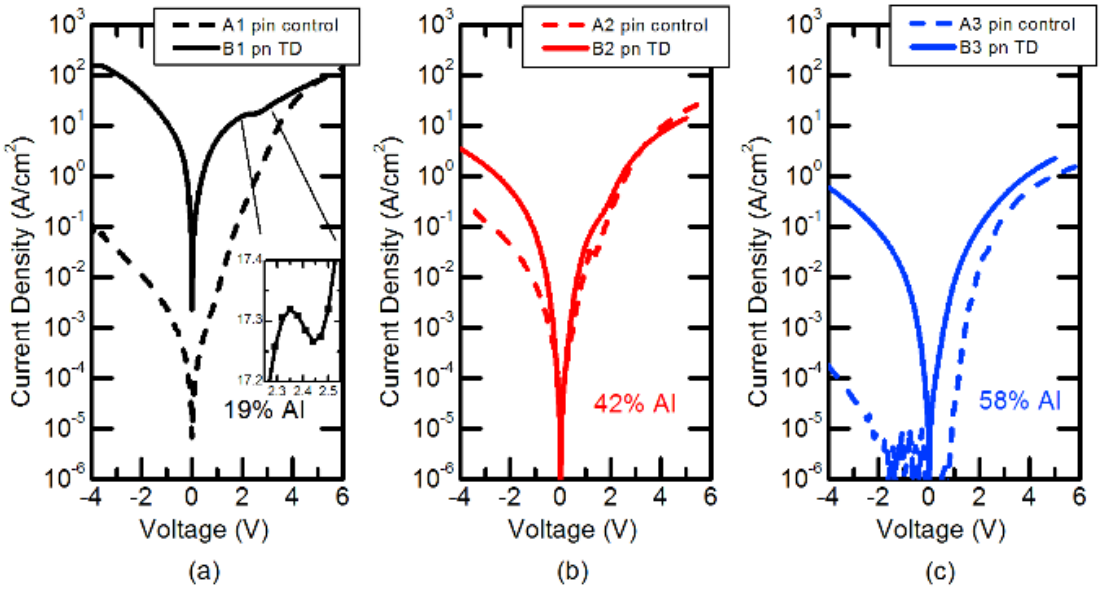

Figure 7.8. Semi-log current-voltage characteristics for p++/i/n control and p++/n++ tunnel diode devices (a) A1and B1 (inset: linear NDR for B1), (b) A2 and B2, and (c) A3 and B3. Negative differential resistance is present in sample B1. High reverse bias conductivities are observed for B1-B3 when compared to their control diodes A1-A3.

In order to verify that tunneling was not a result of poor structural quality (e.g., phase separation, pits, cracking), the samples B1-B3 were measured via x-ray diffraction (XRD), atomic force microscopy (AFM), and scanning transmission electron microscopy (STEM) techniques.

The XRD asymmetric $(10\bar{1}5)$ reciprocal space maps (RSMs) are displayed in Figure 7.9. The films are single composition and partially relaxed. The films may have an initial thin layer that is more strained to the template, and once the critical thickness is exceeded, a more relaxed layer forms, similar to $In_xGa_{1-x}N$/GaN films [49], [51], [187].

The films' $(10\bar{1}5)$ omega rocking curve FWHM values increase from 842 to 1459" for B1 to B3, while the (0002) FWHM decreases from 634 to 487". The trend of FWHM values indicates that at higher Al content, the films are slightly more columnar, similar to previous findings for GaN [188]. This columnar effect may be mitigated in the future with a more optimized MME condition and thicker buffer layers.

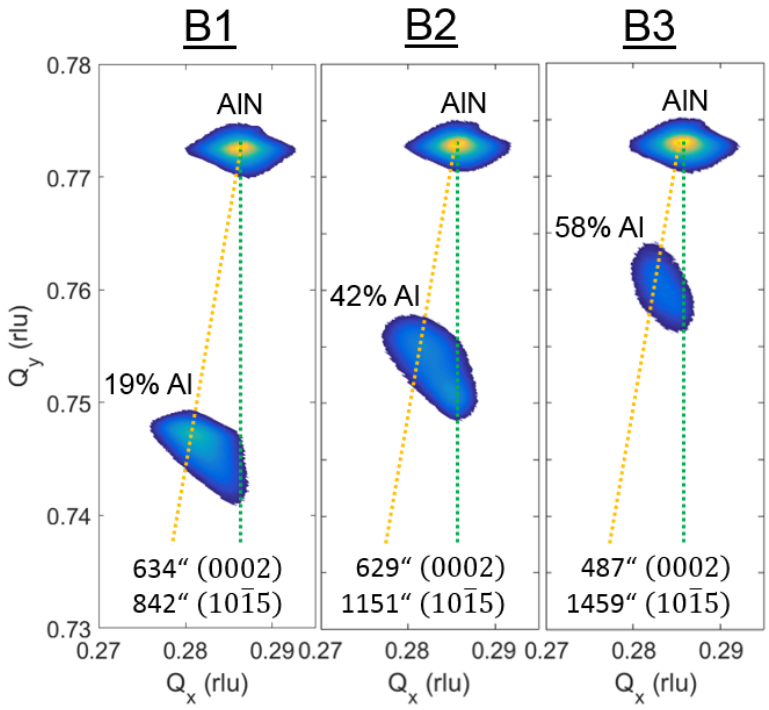

Figure 7.9. XRD $(10\bar{1}5)$ RSMs for samples B1-B3. The AlN template location, the $Al_xGa_{1-x}N$ film location and associated Al content, and the measured (0002) and $(10\bar{1}5)$ FWHM values are all labeled. The vertical (green) and diagonal (orange) dashed lines correspond to the fully-strained and full-relaxed film positioned, respectively.

Atomic force microscopy (AFM) 5 x 5 μm^2 scans are taken of the top p++ surfaces for the p++/n++/n $Al_xGa_{1-x}N$ tunnel junction samples B1-B3 and are shown in Figure 7.10. The RMS roughness values of the three samples are 1.43, 1.91, and 2.07 nm for B1-B3, respectively. It is speculated that there are two main roughening mechanisms that result in

samples B1-B3 surface morphologies and XRD results: lattice mismatch and low adatom mobility from low temperature growth. First, a smaller lattice mismatch between the 3.111 Å a-spacing of the AlN substrate and the film should result in a smoother film. Thus, the higher Al content films should exhibit less lattice-mismatch induced roughening. XRD RSM data indicate the Al content of the $Al_xGa_{1-x}N$ film in samples B1-B3 would result in a relaxed a-spacing of 3.174, 3.155, and 3.144 Å corresponding to a lattice mismatch of ~1.95, 1.37, and 1.01 % from the AlN substrate, respectively. In addition to the lattice-mismatch contribution to the morphology, adatom diffusion lengths during growth also contribute strongly to the AFM morphology. As previously mentioned, samples B1-B3 were grown well below conventional $Al_xGa_{1-x}N$ substrate growth temperatures, and in this study at 680, 700, and 720 °C, respectively. The low-temperatures were chosen to allow for the extreme p-type doping required for the tunnel junction devices. When growing binary III-nitrides via MME, increasing the metal dose or adlayer can enhance the adatom diffusion lengths, but for non-binaries such as $Al_xGa_{1-x}N$, the metal adlayer is limited (unless the growth rate is increased) to prevent alloy inhomogeneity as previously discussed. Thus, the low adatom diffusion lengths may generate increased roughness at higher Al contents due to the low substrate growth temperatures utilized to increase Mg incorporation.

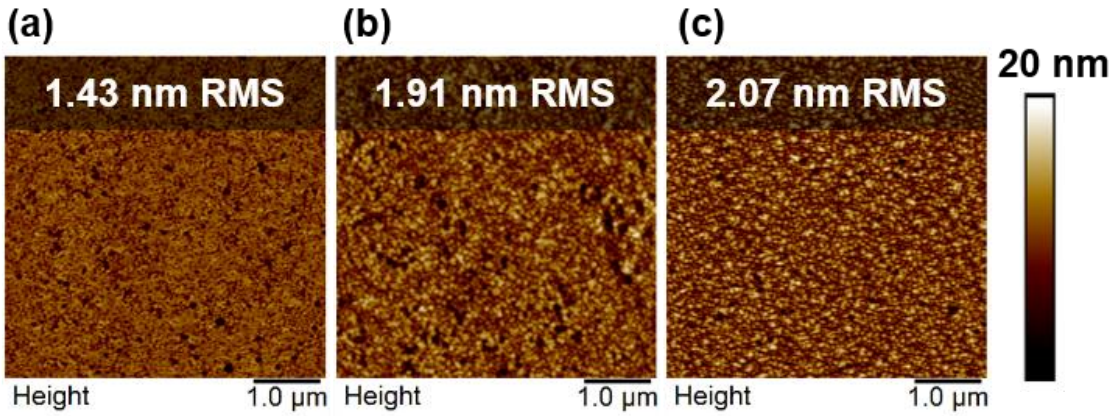

Figure 7.10. AFM 5 x 5 μm^2 scans of top p++ $Al_xGa_{1-x}N$ surfaces for (a) B1, (b) B2, and (c) B3. The cold growths cause some roughening but it is limited due to the metal adlayer in the MME growth technique.

STEM images of sample B1 were taken using a JEOL ARM200F operated at 200 keV, and are displayed in Figure 7.11. The entire structure is shown in Figure 7.11(a). It is well known that AlN surfaces contain adsorbed oxygen that is notoriously difficult to remove. It appears that the un-optimized nucleation of the MME AlN buffer layer on the AlN template contains many defects (*e.g.,* oxygen) that generate dislocations which propagate through the buffer and into the AlGaN layers, a well-known issue.[189] Figure 5(b) is a high-resolution image at the TJ p++/n++ interface representing the overall images found for this device. Figure 5(b) does not indicate Mg precipitates or visible defects related to the extreme doping, but they may still be present in other regions of the device not imaged. Due to the lack of extended defects associated with doping, point defects which cannot be observed with STEM are likely the source of the defect-assisted tunneling.

The ability to heavily dope AlGaN layers while allowing high-quality subsequent epitaxy is promising for devices with buried TJs, such as series-connected LEDs, or tunnel-contacted p-down structures but will require a process for sufficient removal of oxygen

contamination from the AlN templates.

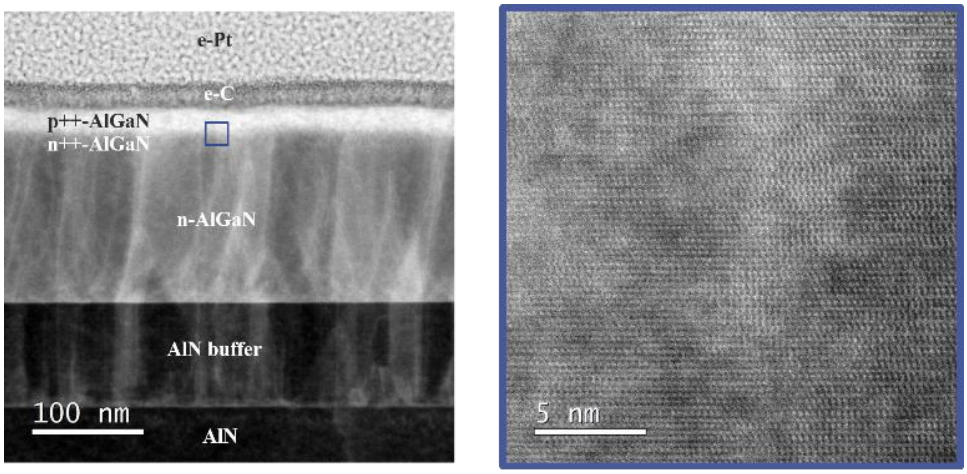

Figure 7.11. Scanning transmission electron microscopy of sample B1: (a) entire structure and (b) the p++/n++ TJ interface (the highlighted region in (a)) shows no significant structural degradation.

7.3 Conclusions

In conclusion, the low-temperature MME growth technique is employed to achieve single-phase, heavily doped AlGaN layers. The doping is progressively more difficult at high Al compositions, where the activation efficiency of dopants reduces and where the low-temperature growth technique is less optimal, and defect formation occurs. However, AlGaN homojunction TDs have been fabricated and are compared to control diodes to investigate the Al compositional limits of tunneling. Forward bias NDR is observed up to $x = 0.19$, indicating a narrow depletion width, and thus extreme dopant concentrations. Reverse bias tunneling is observed for all devices up to 58% Al, but the magnitude of the

tunneling current decreases with increasing Al content. The low-temperature MME growth technique presented here and applied to AlGaN TJs enables alternatives to unfavorable p-GaN layers and may enable future improved hole injection and power efficiency for deep UV emitters.

CHAPTER 8: ULTRA-WIDE-BANDGAP AlGaN TUNNEL CONTACTS FOR ULTRAVIOLET APPLICATIONS

8.1 Introduction

Ultra-wide-bandgap AlGaN tunnel junctions are promising for next generation ultraviolet optoelectronics as previously discussed in chapter 7. Tunneling in these devices is demonstrated in the previous chapters via reverse bias current-voltage measurements, and in some cases, forward bias negative differential resistance. Although these demonstrations with standalone AlGaN homojunction tunnel diodes exhibit clear tunneling, utilizing the tunnel junctions in other devices is necessary to determine their viability for next generation optoelectronics.

Ultra-wide-bandgap tunnel contacts are especially promising for light emitters because the tunnel contacts absorb less of the escaping light that was generated in the active region. Furthermore, transparent n-type AlGaN tunnel contacts to p-type AlGaN layers may improve light extraction efficiency and the external quantum efficiency (EQE) by avoiding the requirement for p-GaN layers which are traditionally inserted to enable ohmic contacts and provide holes to the low hole concentration AlGaN. Additionally, tunnel contacts can improve hole injection, and thus internal quantum efficiency (IQE) of the emitter by better balancing electron and hole concentrations and possibly eliminating the need for an electron blocking layer.

As shown in the previous chapter, tunneling in forward bias is limited at high Al

compositions for standalone AlGaN homojunction tunnel diodes. Fortunately, tunnel-contacted devices utilize a tunnel junction in reverse bias when the critical p/n junction active region of the device is in forward bias. A reverse-biased tunnel junction is much more conductive when compared to forward bias because the depletion width narrows and the tunneling distance for carriers decreases, allowing carriers to have a much higher probability to tunnel.

In this chapter, n-type AlGaN tunnel contacts to p/i/n diodes are first explored to determine the electrical consequences of using an ultra-wide-bandgap tunnel contact. Next, the tunnel contacts are utilized in a hybrid fashion atop MOCVD-grown UV LEDs. Neither structure is optimized, but both provide initial insights into the tradeoffs tunnel contacts provide in these wavelength ranges. These tradeoffs primarily involve minimizing the added electrical power to drive a tunnel-contacted device, while maximizing the added optical output power, in an effort to improve the efficiency of UV and DUV light emitters.

8.2 Results and Discussion

8.2.1 AlGaN Heterojunction Tunnel Contacts to GaN p/i/n Diodes

Four tunnel contacted samples R540 to R543 were grown to determine the effect of increasing Al content on the tunnel contact performance. The samples consist of 140 nm of n-type AlGaN tunnel contacts on top of p/i/n GaN diodes, as shown in Figure 8.1. The AlGaN layer thicknesses were limited, since they are under tensile strain when grown on GaN, and if grown too thick can result in cracking. The n-type tunnel contact varies in Al

content from 0% (GaN) to 63% Al, and the substrate growth temperature was increased from 600 °C for GaN up to 700 °C for the highest Al content of 63%. The Al and Ga metal on the surface were limited during the MME cycling to prevent the superlattice-type structure shown in Figure 7.1. Although other groups have described some of the benefits of a superlattice structure, such as activating holes and annihilating threading dislocations, it was avoided in this application because it can limit vertical conductivity.

As the Al content in the devices increases, the electron concentration in the tunnel contact will decrease, as seen in the previous chapter's Figure 7.3. The reduced electron concentration and higher bandgap with increasing Al content will increase the tunneling distance for carriers, and make the tunnel junction require more voltage to drive the same current through the GaN p/i/n diode.

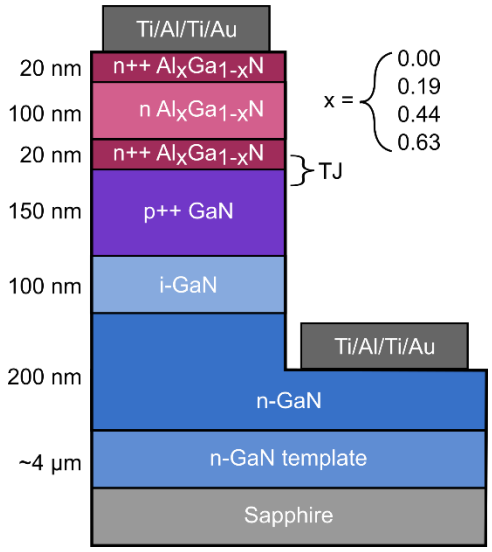

Figure 8.1. Device structure of n-type AlGaN tunnel contacts to underlying GaN p/i/n diodes. The Al composition in the tunnel contact varies from 0 (GaN) to 63 % AlGaN.

The samples were measured via X-ray diffraction to determine the structural quality of the AlGaN layers. The 2theta-omega scans of the three samples R541, R542, and R543 with Al tunnel contacts are displayed in Figure 8.2. The measurements indicate that each AlGaN layer is single composition. The peak intensity of the AlGaN layers decreases as the Al content is increased. The reduction in the diffraction intensity may be due to the low substrate growth temperature for these layers. The low substrate temperature may cause increased roughening and tilt which reduces the symmetric diffraction intensity. The low growth substrate temperature was chosen to prevent any Ga desorption from the surface of the films. It may be possible to improve the quality of these AlGaN/GaN films by further optimizing the growth substrate temperature and MME conditions for each Al composition while still achieving high n-type doping and single composition layers. Conversely, if some form of trap-assisted tunneling is the main contributor to conduction in these AlGaN TCs, then there may be a benefit to a defective AlGaN layer up to a certain defect density that increases the overall device efficiency.

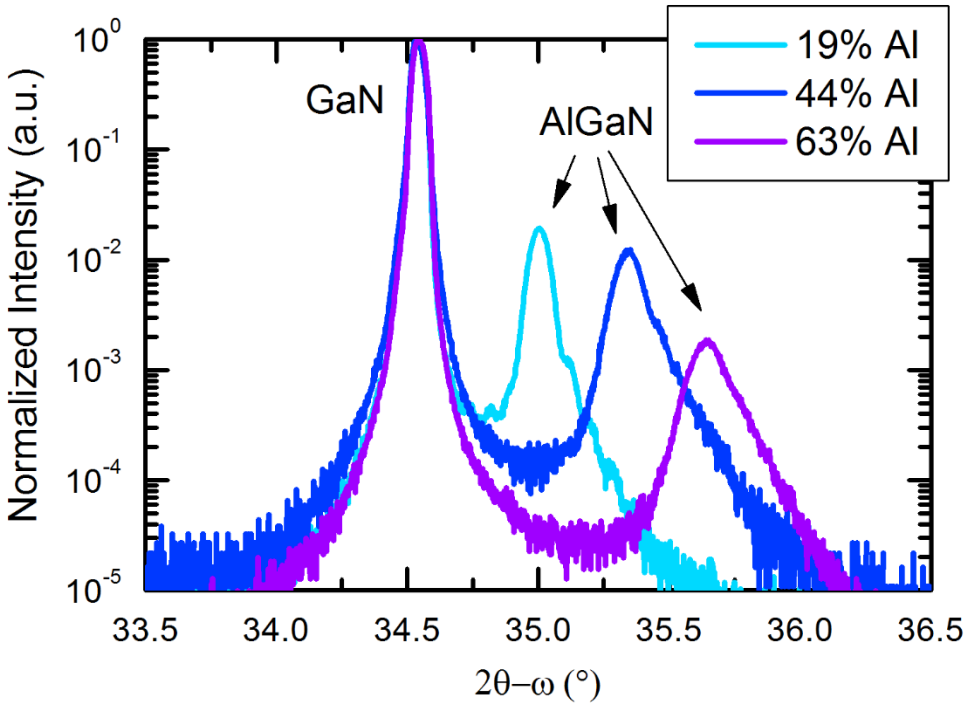

Figure 8.2. X-ray diffraction 2theta-omega scans of n-AlGaN tunnel contacts to GaN p/i/n diodes. Each AlGaN layer is single composition and the Al contents are 19%, 44%, and 63%.

$(10\bar{1}5)$ x-ray diffraction reciprocal space maps (RSMs) were taken for each AlGaN sample R541, R542, and R543. The RSM peaks are labelled and are shown in Figure 8.3. The large peaks are the GaN p/i/n diodes and underlying substrate of GaN, while the smaller peaks are the AlGaN layers. The two highest Al content AlGaN peaks (R542 and R543) demonstrate some iso-compositional elongation in their RSM, indicating some non-uniform strain.

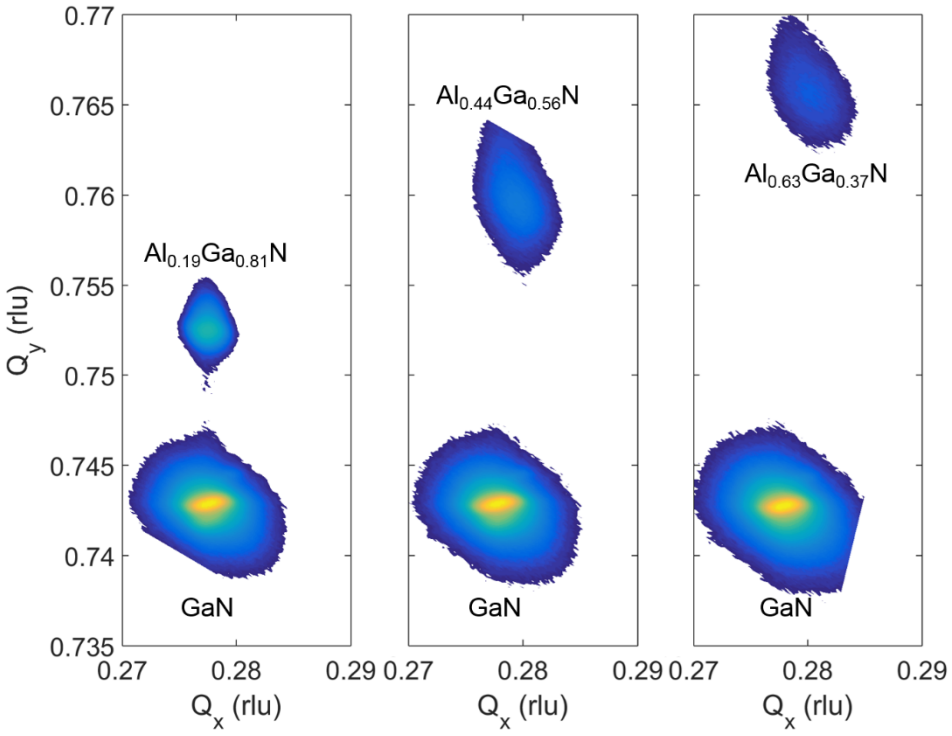

Figure 8.3. $(10\bar{1}5)$ x-ray diffraction reciprocal space maps (RSMs) of the n-type AlGaN tunnel contacts, samples R541, R542, and R543.

The lowest Al content film, R541, with 19% Al is coherently strained to the GaN substrate, as indicated by the vertical alignment of the AlGaN and GaN peaks in the RSM, and thus similar in-plane a-spacing. The RSM data can provide compositional data for the ternary, as well as information on how relaxed the film is relative to the substrate. Samples R541, R542, and R543 exhibit 0%, 39% and 48% relaxation, respectively. The RSM peak locations for the films are overlaid in Figure 8.4 to further illustrate the difference in relaxation for each film.

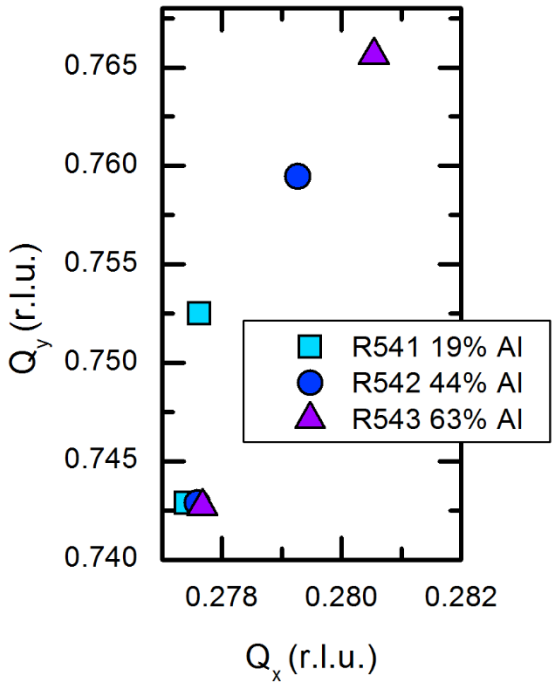

Figure 8.4. Overlay of the peak positions for AlGaN/GaN samples R541, R542, and R543. The 19% Al content film R541 is strained to the GaN substrate, while samples R542 and R543 exhibit partial relaxation.

The AlGaN films' structural quality was quantified by measuring the (0002) and $(10\bar{1}5)$ omega rocking curve full-widths at half maximum (FWHM). The FWHM values as well as the Al mole fraction and percent relaxation are detailed in Table 8.1. The samples' FWHM values indicate that at higher Al content, the structural quality of the AlGaN decreases. This trend is expected since the AlGaN layers are more lattice mismatched to the GaN substrate at higher Al contents, and the growth substrate temperature is low, which also degrades the film at higher Al contents. Interestingly, in Table 8.1 the $(10\bar{1}5)$ FWHM value is dramatically worse when comparing R541 and R542, indicating that when the film begins to relax, the film immediately becomes

defective, as expected.

Table 8.1. Summary of X-ray results for n-type AlGaN tunnel contacts to GaN p/i/n diodes. The structural quality of the AlGaN degrades as the Al content increases.

Sample ID	Al Mole Fraction x	AlGaN Relaxation (%)	AlGaN XRD (0002) FWHM (“)	AlGaN XRD ($10\bar{1}5$) FWHM (“)
R540	0.00	NA	NA	NA
R541	0.19	0	329	442
R542	0.44	39	466	1094
R543	0.63	48	967	1288

The band diagrams for the tunnel contacted devices at equilibrium are simulated using SiLENSe 3.42 software and are shown in Figure 8.5. The impurity concentrations, mobilities, and degree of relaxation inputs for the band diagrams are all determined from previous experimental data. The hole concentrations are greatly underestimated due to the software using a literature activation energy for Mg in GaN of 170 meV, while it is measured in chapter 3 to be < 16 meV for high hole concentration films. Figure 8.5b illustrates a closer view of the tunnel junction region, where the tunneling distance at zero bias increases with the increasing Al content in the tunnel contact. The tunnel junction depletion width widens, as expected, due to the lower doping concentration and wider bandgap as the Al composition is increased. Additionally, the depletion width shifts more towards the tunnel contact as the junction becomes more asymmetrically doped when the n-type AlGaN side of the junction reduces in doping and the p-type GaN remains heavily doped.

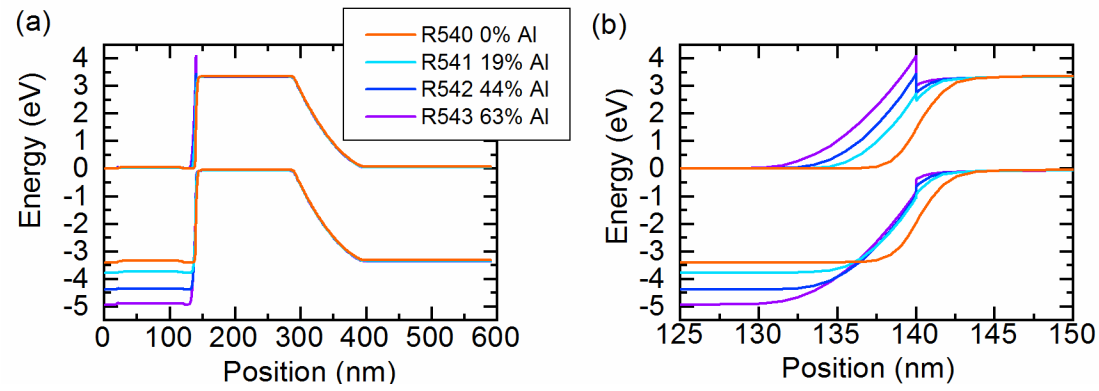

Figure 8.5. Band diagrams at equilibrium for the n-type AlGaN tunnel contacts to GaN p/i/n diodes (a) entire structure, and (b) tunnel junction region.

The samples were fabricated into 200 µm diameter circular mesa devices using standard lithography techniques for the group III-nitrides. Both top and bottom n-type metal electrodes of Ti/Al/Ti/Au were deposited at the same time since a modified tunnel contact mask was utilized, removing a second patterning and evaporation step and dramatically reducing the total fabrication time. The current-voltage characteristics of the devices are measured and displayed in Figure 8.6. The results are as expected, with an increasing turn-on voltage, and thus, higher voltage penalty for the higher Al content tunnel junctions due to their lower electron concentrations, wider depletion widths and lower tunneling probabilities.

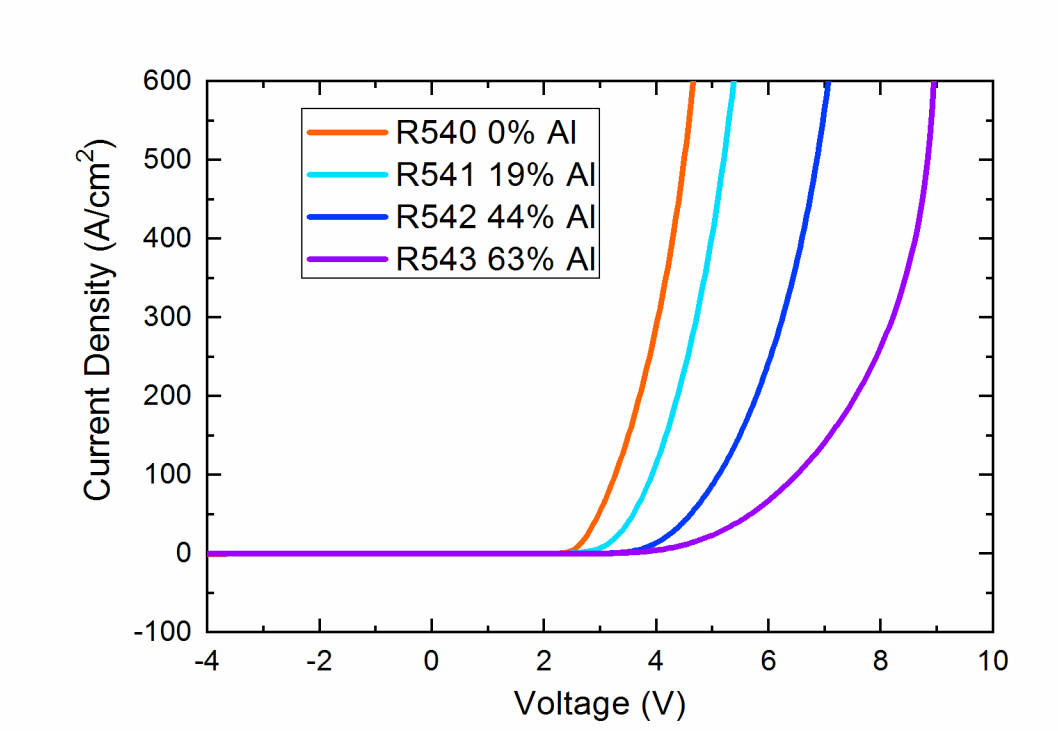

Figure 8.6. Current-voltage characteristics of the n-type AlGaN tunnel contacts to GaN p/i/n diodes. The voltage penalty of the tunnel contacts increases significantly with additional Al content in the tunnel junction.

In order to examine the voltage penalty, and thus the power loss associated with the tunnel contacts, the voltage at a current density of 600 A/cm^2 is plotted for each sample in Figure 8.7. The trend is clear and consistent with the voltage increasing exponentially with values of 4.6, 5.4, 7.1, and 8.9 V. Sample R543 only shows an added 4.3 V when utilizing a 63% Al tunnel contact in comparison to sample R540 with a GaN tunnel contact. An exponential fit line is plotted in Figure 8.7 as well with an R^2 value of 0.996. The fit line illustrates how the added voltage will trend with even higher Al content up to AlN in the tunnel contact. At high Al compositions the voltage penalty is significant, and thus additional techniques must be investigated to further decrease the power to turn on the tunnel contact. One promising technique for GaN tunnel contacts in chapter 5, but is not

explored here, is delta doping. Delta doping involves a high dose of dopant atoms right at the tunnel junction to assist any trap-assisted tunneling and minimize the depletion width as much as possible. Delta doping is demonstrated to lower the voltage penalty for GaN tunnel contacts, but will need to be further explored to examine its effects on light emitters, because the defects that assist tunneling may hinder light extraction.

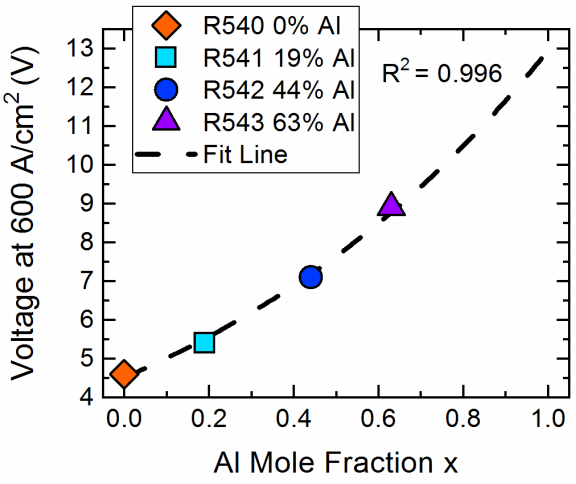

Figure 8.7. Voltage at 600 A/cm^2 for the four tunnel contacted devices vs. the Al mole fraction.

8.2.2 AlGaN Tunnel Contacts to Ultraviolet LEDs

MME-grown AlGaN tunnel contacts are formed atop MOCVD grown ultraviolet LEDs and compared to a more conventional p-type GaN contact layer. The two structures that were grown and fabricated are detailed in Figure 8.8. The device consists of an AlGaN/AlGaN MQW active area for UV light generation, an electron blocking layer (EBL), and an AlGaN grade from high Al content to lower Al content to better enable hole activation and injection from the p-GaN layer.

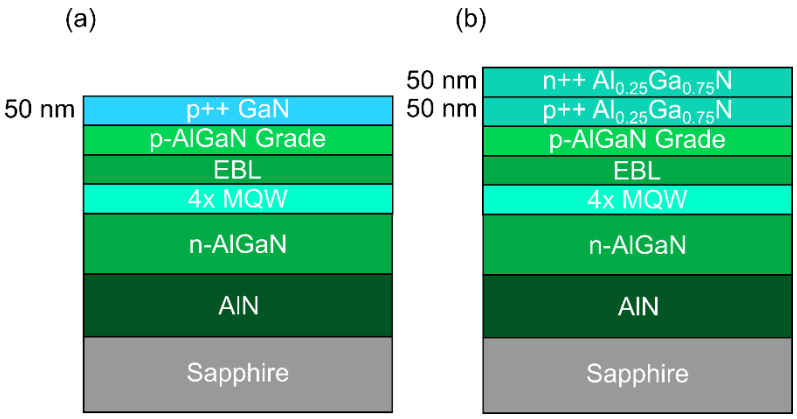

Figure 8.8. Ultraviolet LED structures with a (a) conventional p++ GaN top layer and (b) a p++/n++ $Al_{0.25}Ga_{0.75}N$ tunnel contact.

The two structures' current-voltage and light output power measurements are taken and displayed in Figure 8.9. Remarkably, the TC structure shows a > 2x higher light output power when driven at the same 7.5 mA current, and nearly the same input voltage. The tunnel contacts therefore are conductive enough to enable tunneling, while also being high enough Al content to minimize light absorption.

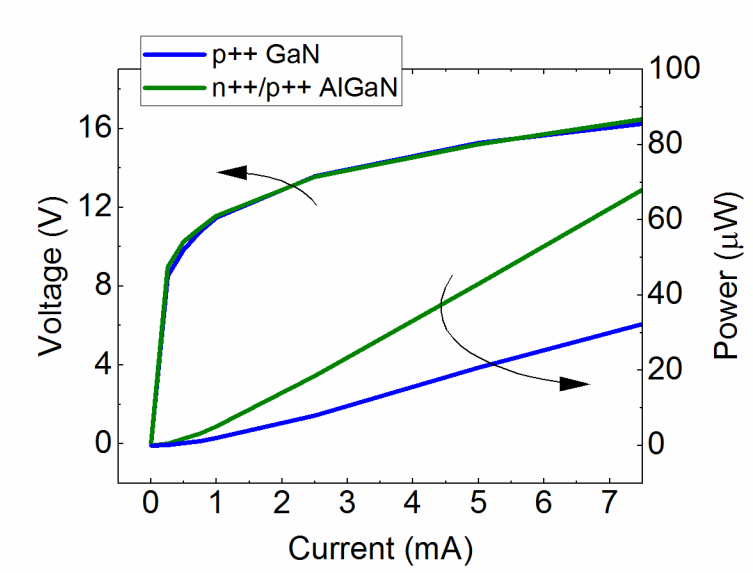

Figure 8.9. Current-voltage and light output power measurement for the conventional p++ GaN contact and a n++/p++ AlGaN TC UV LED.

The emission spectra for both UV LEDs is compared, and is shown in Figure 8.10 for a current injection of 10 mA for both devices, while the voltage is 16.1 and 15.3 for the p++ GaN and the n++/p++ AlGaN contacts, respectively. The conventional p++ GaN contact has a slightly deeper UV emission peak at 273 nm, while the n++/p++ AlGaN tunnel contact peak emission is centered at 276 nm, likely due to quantum well process variation unrelated to the contact technology explored here.

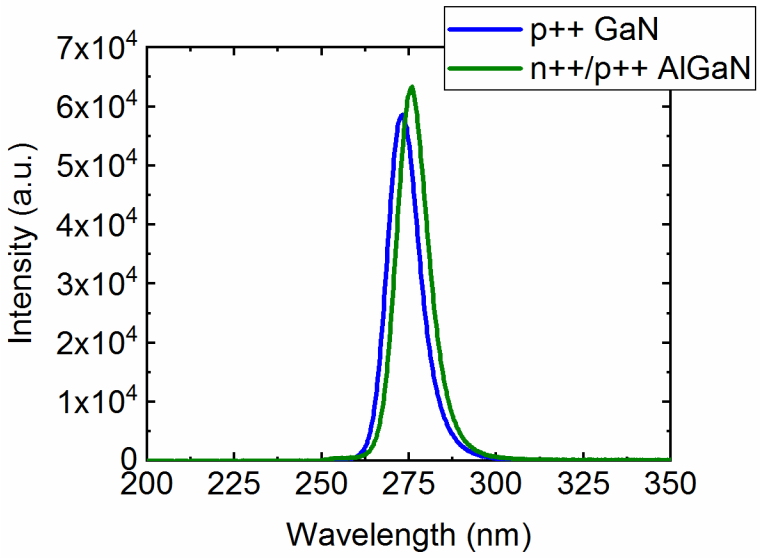

Figure 8.10. Emission spectra for both the conventional and AlGaN TC UV LED.

8.2.3 Conclusions

In conclusion, n-type AlGaN tunnel contacts are grown via MME atop GaN p/i/n diodes at Al contents of 0, 19, 44, and 63%. The AlGaN layers are single composition and their structural quality decreases with increasing Al content, due to low growth substrate temperatures and lattice mismatch. Partial relaxation in samples R542 and R543 with Al contents of 44 and 63%, respectively, generates additional defects. Band diagram simulations indicate longer tunneling distances as the Al is increased at the tunnel junction at equilibrium. The current-voltage characteristics demonstrate the higher Al content tunnel contacts require higher voltage drive to reach the same overall current densities for the devices. Finally, AlGaN tunnel contacts are compared to conventional p-type GaN contacts atop MOCVD-grown UV LEDs. The AlGaN tunnel contact exhibited >2x the light output power for the same input power. These results are promising for future UV

light emitters, but additional techniques should be investigated to reduce the voltage penalty further without dramatically hindering light extraction.

CHAPTER 9: SUMMARY AND FUTURE DIRECTIONS

In summary, a variety of materials and device improvements have been demonstrated, and the results are encouraging for future III-nitride optoelectronics. The plasma-assisted MBE technique can enable low temperature and high growth rate synthesis of high In content III-nitrides. The MME shuttering scheme and growth method is demonstrated to achieve state-of-the-art doping concentrations for both electrons and holes in GaN. The extreme doping and delta doping of GaN allows for homojunction tunnel diodes to be formed, which exhibit tunneling in forward and reverse bias. The GaN tunnel junctions can be utilized as tunnel contacts to improve the hole injection and contact resistance of top p-type layers. Hybrid MBE on MOCVD tunnel contacts are also demonstrated, but perform sub-optimally due to regrowth issues. The extreme doping is transitioned to MME-grown AlGaN tunnel junctions which also demonstrate forward bias tunneling up to 19% Al. Finally, n-type AlGaN tunnel contacts can tunnel inject holes into GaN devices, and even improve light output for a deep UV LED.

9.1 Plasma Optimization for High In Content III-Nitrides

Radio-frequency plasma-induced damage to III-nitride surfaces and bulk defects is observed and mitigated. High In-content and low bandgap materials are more sensitive to the plasma damage when compared to GaN. The plasma is characterized via optical emission spectroscopy and a Langmuir probe. By increasing the nitrogen flow from 2.5 to 7.5 sccm through the plasma bulb at a constant power of 350 W, the acceleration potential

drops by ~3.8 V which results in the background electron concentration for InN films to decrease by 74%, from 13.6 to 3.5 x 10^{18} cm^{-3}. InN grown at this high nitrogen flow results in a growth rate > 4μm/hr, which is the highest in the literature for InN. The high growth rate InN still exhibits excellent structural quality with a 0.9 nm RMS roughness measured in AFM, and with a < 200" (0002) and <350" $(10\bar{1}5)$ omega rocking curve FWHM measured in XRD, which are some of the lowest figures of merit in the literature. The photoluminescence spectra illustrate an improved InN crystal at the optimal plasma condition with a 100 meV shift closer to the fundamental bandgap.

9.2 MME Enabling Extreme Doping of GaN

The metal modulated epitaxy growth technique enables extremely high carrier concentrations in GaN. The optimal shuttering scheme for n-type doping involves high metal doses to promote smooth growth, while the optimal scheme for p-type doping limits the metal dose to limit nitrogen vacancies which can compensate the hole concentration. Heavy n-type doping with Ge and Si is achieved, with electron concentrations >1 x 10^{20} cm^{-3}, with the degenerate doping evident from > 100 meV Moss-Burstein shifts in the photoluminescence spectra. The highest Si-doped GaN film has the highest reported electron concentration of 3.1 x 10^{20} cm^{-3} without cracking. Since the refractive index changes at these high carrier concentrations, these heavily doped layers can form epitaxial distributed Bragg reflectors, but require many pairs (> 40) to have high reflectivity (> 90%). P-type doping via MME is capable of forming p-type layers with a wide range of hole concentrations from 7.0 x 10^{17} to the highest reported value of 1.5 x 10^{20} cm^{-3}. The effective activation energy significantly decreases from 149 to 16 meV when increasing the hole concentration from 7.1 x 10^{17} cm^{-3} to 2.7 x 10^{19} cm^{-3}. Furthermore, the carrier

freezeout is limited at high hole concentrations, indicating that an impurity band is likely forming.

9.3 GaN Tunnel Diodes and Tunnel Contacts

The methods resulting in the extreme doping of GaN are implemented into heavily doped tunnel junctions in standalone tunnel diodes as well as tunnel contacts to other devices. The tunnel diodes exhibit negative differential resistance in forward bias at the lowest reported ~1.35 V peak voltage. The results reported here are the second observation of NDR for a GaN homojunction tunnel diode, and the first time on a low-cost substrate of sapphire. Depending on the doping concentrations, the NDR can persist, or drift away after cycling, likely indicating some form of trap-assisted tunneling. The NDR is still present in the tunnel diode cooled down to 77 K, verifying a tunneling mechanism and that a p-type impurity band is likely present. Increasing the doping further with higher Mg concentrations or delta doping creates even more conductive tunnel junctions. The tunnel junctions are studied with STEM and indicate that they do not inhibit subsequent epitaxy. Tunnel contacted all-MBE grown p/i/n diodes show a low 0.14 V penalty when compared to a control device, which is the lowest reported voltage penalty in the literature. The series resistance of the best tunnel-contacted device is notably 13% lower than the control device that incorporates a p-type contact metallization. Hybrid MBE on MOCVD tunnel contacts are demonstrated for both a solar cell and an LED. The tunnel contacted solar cell demonstrates that the highly conductive tunnel junctions can operate in forward bias, which is the first demonstration of a photovoltaic response from a tunnel-contacted III-nitride solar cell. The best tunnel contacted solar cell employs a tunnel junction that is away from the regrowth interface, and the total cell efficiency improves by 47%, but is still 27% worse

than the control sample, due to a reduced carrier extraction. The hybrid tunnel contacted LED sample shows similar results to the solar cell, with the best tunnel contact still having a voltage penalty when compared to the control sample with ITO. The conductive n-type tunnel contact does exhibit built-in current spreading, which is convenient for light emitters and any series connected optoelectronics.

9.4 AlGaN Tunnel Diodes and Tunnel Contacts

The MME technique and conditions for extreme doping are transitioned to AlGaN materials. The ternary material must be grown with lower metal doses to prevent a superlattice from forming. The doping concentrations fall off exponentially when increasing the Al content. NDR is observed for the first time in an AlGaN tunnel diode. An initial attempt tunnel diode with 9% Al displays NDR at room temperature and at 77 K. This first attempt is the first ever AlGaN homojunction tunnel diode with NDR. The peak-to-valley current ratio reaches 1.09 at 150 K, and is reduced at colder temperatures from carrier freezeout, and also at hotter temperatures from the shifting onset of thermionic emission. Tunnel diodes on AlN substrates are also grown and fabricated at various Al contents from 19 to 58%. The STEM images indicate that the regrowth of AlN on the AlN substrate is not optimal, and generates dislocations. The 19% Al tunnel diode exhibits NDR in forward and reverse bias, which is the highest Al content tunnel diode in the literature with NDR. The 58% Al tunnel diode does not show forward bias tunneling, but does show reverse bias tunneling. N-type AlGaN tunnel contacts are formed on GaN p/i/n devices to examine the voltage penalty for just the n-type layer. The voltage penalty increases exponentially with Al content from 4.5 to 9 V at 600 A/cm^2 for 0 to 60% Al. Finally, a 276

nm tunnel-contacted LED is formed and displays >2x light output power when compared to a control.

9.5 Contributions

The work presented in this thesis resulted in the following accomplishments and contributions:

1. Identified that high-In content, low bandgap III-nitrides can be damaged in the plasma-assisted MBE technique [190].

2. Reduced plasma damage for InN, which resulted in the lowest ever reported InN (0002) FWHM of 167" [190].

3. Synthesized InN at a record-fast growth rate of 4.6 μm/hr [190].

4. Achieved degenerate n-type doping of GaN with both Si and Ge dopants via MME, and is evident in Moss-Burstein shifts in the PL spectra.

5. Record-high n-type doping of GaN with Si results in an electron concentration of 3.1×10^{20} cm^{-3} [175].

6. Record-high p-type doping of GaN with Mg results in a hole concentration of 1.5×10^{20} cm^{-3} [175].

7. Record-low effective activation energy of ~16 meV for Mg-doped GaN, indicating an impurity band forms at high doping.

8. First ever GaN homojunction tunnel diode with NDR grown on sapphire [175].

9. Lowest reported NDR peak voltage of 1.35 V for a GaN homojunction tunnel diode [175].

10. Identified tunneling in GaN tunnel junctions is likely trap-assisted, and not purely interband tunneling [175].

11. Record-low voltage penalty of 0.14 V for a tunnel-contacted III-nitride device [175].

12. Observed a 13% lower series resistance for an n-type tunnel contacted p/i/n diode in comparison to traditional p-type contacts [175].

13. First ever reported NDR in a GaN tunnel diode operating at 77 K [175].

14. First comparison of a GaN tunnel diode grown on sapphire vs. bulk GaN [191].

15. Identified excessive Mg doping eliminates the tunneling mechanism in GaN homojunction tunnel diodes.

16. Delta-doping of GaN homojunction tunnel diodes with Si or Mg can exhibit high conductivity and allow for subsequent epitaxy [191].

17. First demonstration of a tunnel-contacted III-nitride solar cell with a photovoltaic response [74].

18. Identified contamination at the regrowth interface as a potential source for high voltage penalties in hybrid MBE on MOCVD tunnel-contacted III-nitride

devices [191].

19. Determined that a hybrid tunnel junction is best formed away from the regrowth interface [74].

20. Demonstrated excellent current spreading is built-in for an n-type hybrid tunnel contact to a blue LED [191].

21. First demonstration of an AlGaN homojunction tunnel diode with NDR up to 19% Al AlGaN [192].

22. First observation of an AlGaN tunnel diode with NDR operating at a temperature of 80 K.

23. Highest reported Al content of 58% AlGaN for which reverse bias tunneling is observed in an AlGaN homojunction tunnel diode [192].

24. First demonstration of heterojunction n-AlGaN tunnel contacts to GaN devices to limit optical absorption.

25. Correlated voltage penalties with doping efficiency and bandgap of heterojunction n-AlGaN tunnel contacts to GaN devices.

9.6 Future Work

1. **Utilize plasma findings to form thick InGaN templates via MME.** The plasma findings suggest that high growth rate and high indium content III-

nitrides require a plasma to provide nitrogen species with a flux that is de-coupled from the growth substrate temperature, unlike other techniques that require thermal cracking. Synthesis at higher growth rates reduces the damage of the films per unit thickness, and the damage may be further reduced with alternative plasma designs, or a bias on the substrate to possibly deflect damaging particles. The MME technique can be utilized at high growth rates to form high indium content templates, possibly for hybrid growth of LEDs or other devices. These templates may provide relaxed compliant substrates for higher efficiency longer wavelength III-nitride emitters.

2. **Optimize tunnel contact doping for III-N emitters**. In this work GaN homojunction tunnel junctions were formed and were applied as tunnel contacts to all-MBE grown devices, and hybrid MBE-MOCVD devices. Although the extreme tunnel junction doping allowed low voltage penalties to drive the extra junction, the excessive doping may result in unwanted absorption due to a variety of reasons such as dopant related defects, and thus a reduction in the extraction efficiency of the device. Therefore, it is necessary to study the tunnel junction doping on the light extraction efficiency of an all-MBE LED. The optimal tunnel contact doping, thickness, and morphology may be unique for each specific optoelectronic device.
3. **Apply delta-doping to GaN and AlGaN emitters and solar cells.** Delta doping is studied in this work in a GaN standalone tunnel diode application, but is not implemented as a tunnel contact. The delta doping provides improvements in conductivity and permits subsequent epitaxy which will likely

result in ultra-low voltage penalties, but may generate additional defects that hinder emitter light extraction or unwanted recombination in a solar cell. Delta doping should be explored further, especially for AlGaN devices where the Mg doping activation efficiency is already limited at wide bandgaps and the voltage penalty for lightly doped AlGaN tunnel junctions is extremely high. Thus delta-doping AlGaN tunnel contacts may provide the ultimate solution to the detrimental p-GaN contact that is conventional for AlGaN devices to lower contact resistance and improve hole injection.

4. **Optimize UV-relevant AlGaN tunnel contacts.** AlGaN tunnel junctions are studied in this work to allow for UV-relevant tunnel contacts. The doping concentrations for both the n-type and especially the p-type side of the tunnel junction is reduced when increasing the Al content, and thus the voltage penalty for the junction increases dramatically. Thus, there is a tradeoff between reducing the tunnel contact UV light absorption by increasing the Al content in the AlGaN layers, and the additional voltage drive to power a higher Al content tunnel junction. Therefore, there likely exists an optimal Al content tunnel contact to maximize the power efficiency for a UV emitter.
5. **Develop a cap technology to transfer wafers between systems and provide an Epi-Ready wafer technology.** Hybrid MBE tunnel contacts are grown on MOCVD devices and are compared to all-MBE grown tunnel contacts and devices in this work. The all-MBE tunnel contacts have lower voltage penalties in comparison to the hybrid tunnel contacts, even when both sides of the tunnel junction are heavily doped via MME in an MBE system. The higher voltage

drive for the hybrid grown tunnel contact is likely due to some impurity contamination at the regrowth interface. Therefore, a cap technology should be investigated that is protective enough to grow III-N materials in one system and transfer in air to another system. An InN or InGaN cap may be capable of protecting the regrowth interface while easily removable via thermal decomposition and desorption.

APPENDIX A:

DATA FOR FURTHER EXPLORATION

InN Capping Towards an Epi-Ready Transfer Technology:

InN is a promising cap technology to enable transferring wafers between epitaxial growth systems without requiring significant cleaning. One can imagine a p-type GaN substrate grown in one MOCVD chamber with an InN cap, and then transferred to another MOCVD system where the cap is boiled off and followed by an *in-situ* anneal to activate the p-type layer. Finally the growth is continued to avoid the Mg memory effect. Furthermore, hybrid tunnel-contacted structures may greatly benefit from such a cap technology.

An InN capped structure was grown to test the ability to thermally decompose InN and desorb In to remove the cap. The 2theta-omega XRD diffractograms for (0002) InN capped and boiled off samples are shown in Figure A.1. The InN cap was thermally boiled off *in-situ* at ~650 °C.

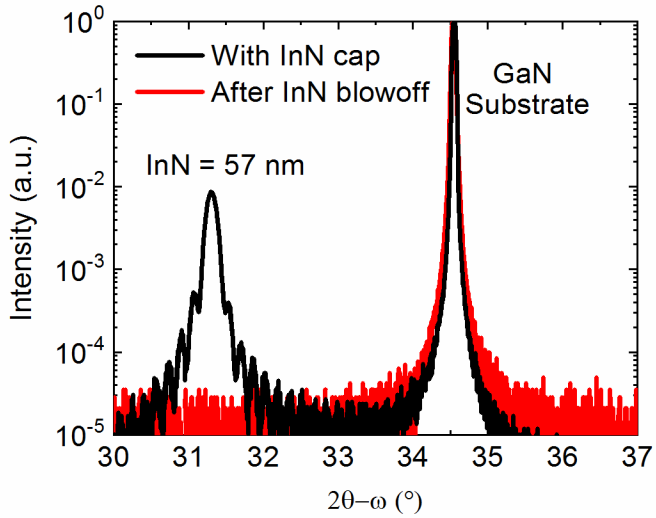

Figure A.1. XRD 2theta-omega for (0002) InN and GaN substrate. The InN layer is thermally boiled off at ~650 °C.

Next, different thicknesses of the cap were grown and boiled off. The RHEED intensity transients are displayed in Figure A.2. Four thicknesses were selected between ~5 and 56 nm. The RHEED intensity for each transient decreases as metal In accumulates on the surface when InN is decomposed. The RHEED intensity begins to rise again when the In metal on the surface begins to desorb, until the transient nearly flat lines when all the In is blown off and a GaN RHEED pattern remains.

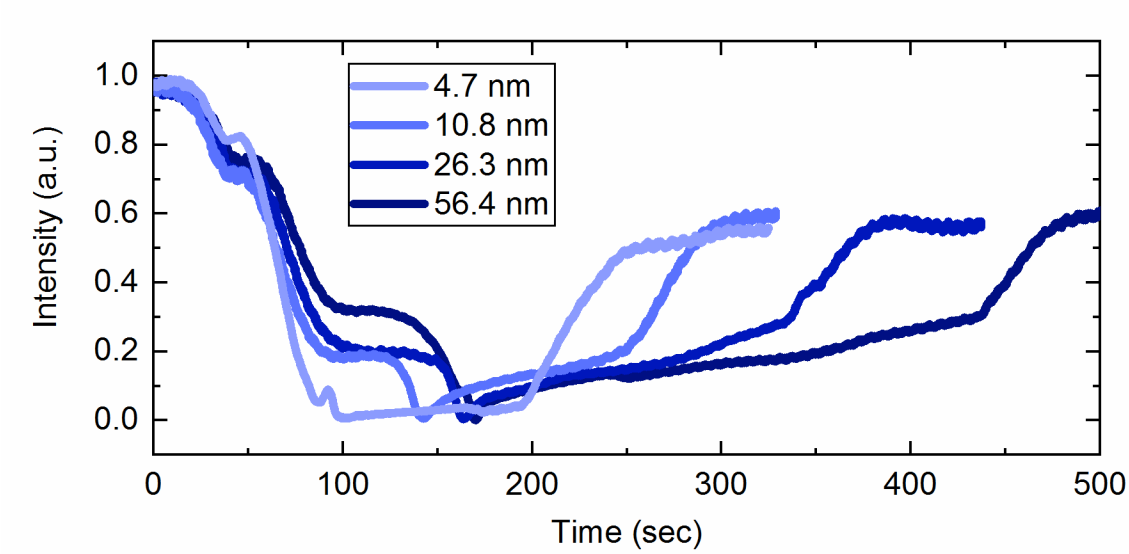

Figure A.2. RHEED intensity transients for InN layers being decomposed and In being desorbed from the surface.

The time to boil off each of these InN caps is then plotted in Figure A.3. Even the thickest InN cap of 56.4 nm is blown off somewhat quickly in about 8 minutes.

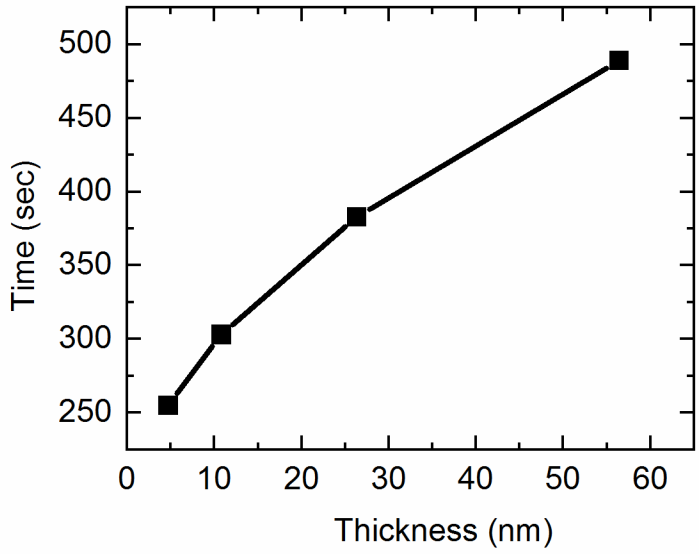

Figure A.3. Time to boil off each InN cap of varying thickness.

These results are promising because they demonstrate the feasibility of an epi-ready transfer technique. Further studies are required to ensure that the cap technology does indeed prevent contamination to the regrowth surfaces.

GaN Growth Rate Study:

High growth rates are pursued to lower device cost and enable thick buffer technologies. MME GaN is grown at four different growth rates from 1.75 to 3.5 μm/hr. This is achieved simply by increasing the nitrogen flow into the RF plasma, as well as raising the Ga cell temperature to increase its flux. The nitrogen flow rate vs growth rate is shown in Figure A.4. The high growth rate plasma bulb used in this work is clearly not saturating the growth rate at higher nitrogen flow.

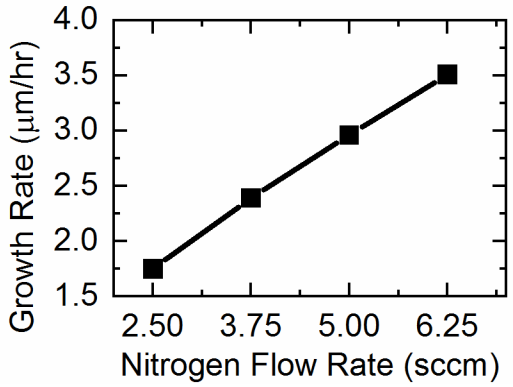

Figure A.4. GaN growth rate at different RF plasma nitrogen flows.

The XRD omega rocking curve FWHM values are measured for these growth rates for both the (0002) and the $(10\bar{1}5)$ planes. The results are displayed in Figure A.5. The results indicate that the higher growth rate films are of worse structural quality. This is likely due to the Ga cell flux not being uniform at these high temperatures and 'spitting' large clusters of Ga. Another possibility is that these growths were performed too cold (600 °C) for such high growth rates.

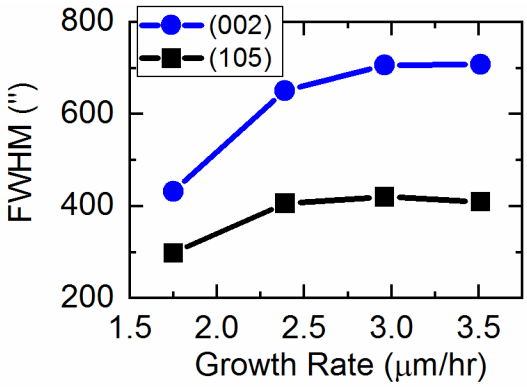

Figure A.5. XRD omega rocking curve FWHM values for both the (0002) and $(10\bar{1}5)$ planes of GaN grown at varying growth rates

To further study the structural quality of these films, thermal conductivity measurements and photoluminescence (PL) measurements were taken and are shown in Figure A.6. Notably, the thermal conductivity remains high at ~200 W/m-K for all the films. Similarly, the PL spectra are the same for all the films grown at various growth rates.

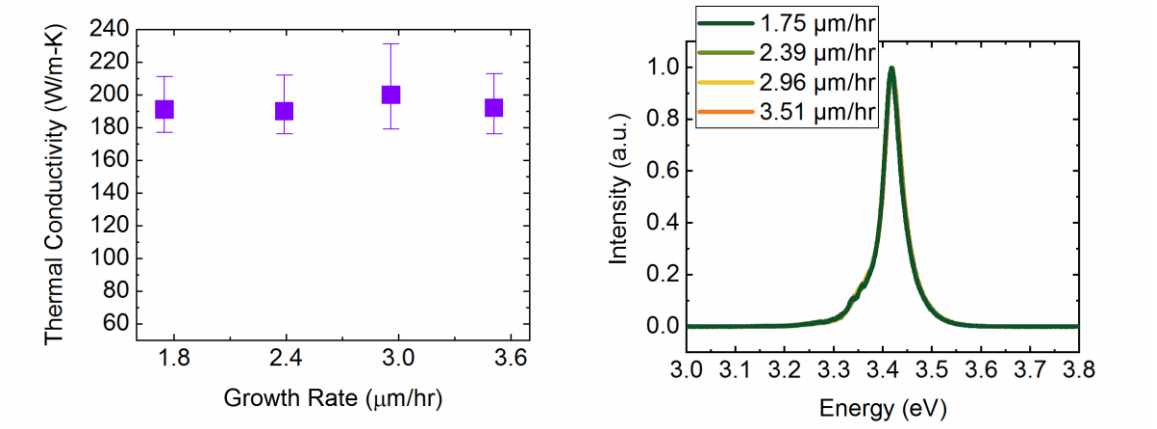

Figure A.6. GaN thermal conductivity (left) and photoluminescence spectra (right) for films grown at various growth rates.

These GaN growth rate results are promising, but must be further explored to determine the reason for the XRD structural degradation at higher growth rates. TEM measurements of these films will be beneficial to this effort.

Observation of III/V Drift during MME Growth and Applying the MEE Technique for Flux Measurements:

MME is a shuttered growth technique that can be utilized *in-situ* to track the III/V ratio (for III/V > 1). It was observed that there can be some drift in the III/V ratio during MME growth if the Al cell temperature is unadjusted. The observed drift tends to reduce the III/V ratio, which either means the group-III metal flux from the cell is reducing, or the N flux is increasing. An example drift of the III/V ratio for MME grown AlN is shown in Figure A.7. Over the course of 30 minutes the III/V reduces from 2.30 to 2.05. Further studies need to be performed to determine the source of this drift and correct for it.

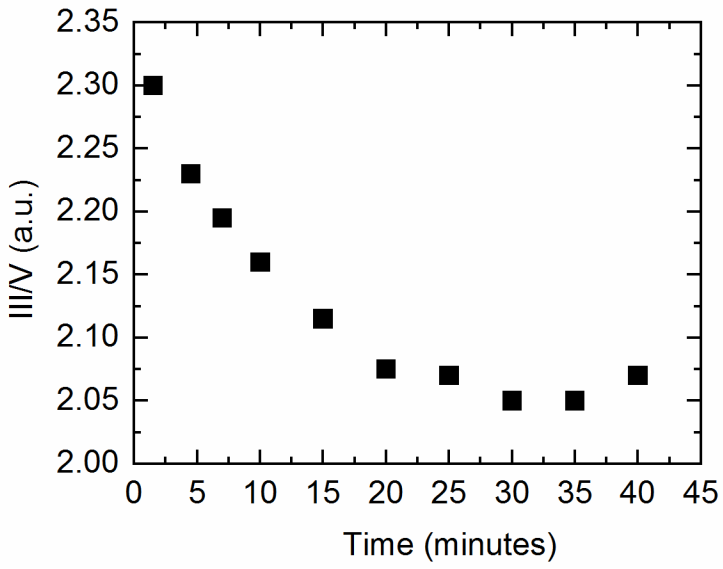

Figure A.7. III/V drift during MME of AlN.

Once the plasma condition stabilizes, III/V flux ratio measurements can be taken for a cell utilizing the metal enhanced epitaxy (MEE) technique in combination with RHEED. The MEE approach is also a shuttered growth technique, where the group-III source is opened and exposes metal to the substrate without the nitrogen plasma being exposed at the same time. Next, the metal shutter is closed and the nitrogen plasma consumes the metal on the surface. This technique can be used to calibrate a source cell by tracking RHEED intensity transients without requiring a flux gauge. By dividing the time depositing metal by the time required for the nitrogen flux to consume the metal dose, a III/V ratio can be determined. An example calibration for Al is shown in Figure A.8 where

an exponential fit line is drawn with an $R^2 = 0.996$.

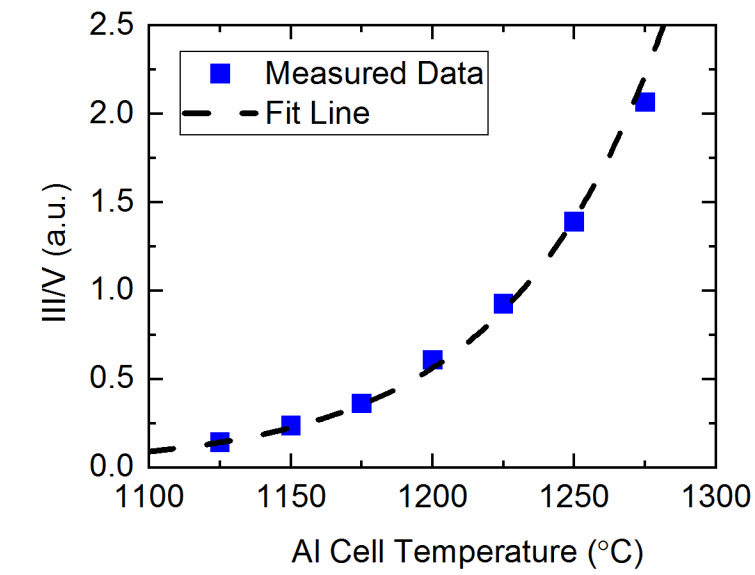

Figure A.8. Utilizing MEE for a flux calibration of an Al cell.

REFERENCES

[1] B. U. K. Mishra, L. Shen, T. E. Kazior, and Y. Wu, "GaN-Based RF Power Devices and Amplifiers," *Proc. IEEE*, vol. 96, no. 2, pp. 287–305, 2008.

[2] J. Wu, "When group-III nitrides go infrared: New properties and perspectives," *J. Appl. Phys.*, vol. 106, no. 1, p. 011101, Jul. 2009.

[3] N. S. Mansour, K. W. Kim, and M. A. Littlejohn, "Theoretical study of electron transport in gallium nitride," *J. Appl. Phys.*, vol. 77, no. 6, pp. 2834–2836, 1995.

[4] J. Kolník, I. H. Oğuzman, K. F. Brennan, R. Wang, P. P. Ruden, and Y. Wang, "Electronic transport studies of bulk zincblende and wurtzite phases of GaN based on an ensemble Monte Carlo calculation including a full zone band structure," *J. Appl. Phys.*, vol. 78, no. 2, pp. 1033–1038, 1995.

[5] F. A. Ponce and D. P. Bour, "Nitride Based Semiconductors for blue and green light-emitting devices," *Nature*, vol. 386, pp. 351–359, 1997.

[6] S. P. Denbaars *et al.*, "Development of gallium-nitride-based light-emitting diodes (LEDs) and laser diodes for energy-efficient lighting and displays," *Acta Mater.*, vol. 61, no. 3, pp. 945–951, 2013.

[7] J. Kim, "Growth and characterization of III-nitride semiconductors for high-efficient light-emitting diodes by metalorganic chemical vapor deposition," Georgia Institute of Technology, 2014.

[8] E. F. Schubert, *Light-Emitting Diodes*. Cambridge University Press, 2006.

[9] F. Rinaldi, "Basics of Molecular Beam Epitaxy (MBE)," 2003.

[10] J. R. Arthur, "Molecular beam epitaxy," *Surf. Sci.*, vol. 500, no. 1–3, pp. 189–217, Mar. 2002.

[11] C. Weisbuch, M. Piccardo, L. Martinelli, J. Iveland, J. Peretti, and J. S. Speck, "The efficiency challenge of nitride light-emitting diodes for lighting," *Phys. Status Solidi Appl. Mater. Sci.*, vol. 212, no. 5, pp. 899–913, 2015.

[12] C. J. Humphreys, "Solid-State Lighting," *MRS Bull.*, vol. 33, no. 4, pp. 459–471, 2008.

[13] L. Liu and J. H. Edgar, "Substrates for gallium nitride epitaxy," *Mater. Sci. Eng. R Reports*, vol. 37, no. 3, pp. 61–127, 2002.

[14] T. Paskova and K. R. Evans, "GaN Substrates — Progress , Status , and Prospects," *IEEE J. Sel. Top. Quantum eElectronics*, vol. 15, no. 4, pp. 1041–1052, 2009.

[15] M. Bockowski, M. Iwinska, M. Amilusik, M. Fijalkowski, B. Lucznik, and T. Sochacki, "Challenges and future perspectives in HVPE-GaN growth on ammonothermal GaN seeds," *Semicond. Sci. Technol.*, vol. 31, no. 9, 2016.

[16] E. Dirk *et al.*, "High Quality, Low Cost Ammonothermal Bulk GaN Substrates," *Jpn. J. Appl. Phys.*, vol. 52, no. 8S, p. 08JA01, 2013.

[17] X. H. Wu *et al.*, "Dislocation generation in GaN heteroepitaxy," *J. Cryst. Growth*, vol. 189–190, pp. 231–243, 1998.

[18] M. A. Moram *et al.*, "On the origin of threading dislocations in GaN films," *J. Appl. Phys.*, vol. 106, no. 7, p. 073513, Oct. 2009.

[19] D. F. Storm *et al.*, "Critical issues for homoepitaxial GaN growth by molecular beam epitaxy on hydride vapor-phase epitaxy-grown GaN substrates," *J. Cryst. Growth*, vol. 456, pp. 121–132, Dec. 2016.

[20] M. F. Schubert *et al.*, "Effect of dislocation density on efficiency droop in GaInNGaN light-emitting diodes," *Appl. Phys. Lett.*, vol. 91, no. 23, 2007.

[21] N. G. Young *et al.*, "High performance thin quantum barrier InGaN/GaN solar cells on sapphire and bulk (0001) GaN substrates," *Appl. Phys. Lett.*, vol. 103, no. 17, 2013.

[22] L. Sang, M. Liao, N. Ikeda, Y. Koide, and M. Sumiya, "Enhanced performance of InGaN solar cell by using a super-thin AlN interlayer," *Appl. Phys. Lett.*, vol. 99, no. 16, p. 161109, Oct. 2011.

[23] P. Kozodoy *et al.*, "Electrical characterization of GaN p-n junctions with and without threading dislocations," *Appl. Phys. Lett.*, vol. 73, no. 7, pp. 975–977, 1998.

[24] A. Dadgar, J. Bläsing, A. Diez, A. Alam, M. Heuken, and A. Krost, "Metalorganic Chemical Vapor Phase Epitaxy of Crack-Free GaN on Si (111) Exceeding 1 μm in Thickness," *Jpn. J. Appl. Phys.*, vol. 39, no. Part 2, No. 11B, pp. L1183–L1185, 2002.

[25] K. Hiramatsu, T. Detchprohm, and I. Akasaki, "Relaxation Mechanism Of Thermal Stresses In The Heterostructure Of Gan Grown On Sapphire By Vapor Phase Epitaxy," *Jpn. J. Appl. Phys.*, vol. 32, no. 4 R, pp. 1528–1533, 1993.

[26] J. O. Kim, S. K. Hong, and K. Y. Lim, "Crack formation in GaN on Si(111) substrates grown by MOCVD using HT Al-preseeding and HT AlN buffer layers," *Phys. Status Solidi Curr. Top. Solid State Phys.*, vol. 7, no. 7–8, pp. 2052–2055, 2010.

[27] D. A. Neumayer and J. G. Ekerdt, "Growth of group III nitrides. A review of precursors and techniques," *Chem. Mater.*, vol. 8, no. 1, pp. 9–25, 1996.

[28] J. Ma, X. Zhu, K. M. Wong, X. Zou, and K. M. Lau, "Improved GaN-based LED grown on silicon (111) substrates using stress/dislocation-engineered interlayers," *J. Cryst. Growth*, vol. 370, pp. 265–268, 2013.

[29] J. P. Zhang *et al.*, "Crack-free thick AlGaN grown on sapphire using AlN/AlGaN superlattices for strain management," *Appl. Phys. Lett.*, vol. 80, no. 19, pp. 3542–3544, 2002.

[30] X. H. Wu *et al.*, "Defect structure of metal-organic chemical vapor deposition-grown epitaxial (0001) GaN/Al2O3," *J. Appl. Phys.*, vol. 80, no. 6, pp. 3228–3237, 1996.

[31] P. Sheldon, K. M. Jones, M. M. Al-Jassim, and B. G. Yacobi, "Dislocation density reduction through annihilation in lattice-mismatched semiconductors grown by molecular-beam epitaxy," *J. Appl. Phys.*, vol. 63, no. 11, pp. 5609–5611, 1988.

[32] M. Tachikawa and M. Yamaguchi, "Film thickness dependence of dislocation density reduction in GaAs-on-Si substrates," *Appl. Phys. Lett.*, vol. 56, no. 5, pp. 484–486, 1990.

[33] B. P. Gunning, E. A. Clinton, J. J. Merola, W. A. Doolittle, and R. C. Bresnahan, "Control of ion content and nitrogen species using a mixed chemistry plasma for GaN grown at extremely high growth rates >9 μm/h by plasma-assisted molecular beam epitaxy," *J. Appl. Phys.*, vol. 118, no. 15, p. 155302, 2015.

[34] S. Y. Karpov, R. A. Talalaev, Y. N. Makarov, N. Grandjean, J. Massies, and B. Damilano, "Surface kinetics of GaN evaporation and growth by molecular-beam epitaxy," *Surf. Sci.*, vol. 450, no. 3, pp. 191–203, 2000.

[35] A. J. Ptak, M. R. Millecchia, T. H. Myers, K. S. Ziemer, and C. D. Stinespring, "The relation of active nitrogen species to high-temperature limitations for (0001) GaN growth by radio-frequency-plasma-assisted molecular beam epitaxy," *Appl. Phys. Lett.*, vol. 74, no. 25, pp. 3836–3838, 1999.

[36] M. Higashiwaki and T. Matsui, "High-quality InN film grown on a low-temperature-grown GaN intermediate layer by plasma-assisted molecular-beam epitaxy," *Japanese J. Appl. Physics, Part 2 Lett.*, vol. 41, no. 5 B, 2002.

[37] A. Knübel *et al.*, "Transport characteristics of indium nitride (InN) films grown by plasma assisted molecular beam epitaxy (PAMBE)," *Phys. Status Solidi Curr. Top. Solid State Phys.*, vol. 6, no. 6, pp. 1480–1483, 2009.

[38] E. Iliopoulos *et al.*, "InGaN(0001) alloys grown in the entire composition range by plasma assisted molecular beam epitaxy," *Phys. Status Solidi Appl. Mater. Sci.*, vol. 203, no. 1, pp. 102–105, 2006.

[39] T. Li *et al.*, "The effect of InGaN underlayers on the electronic and optical properties of InGaN/GaN quantum wells," *Appl. Phys. Lett.*, vol. 102, no. 4, pp. 1–5, 2013.

[40] T. Akasaka, H. Gotoh, T. Saito, and T. Makimoto, "High luminescent efficiency of InGaN multiple quantum wells grown on InGaN underlying layers," *Appl. Phys. Lett.*, vol. 85, no. 15, pp. 3089–3091, 2004.

[41] C. Haller, J. F. Carlin, G. Jacopin, D. Martin, R. Butté, and N. Grandjean, "Burying non-radiative defects in InGaN underlayer to increase InGaN/GaN quantum well efficiency," *Appl. Phys. Lett.*, vol. 111, no. 26, 2017.

[42] A. M. Armstrong, B. N. Bryant, M. H. Crawford, D. D. Koleske, S. R. Lee, and J. J. Wierer, "Defect-reduction mechanism for improving radiative efficiency in InGaN/GaN light-emitting diodes using InGaN underlayers," *J. Appl. Phys.*, vol. 117, no. 13, 2015.

[43] C. Haller *et al.*, "GaN surface as the source of non-radiative defects in InGaN/GaN quantum wells," *Appl. Phys. Lett.*, vol. 113, no. 11, 2018.

[44] M. T. Chu *et al.*, "Growth and characterization of p-InGaN/i-InGaN/n-GaN double-heterojunction solar cells on patterned sapphire substrates," *IEEE Electron Device Lett.*, vol. 32, no. 7, pp. 922–924, 2011.

[45] S. W. Feng, C. M. Lai, C. H. Chen, W. C. Sun, and L. W. Tu, "Theoretical simulations of the effects of the indium content, thickness, and defect density of the i-layer on the performance of p-i-n InGaN single homojunction solar cells," *J. Appl. Phys.*, vol. 108, no. 9, 2010.

[46] J. k. Sheu *et al.*, "White-Light Emission From Near UV InGaN-GaN LED Chip Precoated With Blue/Green/Red Phosphors," *IEEE Photonics Technol. Lett.*, vol. 15, no. 1, pp. 18–20, 2003.

[47] M. Bosi and R. Fornari, "A study of Indium incorporation efficiency in InGaN grown by MOVPE," *J. Cryst. Growth*, vol. 265, no. 3–4, pp. 434–439, 2004.

[48] M. Moseley, B. Gunning, J. Lowder, W. Alan Doolittle, and G. Namkoong, "Structural and electrical characterization of InN, InGaN, and p-InGaN grown by metal-modulated epitaxy," *J. Vac. Sci. Technol. B, Nanotechnol. Microelectron. Mater. Process. Meas. Phenom.*, vol. 31, no. 3, p. 03C104, May 2013.

[49] C. A. M. Fabien *et al.*, "Low-temperature growth of InGaN films over the entire composition range by MBE," *J. Cryst. Growth*, vol. 425, pp. 115–118, 2015.

[50] a. M. Fischer, Y. O. Wei, F. a. Ponce, M. Moseley, B. Gunning, and W. a. Doolittle, "Highly luminescent, high-indium-content InGaN film with uniform composition and full misfit-strain relaxation," *Appl. Phys. Lett.*, vol. 103, no. 13, p. 131101, 2013.

[51] E. A. Clinton *et al.*, "A review of the synthesis of reduced defect density InxGa1−xN for all indium compositions," *Solid. State. Electron.*, vol. 136, pp. 3–11, 2017.

[52] M. Moseley *et al.*, "Observation and control of the surface kinetics of InGaN for the

elimination of phase separation," *J. Appl. Phys.*, vol. 112, no. 1, p. 014909, 2012.

[53] M. Moseley, J. Lowder, D. Billingsley, and W. A. Doolittle, "Control of surface adatom kinetics for the growth of high-indium content InGaN throughout the miscibility gap," *Appl. Phys. Lett.*, vol. 97, no. 19, 2010.

[54] K. S. A. Butcher, D. Alexandrov, P. Terziyska, V. Georgiev, D. Georgieva, and P. W. Binsted, "InN grown by migration enhanced afterglow (MEAglow)," *Phys. Status Solidi Appl. Mater. Sci.*, vol. 209, no. 1, pp. 41–44, 2012.

[55] A. G. Bhuiyan, A. Hashimoto, and A. Yamamoto, "Indium nitride (InN): A review on growth, characterization, and properties," *J. Appl. Phys.*, vol. 94, no. 5, pp. 2779–2808, 2003.

[56] R. C. Powell, N. E. Lee, Y. W. Kim, and J. E. Greene, "Heteroepitaxial wurtzite and zinc-blende structure GaN grown by reactive-ion molecular-beam epitaxy: Growth kinetics, microstructure, and properties," *J. Appl. Phys.*, vol. 73, no. 1, pp. 189–204, 1993.

[57] A. Botchkarev, A. Salvador, B. Sverdlov, J. Myoung, and H. Morkoç, "Properties of GaN films grown under Ga and N rich conditions with plasma enhanced molecular beam epitaxy," *J. Appl. Phys.*, vol. 77, no. 9, pp. 4456–4458, 1995.

[58] R. J. Molnar and T. D. Moustakas, "Growth of gallium nitride by electron-cyclotron resonance plasma-assisted molecular-beam epitaxy: The role of charged species," *J. Appl. Phys.*, vol. 76, no. 8, pp. 4587–4595, 1994.

[59] R. Singh, D. Doppalapudi, T. D. Moustakas, and L. T. Romano, "Phase separation in InGaN thick films and formation of InGaN/GaN double heterostructures in the entire alloy composition," *Appl. Phys. Lett.*, vol. 70, no. 9, pp. 1089–1091, 1997.

[60] N. A. El-Masry, E. L. Piner, S. X. Liu, and S. M. Bedair, "Phase separation in InGaN grown by metalorganic chemical vapor deposition," *Appl. Phys. Lett.*, vol. 72, no. 1, pp. 40–42, 1998.

[61] D. Doppalapudi, S. N. Basu, K. F. Ludwig, and T. D. Moustakas, "Phase separation and ordering in InGaN alloys grown by molecular beam epitaxy," *J. Appl. Phys.*, vol. 84, no. 3, pp. 1389–1395, 1998.

[62] I. H. Ho and G. B. Stringfellow, "Solid phase immiscibility in GaInN," *Appl. Phys. Lett.*, vol. 69, no. 18, pp. 2701–2703, 1996.

[63] S. Chichibu, "Exciton localization in InGaN quantum well devices," *J. Vac. Sci. Technol. B Microelectron. Nanom. Struct.*, vol. 16, no. 4, p. 2204, 1998.

[64] F. Wang *et al.*, "Green and blue emissions in phase-separated InGaN quantum wells," *J. Appl. Phys.*, vol. 114, no. 16, pp. 1–5, 2013.

[65] R. A. Oliver *et al.*, "Microstructural origins of localization in InGaN quantum wells," *J. Phys. D. Appl. Phys.*, vol. 43, no. 35, 2010.

[66] Y. L. Lai *et al.*, "Origins of efficient green light emission in phase-separated InGaN quantum wells," *Nanotechnology*, vol. 17, no. 15, pp. 3734–3739, 2006.

[67] Ž. Gačević *et al.*, "A comprehensive diagram to grow (0001)InGaN alloys by molecular beam epitaxy," *J. Cryst. Growth*, vol. 364, pp. 123–127, 2013.

[68] C. A. M. Fabien and W. A. Doolittle, "Guidelines and limitations for the design of high-efficiency InGaN single-junction solar cells," *Sol. Energy Mater. Sol. Cells*, vol. 130, pp. 354–363, 2014.

[69] C. A. M. M. Fabien, A. Maros, C. B. Honsberg, and W. A. Doolittle, "III-Nitride Double-Heterojunction Solar Cells with High In-Content InGaN Absorbing Layers: Comparison of Large-Area and Small-Area Devices," *IEEE J. Photovoltaics*, vol. 6, no. 2, pp. 460–464, 2016.

[70] B. R. Jampana *et al.*, "Design and realization of wide-band-Gap (~ 2.67 eV) InGaN p-n junction solar cell," *IEEE Electron Device Lett.*, vol. 31, no. 1, pp. 32–34, 2010.

[71] R. H. Horng *et al.*, "Improved conversion efficiency of GaN/InGaN thin-film solar cells," *IEEE Electron Device Lett.*, vol. 30, no. 7, pp. 724–726, 2009.

[72] A. G. Bhuiyan, K. Sugita, A. Hashimoto, and A. Yamamoto, "InGaN solar cells: Present state of the art and important challenges," *IEEE J. Photovoltaics*, vol. 2, no. 3, pp. 276–293, 2012.

[73] C. Jiang *et al.*, "Enhanced Solar Cell Conversion Efficiency of InGaN/GaN Multiple Quantum Wells by Piezo-Phototronic Effect," *ACS Nano*, vol. 11, no. 9, pp. 9405–9412, 2017.

[74] E. Vadiee *et al.*, "InGaN solar cells with regrown GaN homojunction tunnel contacts," *Appl. Phys. Express*, vol. 11, no. 8, p. 082304, 2018.

[75] D. J. As *et al.*, "Incorporation and optical properties of magnesium in cubic GaN epilayers grown by molecular beam epitaxy," *Appl. Phys. Lett.*, vol. 73, no. 13, pp. 1835–1837, 1998.

[76] K. B. Nam, M. L. Nakarmi, J. Li, J. Y. Lin, and H. X. Jiang, "Mg acceptor level in AlN probed by deep ultraviolet photoluminescence," *Appl. Phys. Lett.*, vol. 83, no. 5, pp. 878–880, 2003.

[77] S. Nakamura, T. Mukai, M. Senoh, I. Naruhito, and N. Iwasa, "Thermal Annealing Effects on P-Type Mg-Doped GaN Films," *Jpn. J. Appl. Phys.*, vol. 31, no. 2B, p. L 139-L 142, 1992.

[78] U. Kaufmann, P. Schlotter, H. Obloh, K. Köhler, and M. Maier, "Hole conductivity

and compensation in epitaxial GaN:Mg layers," *Phys. Rev. B - Condens. Matter Mater. Phys.*, vol. 62, no. 16, pp. 10867–10872, 2000.

[79] G. Miceli and A. Pasquarello, "Self-compensation due to point defects in Mg-doped GaN," *Phys. Rev. B*, vol. 93, no. 16, pp. 1–11, 2016.

[80] P. Vennéguès *et al.*, "Atomic structure of pyramidal defects in Mg-doped GaN," *Phys. Rev. B - Condens. Matter Mater. Phys.*, vol. 68, no. 23, pp. 1–8, 2003.

[81] K. Iwata *et al.*, "Atomic resolution structural analysis of magnesium segregation at a pyramidal inversion domain in a GaN epitaxial layer," *Appl. Phys. Express*, vol. 12, no. 3, 2019.

[82] A. Bhattacharyya, W. Li, J. Cabalu, T. D. Moustakas, D. J. Smith, and R. L. Hervig, "Efficient p -type doping of GaN films by plasma-assisted molecular beam epitaxy," *Appl. Phys. Lett.*, vol. 85, no. 21, pp. 4956–4958, 2004.

[83] R. R. Lieten *et al.*, "Mg doping of GaN by molecular beam epitaxy," *J. Phys. D. Appl. Phys.*, vol. 44, no. 13, 2011.

[84] H. Turski *et al.*, "Growth rate independence of Mg doping in GaN grown by plasma-assisted MBE," *J. Cryst. Growth*, vol. 482, pp. 56–60, 2018.

[85] N. Tetsuo, I. Nobuyuki, T. Kazuyoshi, K. Keita, and K. Tetsu, "Wide range doping control and defect characterization of GaN layers with various Mg concentrations," *J. Appl. Phys.*, vol. 124, no. 16, 2018.

[86] D. S. Meyaard *et al.*, "Asymmetry of carrier transport leading to efficiency droop in GaInN based light-emitting diodes," *Appl. Phys. Lett.*, vol. 99, no. 25, pp. 1–4, 2011.

[87] B. Galler *et al.*, "Investigation of the carrier distribution in InGaN-based multi-quantum-well structures," *Phys. Status Solidi Curr. Top. Solid State Phys.*, vol. 8, no. 7–8, pp. 2372–2374, 2011.

[88] S. H. Han *et al.*, "Effect of electron blocking layer on efficiency droop in InGaN/GaN multiple quantum well light-emitting diodes," *Appl. Phys. Lett.*, vol. 94, no. 23, pp. 1–4, 2009.

[89] C. H. Wang *et al.*, "Hole injection and efficiency droop improvement in InGaN/GaN light-emitting diodes by band-engineered electron blocking layer," *Appl. Phys. Lett.*, vol. 97, no. 26, pp. 1–4, 2010.

[90] R. M. Lin, S. F. Yu, S. J. Chang, T. H. Chiang, S. P. Chang, and C. H. Chen, "Inserting a p-InGaN layer before the p-AlGaN electron blocking layer suppresses efficiency droop in InGaN-based light-emitting diodes," *Appl. Phys. Lett.*, vol. 101, no. 8, 2012.

[91] F. Zhang *et al.*, "Improvement of carrier injection symmetry and quantum efficiency

in InGaN light-emitting diodes with Mg delta-doped barriers," *Appl. Phys. Lett.*, vol. 106, no. 18, 2015.

[92] H. Hirayama, N. Maeda, S. Fujikawa, S. Toyoda, and N. Kamata, "Recent progress and future prospects of AlGaN-based high-efficiency deep-ultraviolet light-emitting diodes," *Jpn. J. Appl. Phys.*, vol. 53, p. 100209, 2014.

[93] H. Ryu, I. Choi, H. H. R. I. Choi, J. Shim, and H. C. J. Shim, "Investigation of Light Extraction Efficiency in AlGaN Deep-Ultraviolet Light-Emitting Diodes," *Appl. Phys. Express*, vol. 6, p. 062101, 2013.

[94] N. Maeda and H. Hirayama, "Realization of high-efficiency deep-UV LEDs using transparent p-AlGaN contact layer," *Phys. Status Solidi*, vol. 10, no. 11, pp. 1521–1524, 2013.

[95] L. Esaki, "New phenomenon in narrow germanium p-n junctions [3]," *Phys. Rev.*, vol. 109, no. 2, pp. 603–604, 1958.

[96] C. T. Van Degrift, "Tunnel diode oscillator for 0.001 ppm measurements at low temperatures," *Rev. Sci. Instrum.*, vol. 46, no. 5, pp. 599–607, 1975.

[97] M. E. Hines, "High-Frequency Negative-Resistance Circuit Principles for Esaki Diode Applications," *Bell Syst. Tech. J.*, vol. 39, no. 3, pp. 477–513, May 1960.

[98] H. Sugiura, C. Amano, A. Yamamoto, and M. Yamaguchi, "Double heterostructure GaAs tunnel junction for a AlGaAs/GaAs tandem solar cell," *Jpn. J. Appl. Phys.*, vol. 27, no. 2R, pp. 269–272, 1988.

[99] J. P. Van Der Ziel and W. T. Tsang, "Integrated multilayer GaAs lasers separated by tunnel junctions," *Appl. Phys. Lett.*, vol. 41, no. 6, pp. 499–501, 1982.

[100] M. J. Grundmann and U. K. Mishra, "Multi- color light emitting diode using polarization- induced tunnel junctions," *Phys. Status Solidi*, vol. 4, no. 7, pp. 2830–2833, 2007.

[101] J. Simon *et al.*, "Polarization-Induced Zener Tunnel Junctions in Wide-Band-Gap Heterostructures," *Phys. Rev. Lett.*, vol. 103, no. 2, p. 026801, Jul. 2009.

[102] S. Krishnamoorthy, D. N. Nath, F. Akyol, P. S. Park, M. Esposto, and S. Rajan, "Polarization-engineered GaN/InGaN/GaN tunnel diodes," *Appl. Phys. Lett.*, vol. 97, no. 102, pp. 203502–113503, 2010.

[103] S. Krishnamoorthy, P. S. Park, and S. Rajan, "Demonstration of forward inter-band tunneling in GaN by polarization engineering," *Appl. Phys. Lett.*, vol. 99, no. 10, pp. 233504–203502, Dec. 2011.

[104] S. R. Jeon, Y. H. Song, H. J. Jang, G. M. Yang, S. W. Hwang, and S. J. Son, "Lateral current spreading in GaN-based light-emitting diodes utilizing tunnel contact

junctions," *Appl. Phys. Lett.*, vol. 78, no. 21, pp. 3265–3267, 2001.

[105] J. K. Sheu *et al.*, "Low-Operation Voltage of InGaN / GaN Superlattice Tunneling Contact Layer," *IEEE Electron Device Lett.*, vol. 22, no. 10, pp. 460–462, 2001.

[106] T. C. Wen *et al.*, "InGaN/GaN tunnel-injection blue light-emitting diodes," *IEEE Trans. Electron Devices*, vol. 49, no. 6, pp. 1093–1095, 2002.

[107] Z. H. Zhang *et al.*, "InGaN/GaN light-emitting diode with a polarization tunnel junction," *Appl. Phys. Lett.*, vol. 102, no. 19, p. 193508, 2013.

[108] S. Okawara, Y. Aoki, M. Kuwabara, Y. Takagi, J. Maeda, and H. Yoshida, "Nitride-based stacked laser diodes with a tunnel junction," *Appl. Phys. Express*, vol. 11, no. 1, p. 012701, 2018.

[109] H. Kurokawa *et al.*, "Multijunction GaInN-based solar cells using a tunnel junction," *Appl. Phys. Express*, vol. 7, no. 3, p. 034104, 2014.

[110] J. Wu *et al.*, "Unusual properties of the fundamental band gap of InN," *Appl. Phys. Lett.*, vol. 80, no. 21, pp. 3967–3969, 2002.

[111] J. F. Muth *et al.*, "Absorption coefficient, energy gap, exciton binding energy, and recombination lifetime of GaN obtained from transmission measurements," *Appl. Phys. Lett.*, vol. 71, no. 18, pp. 2572–2574, 1997.

[112] J. Wu *et al.*, "Superior radiation resistance of In1-xGaxN alloys: Full-solar-spectrum photovoltaic material system," *J. Appl. Phys.*, vol. 94, no. 10, pp. 6477–6482, 2003.

[113] J. J. Williams *et al.*, "Refractory InGaN Solar Cells for High-Temperature Applications," *IEEE J. Photovoltaics*, vol. 7, no. 6, pp. 1646–1651, 2017.

[114] J. J. Williams *et al.*, "Development of a high-band gap high temperature III-nitride solar cell for integration with concentrated solar power technology," *2017 IEEE 44th Photovolt. Spec. Conf. PVSC 2017*, pp. 193–195, 2018.

[115] C. A. M. Fabien *et al.*, "Simulations, Practical Limitations, and Novel Growth Technology for InGaN-Based Solar Cells," *IEEE J. Photovoltaics*, vol. 4, no. 2, pp. 601–606, Mar. 2014.

[116] N. G. Young *et al.*, "High-performance broadband optical coatings on InGaN/GaN solar cells for multijunction device integration," *Appl. Phys. Lett.*, vol. 104, p. 163902, 2014.

[117] M. Kamp, M. Mayer, A. Pelzmann, and K. J. Ebeling, "Fundamentals, Material Properties and Device Performances in GaN MBE using On-Surface Cracking of Ammonia," *MRS Internet J. Nitride Semicond. Res.*, vol. 2, 1997.

[118] H. M. Mott-Smith and I. Langmuir, "The theory of collectors in gaseous

discharges," *Phys. Rev.*, vol. 28, no. 4, pp. 727–763, 1926.

[119] M. B. Hopkins and W. G. Graham, "Langmuir probe technique for plasma parameter measurement in a medium density discharge," *Rev. Sci. Instrum.*, vol. 57, no. 9, pp. 2210–2217, 1986.

[120] A. V. Blant, O. H. Hughes, T. S. Cheng, S. V. Novikov, and C. T. Foxon, "Nitrogen species from radio frequency plasma sources used for molecular beam epitaxy growth of GaN," *Plasma Sources Sci. Technol.*, vol. 9, no. 1, pp. 12–17, 2000.

[121] E. Iliopoulos, A. Adikimenakis, E. Dimakis, K. Tsagaraki, G. Konstantinidis, and A. Georgakilas, "Active nitrogen species dependence on radiofrequency plasma source operating parameters and their role in GaN growth," *J. Cryst. Growth*, vol. 278, no. 1–4, pp. 426–430, 2005.

[122] S. Porowski and I. Grzegory, "Thermodynamical properties of III-V nitrides and crystal growth of GaN at high N2 pressure," *J. Cryst. Growth*, vol. 178, no. 1–2, pp. 174–188, 1997.

[123] M. Moseley, D. Billingsley, W. Henderson, E. Trybus, and W. A. Doolittle, "Transient atomic behavior and surface kinetics of GaN," *J. Appl. Phys.*, vol. 106, no. 1, p. 014905, 2009.

[124] C. S. Gallinat, G. Koblmüller, J. S. Brown, and J. S. Speck, "A growth diagram for plasma-assisted molecular beam epitaxy of In-face InN," *J. Appl. Phys.*, vol. 102, no. 6, p. 064907, 2007.

[125] R. L. Merlino, "Understanding Langmuir probe current-voltage characteristics," *Am. J. Phys.*, vol. 75, no. 12, pp. 1078–1085, 2007.

[126] N. Hershkowitz, *How Langmuir Probes Work*. Academic Press, Inc., 1989.

[127] A. A. Azooz, "Four free parameter empirical parametrization of glow discharge Langmuir probe data," *Rev. Sci. Instrum.*, vol. 79, no. 10, p. 103501, 2008.

[128] A. A. Klochikhin *et al.*, "Acceptor states in the photoluminescence spectra of n-InN," vol. 71, no. 19, p. 195207, 2005.

[129] T. Matsuoka, H. Okamoto, M. Nakao, H. Harima, and E. Kurimoto, "Optical bandgap energy of wurtzite InN," vol. 81, no. 7, pp. 1246–1248, 2003.

[130] V. Y. Davydov *et al.*, "Band Gap of Hexagonal InN and InGaN Alloys," vol. 234, no. 3, pp. 787–795, 2002.

[131] I. Mahboob, T. D. Veal, C. F. Mcconville, H. Lu, and W. J. Schaff, "Intrinsic Electron Accumulation at Clean InN Surfaces," *Phys. Rev. Lett.*, vol. 92, no. 3, p. 036804, 2004.

[132] B. Arnaudov *et al.*, "Energy position of near-band-edge emission spectra of InN epitaxial layers with different doping levels," *Phys. Rev. B*, vol. 69, no. 11, p. 115216, 2004.

[133] M. Feneberg, J. Däubler, K. Thonke, R. Sauer, P. Schley, and R. Goldhahn, "Mahan excitons in degenerate wurtzite InN: Photoluminescence spectroscopy and reflectivity measurements," *Phys. Rev. B*, vol. 77, no. 24, p. 245207, 2008.

[134] T. S. Moss, "The Interpretation of the Properties of Indium Antimonide," *Proc. Phys. Soc. Sect. B*, vol. 67, pp. 775–782, 1954.

[135] H. Wang and A. B. Chen, "Calculation of shallow donor levels in GaN," *J. Appl. Phys.*, vol. 87, no. 11, pp. 7859–7863, Jun. 2000.

[136] S. Fritze *et al.*, "High Si and Ge n-type doping of GaN doping - Limits and impact on stress," *Appl. Phys. Lett.*, vol. 100, no. 12, 2012.

[137] P. Bogusławski and J. Bernholc, "Doping properties of C , Si , and Ge impurities in GaN and AlN," *Phys. Rev. B*, vol. 56, no. 15, pp. 9496–9505, 1997.

[138] M. Moseley, D. Billingsley, W. Henderson, E. Trybus, and W. A. Doolittle, "Transient atomic behavior and surface kinetics of GaN," *J. Appl. Phys.*, vol. 106, no. 1, p. 014905, 2009.

[139] A. R. Smith *et al.*, "Determination of wurtzite GaN lattice polarity based on surface reconstruction," *Appl. Phys. Lett.*, vol. 72, no. 17, pp. 2114–2116, 1998.

[140] W. Götz, N. M. Johnson, J. Walker, D. P. Bour, and R. A. Street, "Activation of acceptors in Mg-doped GaN grown by metalorganic chemical vapor deposition," *Appl. Phys. Lett.*, vol. 667, no. October 1995, p. 667, 1995.

[141] G. Y. Zhang, Y. Z. Tong, Z. J. Yang, S. X. Jin, J. Li, and Z. Z. Gan, "Relationship of background carrier concentration and defects in GaN grown by metalorganic vapor phase epitaxy," *Appl. Phys. Lett.*, vol. 71, no. 23, pp. 3376–3378, Dec. 1997.

[142] C. Stampfl and C. G. Van De Walle, "Doping of AlxGa1-xN," *Appl. Phys. Lett.*, vol. 72, no. 4, pp. 459–461, Jan. 1998.

[143] F. Bernardini, V. Fiorentini, and A. Bosin, "Theoretical evidence for efficient p-type doping of GaN using beryllium," *Appl. Phys. Lett.*, vol. 70, no. 22, pp. 2990–2992, 1997.

[144] C. G. Van de Walle, C. Stampfl, and J. Neugebauer, "Theory of doping and defects in III–V nitrides," *J. Cryst. Growth*, vol. 189, pp. 505–510, 1998.

[145] M. Feneberg *et al.*, "Band gap renormalization and Burstein-Moss effect in silicon- and germanium-doped wurtzite GaN up to 1020 cm-3," *Phys. Rev. B - Condens. Matter Mater. Phys.*, vol. 90, no. 7, pp. 1–10, 2014.

[146] C. Berger *et al.*, "Metalorganic chemical vapor phase epitaxy of narrow-band distributed Bragg reflectors realized by GaN:Ge modulation doping," *J. Cryst. Growth*, vol. 440, pp. 6–12, Apr. 2016.

[147] J. Park, J. H. Kang, and S. W. Ryu, "High diffuse reflectivity of nanoporous gan distributed bragg reflector formed by electrochemical etching," *Appl. Phys. Express*, vol. 6, no. 7, p. 072201, Jul. 2013.

[148] T. Zhu *et al.*, "Wafer-scale Fabrication of Non-Polar Mesoporous GaN Distributed Bragg Reflectors via Electrochemical Porosification," *Sci. Rep.*, vol. 7, no. 1, pp. 1–8, Mar. 2017.

[149] M. Mandurrino *et al.*, "Physics-based modeling and experimental implications of trap-assisted tunneling in InGaN/GaN light-emitting diodes," *Phys. Status Solidi Appl. Mater. Sci.*, vol. 212, no. 5, pp. 947–953, 2015.

[150] D. Zhu *et al.*, "The origin of the high diode-ideality factors in GaInN/GaN multiple quantum well light-emitting diodes," *Appl. Phys. Lett.*, vol. 94, no. 8, p. 081113, 2009.

[151] C. Skierbiszewski *et al.*, "True-blue laser diodes with tunnel junctions grown monolithically by plasma-assisted molecular beam epitaxy," *Appl. Phys. Express*, vol. 11, p. 034103, 2018.

[152] M. Malinverni *et al.*, "InGaN laser diode with metal-free laser ridge using n^+-GaN contact layers," *Appl. Phys. Express*, vol. 9, no. 6, p. 061004, Jun. 2016.

[153] S. Fischer, C. Wetzel, E. E. Haller, and B. K. Meyer, "On p-type doping in GaN - acceptor binding energies," *Appl. Phys. Lett.*, vol. 67, no. 9, p. 1298, 1995.

[154] H. Xing *et al.*, "Memory effect and redistribution of Mg into sequentially regrown GaN layer by metalorganic chemical vapor deposition," *Jpn. J. Appl. Phys.*, vol. 42, no. 1, pp. 50–53, 2003.

[155] Y. Ohba and A. Hatano, "A study on strong memory effects for Mg doping in GaN metalorganic chemical vapor deposition," *J. Cryst. Growth*, vol. 145, no. 1–4, pp. 214–218, Dec. 1994.

[156] D. Hwang, A. Mughal, M. S. Wong, A. I. Alhassan, S. Nakamura, and S. P. DenBaars, "Micro-light-emitting diodes with III–nitride tunnel junction contacts grown by metalorganic chemical vapor deposition Sustained high external quantum efficiency in ultrasmall blue III–nitride micro-LEDs," *Appl. Phys. Express*, vol. 11, p. 012102, 2018.

[157] R. Czernecki *et al.*, "Hydrogen diffusion in GaN:Mg and GaN:Si," *J. Alloys Compd.*, vol. 747, pp. 354–358, 2018.

[158] B. P. Gunning *et al.*, "Comprehensive study of the electronic and optical behavior

of highly degenerate p-type Mg-doped GaN and AlGaN," *J. Appl. Phys.*, vol. 117, no. 4, p. 045710, 2015.

[159] B. Gunning, J. Lowder, M. Moseley, and W. Alan Doolittle, "Negligible carrier freeze-out facilitated by impurity band conduction in highly p-type GaN," *Appl. Phys. Lett.*, vol. 101, no. 8, p. 082106, Aug. 2012.

[160] F. Akyol, S. Krishnamoorthy, Y. Zhang, J. Johnson, J. Hwang, and S. Rajan, "Low-resistance GaN tunnel homojunctions with 150 kA/cm ^{2} current and repeatable negative differential resistance," *Appl. Phys. Lett.*, vol. 108, no. 13, p. 131103, Mar. 2016.

[161] A. M. Andrews, H. W. Korb, N. Holonyak, C. B. Duke, and G. G. Kleiman, "Tunnel mechanisms and junction characterization in III-V tunnel diodes," *Phys. Rev. B*, vol. 5, no. 6, pp. 2273–2295, 1972.

[162] C. Bayram, Z. Vashaei, and M. Razeghi, "Reliability in room-temperature negative differential resistance characteristics of low-aluminum content AlGaN/GaN double-barrier resonant tunneling diodes," *Appl. Phys. Lett.*, vol. 97, no. 18, p. 181109, 2010.

[163] C. Bayram, Z. Vashaei, and M. Razeghi, "Room temperature negative differential resistance characteristics of polar III-nitride resonant tunneling diodes," *Appl. Phys. Lett.*, vol. 97, no. 9, p. 092104, 2010.

[164] O. Contreras, F. A. Ponce, J. Christen, A. Dadgar, and A. Krost, "Dislocation annihilation by silicon delta-doping in GaN epitaxy on Si," *Appl. Phys. Lett.*, vol. 81, no. 25, pp. 4712–4714, Dec. 2003.

[165] J. T. Leonard *et al.*, "Demonstration of a III-nitride vertical-cavity surface-emitting laser with a III-nitride tunnel junction intracavity contact," *Appl. Phys. Lett.*, vol. 107, no. 9, p. 091105, Aug. 2015.

[166] E. C. Young *et al.*, "Hybrid tunnel junction contacts to III-nitride light-emitting diodes," *Appl. Phys. Express*, vol. 9, no. 2, p. 022102, Feb. 2016.

[167] J. R. Jinschek, R. Erni, N. F. Gardner, A. Y. Kim, and C. Kisielowski, "Local indium segregation and bang gap variations in high efficiency green light emitting InGaN/GaN diodes," *Solid State Commun.*, vol. 137, no. 4, pp. 230–234, Jan. 2006.

[168] Y. Kuwano *et al.*, "Lateral Hydrogen Diffusion at p-GaN Layers in Nitride-Based Light Emitting Diodes with Tunnel Junctions," *Jpn. J. Appl. Phys.*, vol. 52, p. 08JK12, 2013.

[169] M. R. Mahat *et al.*, "Electronic surface, optical and electrical properties of p – GaN activated via in-situ MOCVD and ex-situ thermal annealing in InGaN/GaN LED," *Mater. Sci. Semicond. Process.*, vol. 106, p. 104757, Feb. 2020.

[170] B. P. Yonkee, E. C. Young, S. P. DenBaars, S. Nakamura, and J. S. Speck, "Silver free III-nitride flip chip light-emitting-diode with wall plug efficiency over 70% utilizing a GaN tunnel junction," *Appl. Phys. Lett.*, vol. 109, no. 19, p. 191104, Nov. 2016.

[171] M. A. Khan, "AlGaN multiple quantum well based deep UV LEDs and their applications," *Phys. status solidi*, vol. 203, no. 7, pp. 1764–1770, 2006.

[172] J. Cho, E. F. Schubert, and J. K. Kim, "Efficiency droop in light-emitting diodes: Challenges and countermeasures," *Laser Photon. Rev.*, vol. 7, no. 3, pp. 408–421, 2013.

[173] Q. Dai *et al.*, "Carrier recombination mechanisms and efficiency droop in GaInN/GaN light-emitting diodes," *Appl. Phys. Lett.*, vol. 97, no. 13, p. 133507, Sep. 2010.

[174] E. Kioupakis, P. Rinke, K. T. Delaney, and C. G. Van De Walle, "Indirect Auger recombination as a cause of efficiency droop in nitride light-emitting diodes," *Appl. Phys. Lett.*, vol. 98, no. 161107, 2011.

[175] E. A. Clinton, E. Vadiee, S. C. Shen, K. Mehta, P. D. Yoder, and W. A. Doolittle, "Negative differential resistance in GaN homojunction tunnel diodes and low voltage loss tunnel contacts," *Appl. Phys. Lett.*, vol. 112, no. 25, p. 252103, 2018.

[176] D. Jena *et al.*, "Polarization-engineering in group III-nitride heterostructures: New opportunities for device design," *Phys. status solidi*, vol. 208, no. 7, pp. 1511–1516, 2011.

[177] S. Lee *et al.*, "GaN-based vertical-cavity surface-emitting lasers with tunnel junction contacts grown by metal-organic chemical vapor deposition," *Appl. Phys. Express*, vol. 11, p. 062703, 2018.

[178] Y. Zhang *et al.*, "Design and demonstration of ultra-wide bandgap AlGaN tunnel junctions," *Appl. Phys. Lett.*, vol. 109, no. 2016, p. 121102, 2017.

[179] Y. Zhang *et al.*, "Interband tunneling for hole injection in III-nitride ultraviolet emitters," *Appl. Phys. Lett.*, vol. 106, p. 141103, 2015.

[180] Y. Taniyasu, M. Kasu, and N. Kobayashi, "Intentional control of n -type conduction for for Si-doped AlN and AlxGa1-xN (0.42<x<1)," *Appl. Phys. Lett.*, vol. 81, p. 1255, 2002.

[181] B. Gunning, J. Lowder, M. Moseley, W. A. Doolittle, and W. Alan Doolittle, "Negligible carrier freeze-out facilitated by impurity band conduction in highly p-type GaN," *Appl. Phys. Lett.*, vol. 101, no. 8, p. 082106, Aug. 2012.

[182] A. Pandey *et al.*, "Enhanced doping efficiency of ultrawide band gap semiconductors by metal-semiconductor junction assisted epitaxy," *Phys. Rev.*

Mater., vol. 3, no. 5, p. 053401, 2019.

[183] J. Shao, D. N. Zakharov, C. Edmunds, O. Malis, and M. J. Manfra, "Homogeneous AlGaN/GaN superlattices grown on free-standing (1 1$\bar{0}$0) GaN substrates by plasma-assisted molecular beam epitaxy," *Appl. Phys. Lett.*, vol. 103, no. 23, pp. 0–4, 2013.

[184] M. Gao *et al.*, "Compositional modulation and optical emission in AlGaN epitaxial films," *J. Appl. Phys.*, vol. 100, no. 10, 2006.

[185] M. E. Zvanut, Y. Uprety, J. Dashdorj, M. Moseley, and W. Alan Doolittle, "Passivation and activation of Mg acceptors in heavily doped GaN," *J. Appl. Phys.*, vol. 110, no. 4, p. 044508, 2011.

[186] Z. Hu *et al.*, "Near unity ideality factor and Shockley-Read-Hall lifetime in GaN-on-GaN p-n diodes with avalanche breakdown," *Appl. Phys. Lett.*, vol. 107, no. 24, 2015.

[187] S. Pereira *et al.*, "Structural and optical properties of InGaN / GaN layers close to the critical layer thickness," *Appl. Phys. Lett.*, vol. 81, no. June, pp. 1207–1209, 2002.

[188] B. Heying *et al.*, "Role of threading dislocation structure on the x-ray diffraction peak widths in epitaxial GaN films," *Appl. Phys. Lett.*, vol. 68, no. 5, pp. 643–645, 1996.

[189] R. Dalmau *et al.*, "Growth and Characterization of AlN and AlGaN Epitaxial Films on AlN Single Crystal Substrates," *J. Electrochem. Soc.*, vol. 158, no. 5, p. H530, 2011.

[190] E. A. Clinton, E. Vadiee, M. B. Tellekamp, and W. A. Doolittle, "Observation and mitigation of RF-plasma-induced damage to III-nitrides grown by molecular beam epitaxy," *J. Appl. Phys.*, vol. 126, no. 1, p. 015705, 2019.

[191] E. Vadiee *et al.*, "The role of Mg bulk hyper-doping and delta- doping in low-resistance GaN homojunction tunnel diodes with negative differential resistance The role of Mg bulk hyper-doping and delta-doping in low-resistance GaN homojunction tunnel diodes with negative diff," *J. Appl. Phys.*, vol. 126, p. 083110, 2019.

[192] E. A. Clinton, Z. Engel, E. Vadiee, J. V Carpenter, Z. C. Holman, and W. A. Doolittle, "Ultra-wide-bandgap AlGaN homojunction tunnel diodes with negative differential resistance," *Appl. Phys. Lett.*, vol. 115, p. 082104, 2019.

VITA

Evan Clinton was raised in Vienna, Virginia by his mother and father Dorothy and Andrew Clinton. He attended James Madison High School in Vienna where his interest in science and engineering grew. He then attended Virginia Polytechnic Institute and State University where he received a Bachelor's degree in Electrical Engineering in 2013. Afterwards, he attended the Georgia Institute of Technology where he received a Master's degree in Electrical and Computer Engineering in 2015. He plans to receive his Ph.D. in March of 2020 under the supervision of Prof. W. Alan Doolittle. His research interests include the synthesis and characterization of novel III-nitride materials and devices.

First-Authored and Co-Authored Publications

E. Clinton, Z. Engel, E. Vadiee, J. Carpenter, Z. Holman, and W. A. Doolittle. "Ultra-wide-bandgap AlGaN homojunction tunnel diodes with negative differential resistance," *Appl. Phys. Lett.*, vol. 115, p. 082104, 2019.

E. Clinton, E. Vadiee, M. B. Tellekamp, and W. A. Doolittle. "Observation and mitigation of RF-plasma-induced damage to III-nitrides grown by molecular beam epitaxy," *J. Appl. Phys.*, vol. 126, no. 1, p. 015705, 2019.

E. Clinton, E. Vadiee, S. C. Shen, K. Mehta, P. D. Yoder, and W. A. Doolittle. "Negative differential resistance in GaN homojunction tunnel diodes and low voltage loss tunnel contacts," *Appl. Phys. Lett.*, vol. 112, no. 25, p. 252103, 2018.

E. Clinton, E. Vadiee, C. Fabien, M. Moseley, B. Gunning, W. A. Doolittle, A. Fischer, Y.O. Wei, H. Xie, and F. Ponce. "A review of the synthesis of reduced defect density $In_xGa_{1-x}N$ for all indium compositions," *Solid. State. Electron.*, vol. 136, pp. 3–11, 2017.

E. Vadiee, A. Fischer, **E. Clinton**, H. McFavilen, A. Patadia, C. Arena, F. Ponce, R. King, C. Honsberg, and W. A. Doolittle. "Evaluating the performance of InGaN/GaN multi-quantum-well solar cells operated at elevated temperatures via DC and small-signal AC analysis," *Jpn. J. Appl. Phys.*, vol. 58, p. 101003, 2019.

E. Vadiee, **E. Clinton**, J. Carpenter, H. McFavilen, C. Arena, Z. Holman, C. Honsberg, and W. A. Doolittle. "The role of Mg bulk hyper-doping and delta- doping in low-resistance GaN homojunction tunnel diodes with negative differential resistance," *J. Appl. Phys.*, vol. 126, p. 083110, 2019.

E. Vadiee, **E. Clinton**, H. McFavilen, A. Weidenbach, Z. Engel, C. Matthews, C. Zhang, *et al*. "InGaN solar cells with regrown GaN homojunction tunnel contacts," *Appl. Phys. Express*, vol. 11, no. 8, p. 082304, 2018.

E. Vadiee, **E. Clinton**, H. McFavilen, Z. Engel, C. Matthews, C. Arena, C. Honsberg, Stephen M. Goodnick, and W.A. Doolittle. "InGaN based solar cells with GaN tunnel junction contacts," *2018 IEEE 7th WCPEC*, pp. 965–968, 2018.

E. Vadiee, **E. Clinton**, H. McFavilen, A.M. Fischer, Y. Fang, J. Williams, C. Honsberg, W. A. Doolittle, and S. Goodnick. "Progress towards double-junction InGaN solar cell," *2017 IEEE 44th Photovolt. Spec. Conf.*, pp. 305–308, 2018.

B. Gunning, **E. Clinton**, J. Merola, W. A. Doolittle, and R.C. Bresnahan. "Control of ion content and nitrogen species using a mixed chemistry plasma for GaN grown at extremely high growth rates >9 μm/h by plasma-assisted molecular beam epitaxy," *J. Appl. Phys.*, vol. 118, no. 15, p. 155302, 2015.

B. Gunning, C. Fabien, J. Merola, **E. Clinton**, W. A. Doolittle, S. Wang, A.M. Fischer, and F.A. Ponce. "Comprehensive study of the electronic and optical behavior of highly degenerate p-type Mg-doped GaN and AlGaN," *J. Appl. Phys.*, vol. 117, no. 4, p. 045710, 2015.

First-Authored Conference Presentations

E. Clinton, E. Vadiee, M. B. Tellekamp, Z. Engel, C. Matthews, and W. A. Doolittle, "Engineering the Nitrogen Plasma to Reduce Defects in InN Resulting in a 0.12 eV Moss-Burstein Shift Towards the Fundamental Bandgap," 13th International Conference on Nitride Semiconductors, Bellevue, Washington, USA, July 2019.

E. Clinton, E. Vadiee, Z. Engel, C. Matthews, and W. A. Doolittle, "First Demonstration of Negative Differential Resistance in $Al_xGa_{1-x}N$ Homojunction Tunnel Diodes up to x=0.19 and High Reverse Bias Tunneling up to x=0.58 to Enable Ultraviolet Optoelectronics," 13th International Conference on Nitride Semiconductors, Bellevue, Washington, USA, July 2019.

E. Clinton, E. Vadiee, M. B. Tellekamp, Z. Engel, C. Matthews, and W. A. Doolittle,

"Plasma Control of Defects in InN: Correlation to Residual Electron Concentration and Moss-Burstein Effect," 61st Electronic Materials Conference, Ann Arbor, Michigan, USA, June 2019.

E. Clinton, E. Vadiee, Z. Engel, C. Matthews, and W. A. Doolittle, "$Al_xGa_{1-x}N$ ($0<x<0.6$) Homojunction Tunnel Diodes Exhibiting Low Voltage Negative Differential Resistance: Progress towards Tunnel Contacts Compatible with Ultraviolet Optoelectronics," 61st Electronic Materials Conference, Ann Arbor, Michigan, USA, June 2019.

E. Clinton, E. Vadiee, Z. Engel, C. Matthews, and W. A. Doolittle, "Plasma Considerations for Growth of High In Content III-Nitrides," International Workshop on Nitride Semiconductors, Kanazawa, Japan, November 2018.

E. Clinton, E. Vadiee, K. Mehta, P. D. Yoder, Z. Engel, C. Matthews, A. Weidenbach, H. McFavilen, C. Arena, and W. A. Doolittle, "GaN Homojunction Tunnel Diodes Exhibiting Negative Differential Resistance and their Application as Tunnel Contacts," International Workshop on Nitride Semiconductors, Kanazawa, Japan, November 2018.

E. Clinton, E. Vadiee, and W. A. Doolittle, "High Growth Rate Plasma Considerations for Indium-Rich III-Nitrides," 34th North American Conference on Molecular Beam Epitaxy, Banff, Alberta, Canada, October 2018.

E. Clinton, E. Vadiee, and W. A. Doolittle, "High Growth Rate Plasma Considerations and Applications to Metal Modulated Epitaxy of High Indium Content III-Nitrides," 60th Electronic Materials Conference, Santa Barbara, California, June 2018.

E. Clinton, E. Vadiee, and W. A. Doolittle, "Negative Differential Resistance in GaN Homojunction p++/n++ Tunnel Diodes and their Application as Tunnel Contacts to GaN p/i/n Diodes," 60th Electronic Materials Conference, Santa Barbara, California, June 2018.

E. Clinton, J. Merola, B. Gunning, and W. A. Doolittle, "Metal Modulated Epitaxy of High Carrier Concentration Mg doped p-type and Ge doped n-type AlGaN," International Workshop on Nitride Semiconductors, Orlando, Florida, October 2016.

E. Clinton, B. Gunning, C. Fabien, J. Merola, W. A. Doolittle, S. Wang, A. Fischer, and F. Ponce, "Highly degenerate p-type GaN and AlGaN Grown via Metal Modulated Epitaxy," 19th International Conference on Molecular Beam Epitaxy, Montpelier, France, September 2016.

E. Clinton, B. Gunning, J. Merola, and W. A. Doolittle, "Metal Modulated Epitaxy of GaN at High Growth Rates >9μm/hr," 19th International Conference on Molecular Beam Epitaxy, Montpelier, France, September 2016.

E. Clinton, B. Gunning, C. Fabien, J. Merola, W. A. Doolittle, S. Wang, A. Fischer, and F. Ponce, "Growth of High Carrier Concentration AlGaN by Metal Modulated Epitaxy," 58th Electronic Materials Conference, Newark, Delaware, June 2016.

E. Clinton, C. Fabien, J. Merola, B. Gunning, E. Vadiee, A. Fischer, Y. Wei, H. Xie, F. Ponce, and W. A. Doolittle, "Progress Towards InxGa1-xN Templates for Optoelectronic Devices," 58th Electronic Materials Conference, Newark, Delaware, June 2016.

First-Authored Conference Posters

E. Clinton, E. Vadiee, S. C. Shen, K. Mehta, P. D. Yoder, and W. A. Doolittle, "GaN Homojunction Tunnel Diodes Exhibiting Negative Differential Resistance and their Application as Tunnel Contacts," International Workshop on Nitride Semiconductors, Kanazawa, Japan, November 2018.

E. Clinton, E. Vadiee, B. Gunning, C. Fabien, J. Merola, A. Fischer, S. Wang, F. Ponce, and W. A. Doolittle, "N-polar and Ga-polar p-type GaN Grown via Metal Modulated Epitaxy," 12th International Conference on Nitride Semiconductors, Strasbourg, France, July 2017.

E. Clinton, B. Gunning, J. Merola, E. Vadiee, L. Yates, S. Graham, and W. A. Doolittle, "High Growth Rate, Low Residual Doped Metal Modulated Epitaxy of GaN at 10 μm/hr," International Workshop on Nitride Semiconductors, Orlando, Florida, October 2016.

E. Clinton, C. Fabien, B. Gunning, and W. A. Doolittle, "Thick, Rapidly Grown (1.8 μm/hr) $In_xGa_{1-x}N$: Towards Templates for Optoelectronics," International Workshop on Nitride Semiconductors, Orlando, Florida, October 2016.

E. Clinton, J. Merola, E. Vadiee, and W. A. Doolittle, "Progress Towards InGaN Templates for Optoelectronic Devices," 19th International Conference on Molecular Beam Epitaxy, Montpelier, France, September 2016.

E. Clinton, C. Fabien, B. Gunning, E. Vadiee, Y. Wei, A. Fischer, F. Ponce, and W. A. Doolittle, "Progress Towards InGaN Templates for Optoelectronic Devices," 19th International Conference on Molecular Beam Epitaxy, Montpelier, France, September 2016.